QUANTUM-LIMITED MECHANICAL RESONATOR MEASUREMENT AND BACK-ACTION COOLING TO NEAR THE QUANTUM GROUND STATE.

A Dissertation

Presented to the Faculty of the Graduate School

of Cornell University

in Partial Fulfillment of the Requirements for the Degree of

Doctor of Philosophy

by

Tristan Orion Rocheleau

January 2011

QUANTUM-LIMITED MECHANICAL RESONATOR MEASUREMENT AND BACK-ACTION COOLING TO NEAR THE QUANTUM GROUND STATE.

Tristan Orion Rocheleau, Ph.D.

Cornell University 2011

For decades, quantum mechanics has been a hugely successful theory for understanding the microscopic world. Despite its seemingly non-physical predictions, such as superposition or cat states, the accuracy of the theory has been verified time and again for microscopic systems composed of single atoms or other quantum particles. Up till now, however, our understanding of how and if these quantum predictions scale to larger systems closer to our everyday perceptions, where we do not see quantum "weirdness", is an open question. One platform to pursue observation of quantum effects in a system composed of large ensembles of atoms rather than single particles is that of nanomechanical resonators. Several schemes have been proposed to observe quantum effects in these systems, eg [1],[41], but a common feature is the requirement that the mechanical resonator be at or near its quantum ground state, which has proved challenging to achieve.

In this dissertation, a novel mechanical motion readout scheme using superconducting resonators is presented and shown to allow near quantum limited detection. In any strong measurement of a system, quantum mechanics dictates that the measurement will inherently produce some "back-action" on the measured system. It will be shown that for the measurement system presented, back-action forces can additionally be used to cool a single mode of a mechanical resonator to near its quantum ground state, with the lowest observed occu-

pation factor at 3.8 ±1.3 quanta. This is a low enough occupation level that the nanoresonator is in its ground state statistically 21% of the time and opens up the possibility of preforming further quantum experiments.

The system investigated in this dissertation is composed of a nanoscale mechanical resonator capacitively coupled to a superconducting coplanar waveguide resonator. The resonators were nanofabricated on a silicon substrate and cooled to low temperature in a dilution refrigerator system. Applying microwave signals to the device and measuring output spectra provided the means to both observe the mechanical motion and produce the back-action forces.

BIOGRAPHICAL SKETCH

Tristan Rocheleau grew up in the town of Arcata, located on the northern coast of California. From an early age, he found a natural inclination towards science and a desire to understand the world, a tendency which was supported and fostered by his parents. When it came time for college, a physics education seemed like the obvious choice. To this end, Tristan chose to join the physics program in the College of Creative Studies at the University of California at Santa Barbara. Receiving his degree in 2005, he then took a position as a Ph.D. student in physics at Cornell University with the intent of focusing on experimental condensed matter. In early 2006, he joined Keith Schwab's group just as Keith was joining the faculty at Cornell. In the following years, Tristan was involved in setting up the low temperature lab and performing work towards measurement and cooling to the quantum mechanical ground state of a nanomechanical oscillator coupled to superconducting circuits. In 2010, Tristan helped pack the lab up again for a move to Caltech, before graduating with the Ph.D.

ACKNOWLEDGEMENTS

I would first like to acknowledge the funding sources that have supported me through my graduate career. In particular, I would like to thank the Cornell Physics department and Cornell university in general for providing support during the early part of my graduate career. Cornell university provides generous graduate stipends and guaranteed support for all their Ph.D. students for which I am very grateful. In addition, I would like to thank the National Science Foundation, which provided funds for my support as well as the purchase of needed equipment in Keith Schwab's lab. There are very few agencies providing funds for fundamental science work such as we have been doing, and without the NSF I feel that it would be fair to say that we would be unable to accomplish our research goals.

I would like additionally to acknowledge the positive influence Keith Schwab has had on my graduate education. It goes without saying that his scientific mentoring and advising was top-notch, but beyond that his personal support and guidance has been and continues to be of great benefit. Graduate school in experimental physics can be a hard road but having an advisor that has the foresight to push you down productive avenues of research and the understanding of the difficulties involved in so doing can help. While I can not deny that we have not always seen eye-to-eye on everything, despite occasional disagreements Keith has continued to believe in my ability to do good work and in my eventual capability as a scientist, and for that I am deeply grateful.

I am also extremely grateful for the support my parents have provided me through grad school and my entire life. They have always encouraged my exploration and education in whatever I was interested in and have never tried to push their own desires upon me. When I decided that Cornell was the best

place to pursue graduate school, they never tried to disuade or keep me on the west coast. To a great extent, I owe my ability to push my physics education to the furthest extremes to their unwavering support.

I would additionally like to thank the major contributions provided for by the many colleagues I have worked with on these experiments. In particular, I worked very closely with fellow graduate students Tchefor Ndukum and Jared Hertzberg. Their tireless efforts were central in the development and running of all the experiments conducted at Cornell. In addition, I would like to thank the many undergraduate students with whom I have had the privilege of working throughout my graduate career. Their enthusiasm and talents both brought novel viewpoints to the experiments as well as accomplishing many tasks that would have been difficult or impossible without their help.

I would finally like to acknowledge the help and support of the many other people I interacted with through grad school: Nathan Ellis in the graduate machine, Stan Carpenter and the others in the professional machine shop, Nicholas Brown, and many others too numerous to name here.

TABLE OF CONTENTS

LIST OF FIGURES

LIST OF ABBREVIATIONS

SR	Superconducting Microwave Resonator
NR	Nanomechanical Resonator
CPW	Coplanar waveguide
SiN	Silicon nitride
SOM	Supplemental Online Materials
HEMT	High Electron Mobility Transistor
SEM	Scanning Electron Microscope
PCB	Printed Circuit Board
RBW	Resolution BandWidth
OFHC	Oxygen Free HIgh Conductivity
AFG	Arbitrary Function Generator
FFT	Fast Fourier Transform
FPGA	Flash Programable Gate Array

LIST OF SYMBOLS

C_{tot} Total effective capacitance of SR

C_κ Capacitance coupling at each end of SMR to external circuitry

C_g Gate capacitance coupling SR to NR

Γ_m Linewidth of NR due to coupling to thermal bath

Γ_{opt} Dissipation of NR due to coupling to microwave field

Γ_{tot} Total measured NR linewidth

(All symbols ω, κ and Γ are in units of angular frequency.)

$gain$ Total gain of apparatus from SR to spectrum analyzer

$\hbar$ Reduced Planck constant

κ_{int} Linewidth of SR due to internal dissipation

κ_{ext} Linewidth of SR due to coupling to external circuitry

κ_{tot} Total linewidth of SR ($\kappa_{tot} = \kappa_{ext} + \kappa_{int}$)

k Spring constant of NR

k_B Boltzmann's constant

m_{NR} Effective mass of NR

$\bar{n}_{SR}$ Occupation of pump photons in SR

$\bar{n}_{SR}^T$ Thermal occupation of SR

$\bar{n}_{NR}^T$ Thermal occupation of NR when coupled only to thermal bath

$\bar{n}_{NR}^{opt}$ Effective occupation of energy bath formed by microwave field

$\bar{n}_{NR}^{eff}$ Apparent occupation of NR as directly measured

$\bar{n}_{NR}$ Equilibrium occupation of NR

ω_{SR} Resonant frequency of SR

ω_{NR} Resonant frequency of SR

$\Delta\omega$ Difference of frequency from ω_{SR}

P_{in} Input pump power to SR

P_{out} Output pump power from SR

P_{sideb} Power of sideband signal generated by NR motion

S_x Position noise spectral density

R_L Load resistance of external circuitry (typically 50 ohms)

T Fridge or thermal bath temperature

x Instantaneous amplitude of mechanical motion

$\langle x^2 \rangle$ Mean-squared amplitude of mechanical motion

Δx Position uncertainty

Δx_{ZP} Zero-point motion

Z_0 Characteristic impedance of transmission line

CHAPTER 1

INTRODUCTION

Since its inception, quantum mechanics has made many seemingly impossible and counter-intuitive predictions about our world. The most unexpected predictions are those which contradict our every-day experience and intuition: predictions which say that an electron can be both up or down, or on a larger scale, that a physical object can be both here and there. While unusual, the claims of quantum mechanics have been borne out consistently by experiment on single atoms or photons, and at present day no one doubts the validity of quantum mechanics as a physical theory for microscopic systems.

One regime that quantum mechanics experiments have not yet made significant inroads in is that of macroscopic systems composed of large ensembles of atoms. Systems, that is, more like actual real-world objects. In this dissertation work is presented which makes some steps towards the goal of expanding quantum mechanics closer to the real world. The system chosen for this work is that of nanomechanical oscillators. These oscillators, while still tiny, are composed of greater than 10^{10} atoms and can reasonably be considered macroscopic.

In order to observe quantum effects of such a system, a primary requirement is to prepare the mechanical resonator in or near its quantum ground state. Several proposals exist to see quantum effects for such systems, e.g. [1],[41], but all require a low quantum mechanical occupation. While quantum effects would theoretically still be present for a resonator in a thermally excited state, in practice the thermal occupation smears out the quantum signature. As such, the mechanical resonator must be cooled to a low thermal occupation before quantum effects can be seen.

The work presented in this dissertation is primarily focused on the cooling of a nanomechanical resonator to near it's ground state. This experiment involved the nanofabrication of a silicon device composed of a doubly-clamped nanomechanical resonator(NR) coupled to a superconducting resonator. The device was cooled in a dilution refrigerator wired to allow high-bandwidth signals and then measured using microwave techniques. By employing a dynamical back-action effect produced by a properly tuned microwave drive signal, the NR motion was simultaneously cooled and measured. In order to better understand the motivation for this work, a brief discussion of the possible NR cooling techniques and previous work is presented, followed by an overview of the specific approach used in this thesis.

1.1 Cooling of Mechanical Resonators

Several avenues to a cold mechanical resonator exist. The most direct method is simple passive cooling in which the resonator is directly cooled by a refrigeration system. The level of cooling required to reach the ground state is discussed in detail in section 2.2, but broadly speaking the difficulty of achieving the ground state lies in creating a high enough frequency resonator with a detection scheme that allows near quantum limited motion detection. Prior to the work discussed here, the closest approach was limited to an average NR occupation $\bar{n}_{NR} = 25$ [43].

Assuming passive cooling is insufficient, an active cooling scheme is required. Several possibilities exist ranging from direct active feedback cooling[48], techniques such as coupling to q-bit systems [43], and the dynamical back-action cooling technique used in this dissertation. Unfortunately, the

active cooling technique is limited directly by measurement noise of the detector and has yet to demonstrate competitive cooling results. Cooling schemes such as q-bit coupling have also thus far failed to provide results superior to simple bulk cooling [34]. Back-action cooling is one of the few techniques expected to allow cooling over several orders of magnitude to near the ground state[37].

The dynamical backaction cooling technique is not new, having been studied and used for years, though not targeted towards nanomechanics or ground state cooling. In particular, the field of gravity wave detection has had significant work done on these effects, where super high-precision readout techniques have been necessary, eg [62, 6]. The parametric coupling and readout scheme used here bears significant similarities to these previous works. [4], for example, demonstrates parametric coupling and backaction cooling(called "cold damping" in the lingo of the day) of a 1.5 tonne gravity wave antenna resonating at 700Hz coupled to a 10GHz superconducting cavity. While the mechanical resonator sizes are hugely different, 1.5 tonnes vs. 1pg, the basic physics of the capacitive coupling and back action are essentially the same.

The nanomechanical readout and backaction presented here builds upon these type of designs, but with a focus toward pushing the limits of measurement precision and in particular allowing a maximum of cooling effect in the attempt to push toward the ground state. A system using a microwave readout scheme allowed installation in a dilution refrigerator system for a low starting occupation and the use of high-quality commercial microwave sources and components.

1.2 Experimental introduction

A basic overview of the experiment is shown in figure 1.1. The device used in these measurements consisted of a superconducting resonator formed from a length of co-planar waveguide, 1.1 a), capacitively coupled to a doubly clamped nanomechanical resonator, seen in 1.1 c). Measurements of this device were conducted by sending microwaves in one side of the superconducting resonator and measuring the spectra of microwaves coming out the other side, as shown in the simplified schematic in 1.1 b).

This capacitively coupled NR - SR system here provides the ability to both accurately measure NR motion, and to directly produce back-action forces upon the NR. The measurement scheme used in this dissertation involves driving the SR with a "red-detuned", or lower frequency microwave pump signal. Because of the capacitive coupling of the NR to the SR, the motion of the NR causes a modulation of the total capacitance of the waveguide used in the SR. This modulation in turn changes the resonant frequency of the SR. This produces a modulation of the microwave signal incident on the SR which creates two sidebands on the microwave drive displaced by the NR frequency. Due to the lorentizian response of the SR, the sideband at higher frequency is significantly enhanced, compared to the sideband at lower frequency. By directly measuring the power spectrum near the SR resonance frequency, the side-band provides an accurate read-out of NR motion.

In addition to working as a direct mechanical resonator motion detector, this particular measurement configuration also provides the back-action forces necessary to cool the NR mode. This is best understood from a quantum standpoint

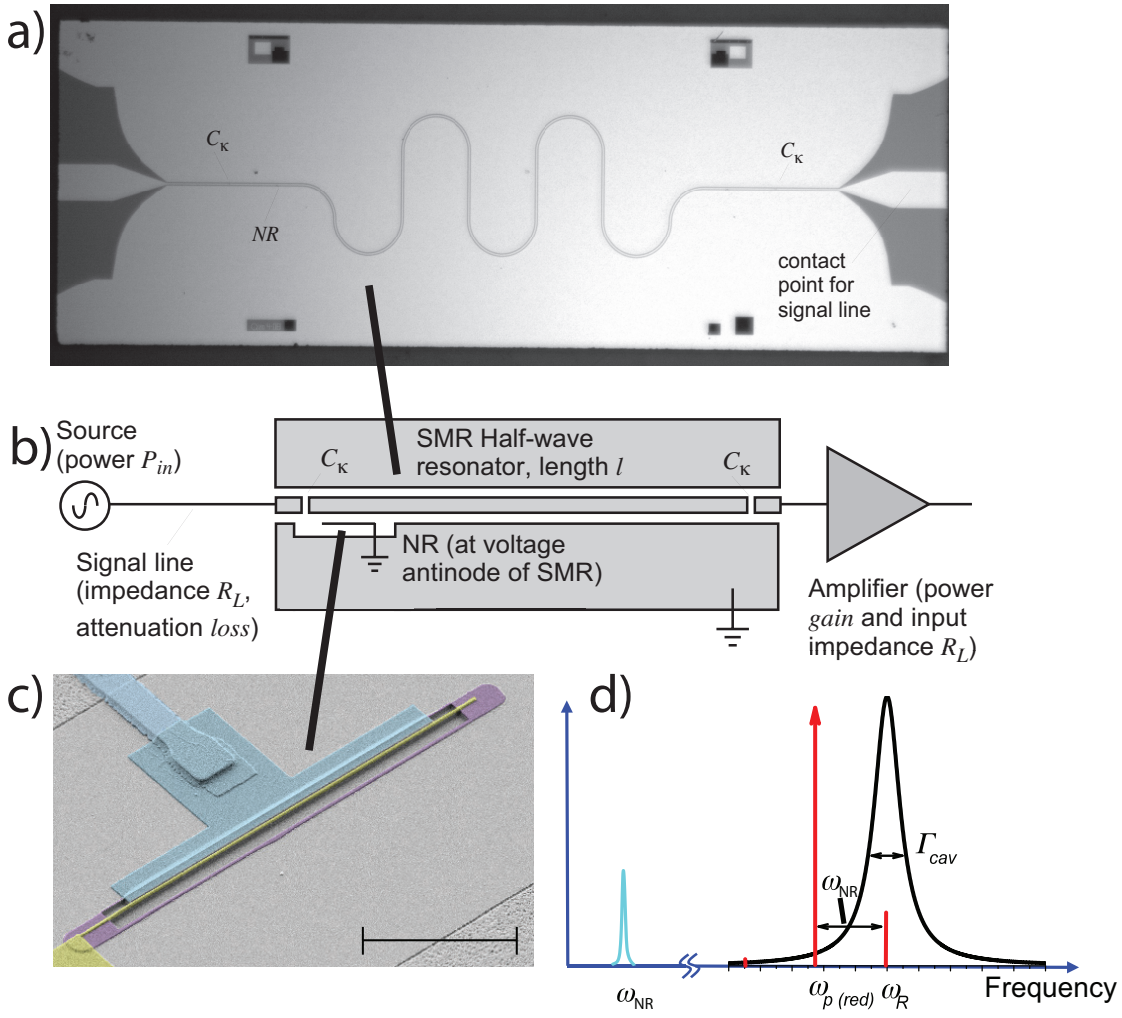

Figure 1.1: Experiment overview.

as a process analogous to Raman scattering. The generation of the sidebands due to NR motion corresponds to an increase or decrease in photon energy of the microwave pump. Each time a microwave photon is scattered by the NR to a higher or lower frequency, it absorbs or emits a phonon from or to the NR. For the red-detuned microwave pump, the response of the SR naturally inhibits down-conversion and enhances up-conversion of the photons. The intensity of the enhanced up-conversion sideband then directly corresponds to a rate of extraction of phonons, or in other words, cooling.

By increasing the microwave pump power, the rate of phonon extraction or cooling can be increased. This provides a controllable cooling effect on the single mode of mechanical motion which, in principle at least, can be used to cool the motion to an arbitrary effective temperature and is the basis upon which the majority of work in this dissertation is based. The physics and behavior of the measurement and cooling scheme here is described in more detail in chapter 2.

1.3 Overview of the Dissertation

This dissertation is structured as follows: Starting with chapter 2, an overview of the general physics concepts and theory of the nanomechanical resonator and superconducting resonator is presented. The necessary concepts for understanding and analyzing NR measurement data are also discussed. In chapter 3, the experimental apparatus design and operation is introduced. Chapter 4 provides a detailed description of each major measurement technique used along with some discussion of analysis. Chapter 5 presents the data and results of the measurement and back-action cooling of the best device measured thus far. Finally, chapter 6 provides some discussion of the meaning and interpretation of the results presented and finishes with some concluding remarks. The two appendices detail device fabrication recipes and some calculations and discussion on a proposed follow-up experiment designed to show quantum effects of the NR.

CHAPTER 2

NANOMECHANICAL RESONATORS COUPLED TO SUPERCONDUCTING WAVEGUIDE RESONATORS: A THEORETICAL OVERVIEW

The devices used in this dissertation consisted, for the most part, of nanofabricated mechanical resonators(NR) capacitively coupled to superconducting resonators(SR). These devices were engineered such that motion of the nanoresonator modulates voltages in the superconducting resonators, which can be directly read out, allowing a near quantum limited measurement of NR motion. For any measurement, there will be some associated back-action upon the measured system. In the coupled resonator scheme investigated here, the measurement can be conducted in such a fashion that voltages in the SR produce back-action forces upon the NR to produce a cooling effect. In this chapter, an overview of the basic physics and theoretical underpinnings of the SR, NR and their interaction is introduced.

The Hamiltonian which describes the capacitively coupled resonators is given by[38, 69]:

$$\hat{H} = \hbar(\omega_{sr} + g\hat{x} - \frac{1}{2}\lambda\hat{x}^2)(\hat{b}^\dagger\hat{b} + \frac{1}{2}) + \hbar\omega_m(\hat{a}^\dagger\hat{a} + \frac{1}{2}) \tag{2.1}$$

with

$$g = \frac{\partial \omega_{sr}}{\partial x} = \frac{\omega_{sr}}{2C_t}\frac{\partial C_g}{\partial x} \tag{2.2}$$

$$\hat{x} = x_{zp}(\hat{a}^\dagger + \hat{a}) \tag{2.3}$$

$$\tag{2.4}$$

where $\hat{a}$, $\hat{a}^\dagger$ are the NR annihilation and creation operators and $\hat{b}$, $\hat{b}^\dagger$ are the SR annihilation and creation operators. g is the coupling of the NR to SR and is a measure of how much a displacement of the NR pulls the resonant frequency of the SR. $x_{zp} == \sqrt{\frac{\hbar}{2m\omega_{NR}}}$ is the zero point motion amplitude of the NR. The first term in the hamiltonian represents the total coupling of the SR frequency to the mechanical motion. The $\frac{1}{2}\lambda\hat{x}^2$ term represents electrostatic non-linear frequency pulling of the mechanical resonator by the SR due to the microwave fields, where $\lambda = \frac{\omega_{sr}}{2C_t}\frac{\partial^2 C_g}{\partial x^2}$.

This hamiltonian fully describes the the behavior of the devices used in this dissertation based upon a parametric coupling between a doubly clamped silicon beam resonator capacitively coupled to a coplanar waveguide resonator. The method used to measure the motion and cool a nanoresonator uses this interaction with an applied microwave pump. A fully quantum mechanical treatment of this interaction and the associated back-action for an arbitrary measurement pump can be derived from this Hamiltonian, see [38]. As the case of a red-detuned(lower frequency than the SR resonance) cooling pump is of primary interest here, this chapter focuses in such a configuration. First, however, a brief description of the behavior of each resonator, NR and SR, individually is warranted.

2.1 The Co-planar Waveguide resonator

The superconducting resonators used in these experiments were based upon sections of coplanar waveguide bounded by small coupling capacitors at each end, forming a two dimensional resonant cavity. This configuration, shown schematically in figure 2.1, creates a cavity whose modes act to close approximation as a simple harmonic oscillator. These have been studied extensively in earlier experiments, e.g. [57], [26], but a brief overview of the principles involved will aid in understanding and discussion of the dissertation. To understand this behavior, it is instructive to first briefly review the well-known LRC resonator.

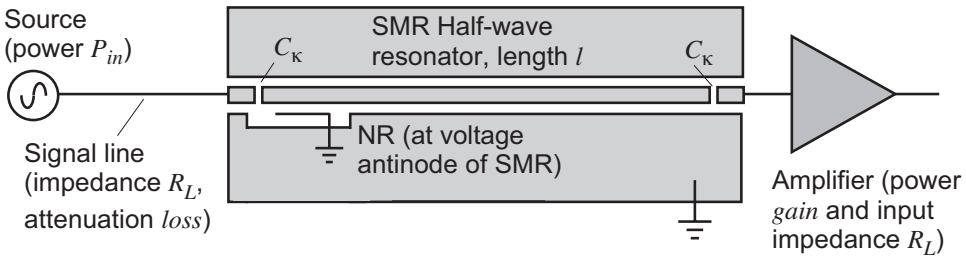

Figure 2.1: Schematic diagram of the superconducting resonator. Microwave signals from an external source are applied from the left to the on-chip fabricated CPW superconducting resonator. The nanoresonator is capacitively coupled to the centerline of the SR near one end where SR voltage swings are at a max. Microwave signals leak out of the SR on the right, where they routed to a low-noise amplifier.

2.1.1 the LRC resonator

The LRC resonator is of course the classic damped electrical resonance formed of a parallel capacitance, inductance, and resistance. From a circuit model, one can easily obtain the differential equation of the charge on the capacitance, q:

$$\frac{d^2q}{dt^2} - \frac{1}{RC}\frac{dq}{dt} + \frac{q}{LC} = 0 \tag{2.5}$$

Which has the form of a damped simple harmonic oscillator with the solution:

$$q(t) = q_0 e^{-\frac{\kappa}{2}t} e^{i(\omega_0 t + \phi)} \tag{2.6}$$

a damped oscillation with frequency $\omega_0 = 1/\sqrt{LC}$ and a decay time $\kappa = 2/RC$. An alternative method of treating an LRC oscillator, which is more useful for the current discussions, is to look at the total complex input impedance of the resonator as in figure 2.2. For the three components in parallel, this gives:

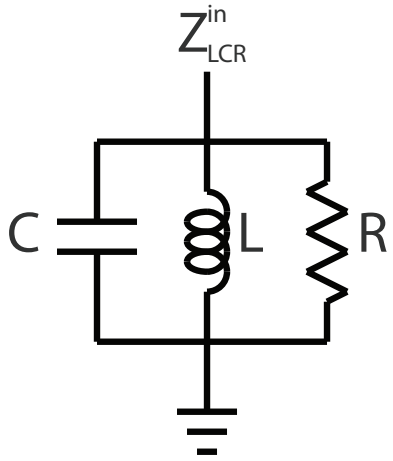

Figure 2.2: Simple harmonic oscillator formed from an LRC circuit. Z^{in}_{LRC} is the complex impedance looking into the circuit.

$$Z^{in}_{LCR} = \frac{1}{i\omega C - \frac{i}{\omega L} + \frac{1}{R}} \tag{2.7}$$

Defining $\delta = \omega - \omega_0$ and expanding this impedance around $\omega = \omega_0$ for small δ gives:

$$Z^{in}_{LRC} \approx \frac{R}{1 + 2iRC\delta} \tag{2.8}$$

or with the substitution $Q = \omega_0 RC$, the quality factor of the resonator:

$$Z^{in}_{LRC} \approx \frac{R}{1 + i\frac{2\delta Q}{\omega_0}} \tag{2.9}$$

This expression provides the input impedance for the LRC resonator for frequencies near resonance. This will be useful for comparison purposes after preforming a similar investigation of the waveguide resonator.

2.1.2 Coplanar Waveguide Resonator

Using a similar input impedance view, a comparison can be made to the coplanar waveguide resonator. [49] gives the input impedance for a length of lossless waveguide terminated by Z_L as:

$$Z^{in}_{CPW} = Z_0 \frac{Z_L + iZ_0 tan(\beta l)}{Z0 + iZ_L tan(\beta l)} \tag{2.10}$$

Where Z_0 is the characteristic impedance of the waveguide, l is the length of the waveguide section, $\beta = 2\pi/\lambda$ is the propagation constant, and λ is the wavelength. In the case of the superconducting waveguides used in this dissertations, the approximation of the waveguide as lossless is a good one. In this case, each end of the waveguide section is connected to the external circuit by a small capacitive coupling. To good approximation, this can be regarded in equation 2.10 as an open load, ie. an infinite Z_L. This gives:

$$Z^{in}_{open} = icot(\beta l) \tag{2.11}$$

For $\beta l = n\pi$, this gives an infinite Z^{in}. A small input coupling capacitor acts as an extremely high driving impedance, and this thus leads to maximum signal transmitted, or resonance, at these values of βl. From this, it is seen that the section of capacitively coupled waveguide has resonance conditions when

$$l = n\frac{\lambda}{2} = \frac{\pi v}{\omega_0}$$

This makes sense from a conceptual standpoint as well. When a propagating EM wave in the waveguide is of a wavelength such that its antinodes are located at the end coupling capacitors(which are high impedance and thus easy to drive to arbitrary voltage) the wave is in resonance with the cavity.

To better understand the resonator character of the waveguide cavity, one can expand Z^{in}_{open} for small deviations from a resonant mode. Near resonance, the effect of even small waveguide losses becomes significant, and so must also be taken into account. Adding in loss for the open load impedance gives:

$$Z^{in}_{open} = Z_0 \frac{1 + iZ_0 tan(\beta l) tanh(\alpha l)}{tanh(\alpha l) + itan(\beta l)} \tag{2.12}$$

Defining $\delta\omega_n = \omega - \omega_n$ where ω_n is the nth harmonic resonance, we can expand 2.12 using $\beta l = \frac{\omega}{v}\frac{\pi v}{\omega_0} = \pi\frac{n\omega_0 + \delta\omega_n}{\omega_0}$ for small $\delta\omega_n$ and α. Doing so and simplifying gives:

$$Z_{open}^{in} = Z_0 \frac{1 + iZ_0 tan(\beta l) tanh(\alpha l)}{tanh(\alpha l) + itan(\beta l)} \tag{2.13}$$

Comparing the form of 2.13 to that of the LCR impedance 2.9 it is clear that they share the same form. From this comparison, direct parallels to the SHO parameters of the LCR circuit for the nth harmonic of the CPW cavity can be made:

$$\omega_n = n\omega_0 \tag{2.14}$$

$$Q_n = \frac{n\pi}{2\alpha l} \tag{2.15}$$

$$R_n = R_l l \tag{2.16}$$

$$C_n = \frac{Q}{\omega_n R} \tag{2.17}$$

$$L_n = \frac{1}{\omega_n^2 C} \tag{2.18}$$

$$\tag{2.19}$$

These values are effective equivalent LRC components that would produce the same resonance as the waveguide cavity. This model proves useful as it distills the 2-dimensional varying EM fields to a simple circuit model which can be more readily used calculating interactions with other components, as seen in the following sections.

2.1.3 External Coupling of the Superconducting Resonator

In the previous discussion, it was assumed that any coupling of the waveguide resonator to the external lines was through small capacitances at each end that

could be effectively treated as open breaks. Realistically, any additional coupling, either to drive or measure the resonator, provides a path for energy to be lost from the resonator. This is directly seen as an additional source of loss, leading to a decreased Q. Here, the Q value derived in the previous section is referred to as the "unloaded Q", the Q value achievable with no coupling of the resonator to any external system. As is well established by many sources, eg [49], [20], the overall observed Q, or loaded Q, of the resonator is given by:

$$\frac{1}{Q_L} = \frac{1}{Q_{ext}} + \frac{1}{Q_{int}} \tag{2.20}$$

Where Q_L is loaded Q, Q_{ext} is the Q value taking into account only external loading, and Q_{int} is the internal Q value for no external coupling. Q_{ext} is dependent upon the size of the coupling capacitors which can designed to achieve a design Q value. The value of Q_{ext} can be most easily determined by looking at the total loading on the equivalent LRC resonator due to the external capacitance. Converting this loading to a Nortan quivalent parallel impedance, as in [27], [57], allows a direct comparison with the LRC model R term and thus the effective Q:

$$Q_{ext} = \frac{\pi}{Z_0 n \omega_0 C_\kappa^2} \tag{2.21}$$

Where C_κ is the total capacitive coupling to the external lines. For cases where internal losses are minimal, the Q of the resonator is primarily determined by the coupling capacitor size, which can be directly calculated or estimated based on geometry(see, for example [59]).

In addition to the design of Q, an understanding of the external coupling

and losses is essential to an understanding of the rates at which photons leak out of the cavity. For the measurements in these experiments, it is ultimately the photons exiting the cavity that are observed and from which estimates of signal strength within the cavity are made. To better understand this, it is useful to define the coupling to the external waveguides, κ_{ext} and to internal loss mechanisms, κ_{int} in angular frequency:

$$\kappa_{int} = \frac{\omega_{SR}}{Q_{int}} \tag{2.22}$$

$$\kappa_{ext} = \frac{\omega_{SR}}{Q_{ext}} \tag{2.23}$$

$$\kappa_{tot} = \kappa_{int} + \kappa_{ext} \tag{2.24}$$

κ_{ext} can additionally be broken into components for the left and right coupling capacitors: $\kappa_{ext} = \kappa_R + \kappa_L$ to account for designs where the coupling capacitors are not identical. These angular frequencies represent the coupling of the energy stored in the resonator to specific loss mechanisms, such that the power delivered, eg to the output waveguide, is given by:

$$P_{out} = \kappa_R * E_{SR} \tag{2.25}$$

Where $E_{SR} = \frac{1}{2} C_{tot} * \bar{V_{SR}}^2$ is the energy stored in the SR(V_{SR} is the voltage on the centerline of the SR). Knowing κ_R thus allows a direct relation of measured output power to either internal voltages or cavity energy which in turn is equivalent to knowing cavity occupation.

While κ_{tot} is directly measurable from a measurement of overall linewidth of the SR, the individual couplings to loss terms and the external waveguides are

harder to tease out. To determine these values individually, the signal from the coupled nanoresonator is needed. This will be discussed in detail in section 2.3 after introducing the dynamics of the nanoresonator itself.

2.2 Nanoresonator Occupation

In order to begin to see any inherent quantum nature of a mesoscopic mechanical resonator, it becomes necessary to prepare it in a state at or near its quantum ground state. Achieving this in a resonator that is possible to couple to a system necessary to measure the near quantum limited motion has thus far proved challenging. To give a perspective of the difficulty involved, the zero point motion of a typical mechanical resonator used here is around $25fm$. This means that in the quantum ground state, a detection scheme with sufficient fidelity to observe motion of this amplitude is needed; a measurement of position equal to the width of about 3 atomic nuclei of gold!

Many strategies have been proposed[38, 69] and applied in an attempt to reach this quantum regime with varying success. Experiments with nanomechanical structures have been able to reach and detect $\bar{n}_m = 25$ through passive cooling of a nanomechanical resonator [43], using a superconducting single electron transistor as the detector. Opto-mechanical systems have been able to utilize ultra-sensitive optical detection and radiation pressure to both cool and detect $\bar{n}_m = 65$ in a toroidal resonator[46], $\bar{n}_m = 37$ in microsphere resonator[54], and $\bar{n}_m = 35$ in an optical cavity[25].

The nanomechanical resonators used in the work described in this thesis were all of the doubly clamped suspended beam type. A typical device is shown

in figure 2.3. Constructed of high stress SiN with a thin metallization layer, the vibration of these resonators were dominated by tensional forces. That is to say, these doubly clamped beams behave much like vibrating strings with fundamental and harmonic resonance frequencies dictated by geometry and tension.

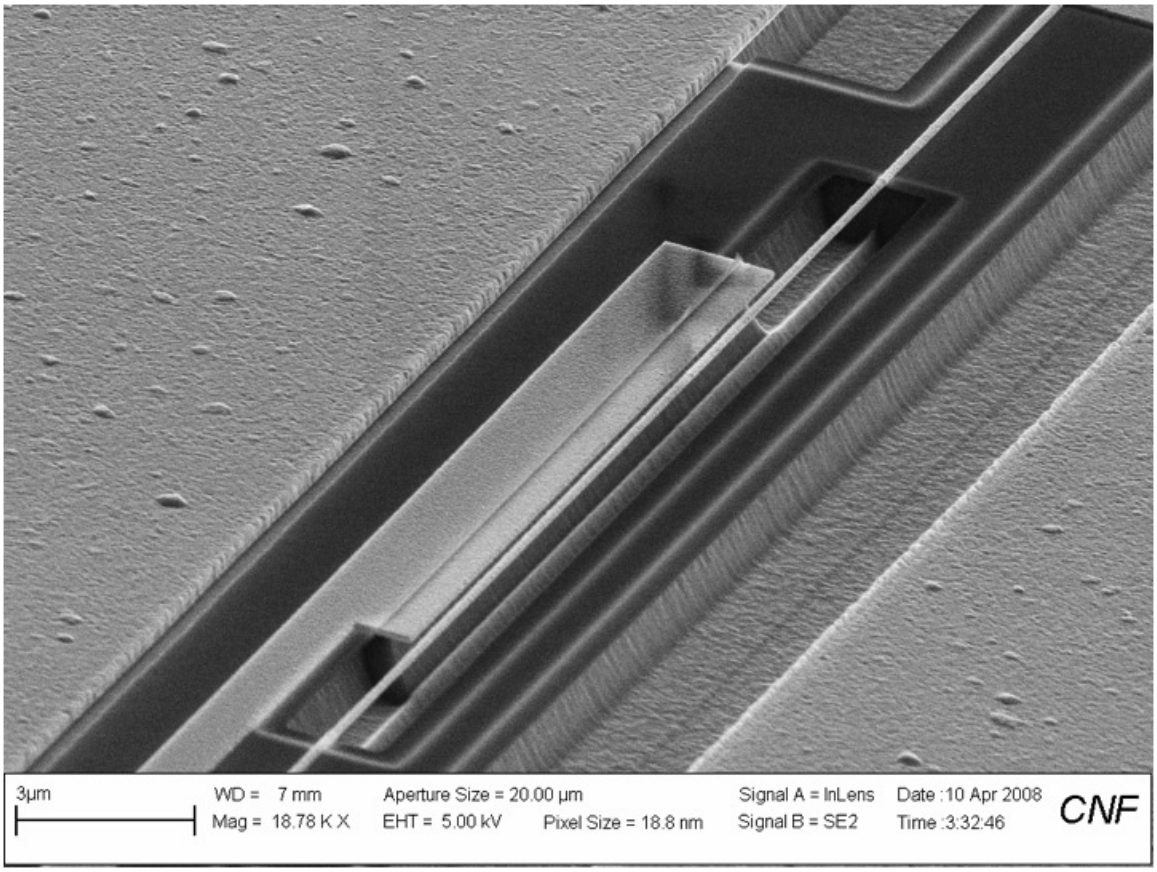

Figure 2.3: Example nanomechanical resonator SEM image. The NR is formed from the thin beam in the center of the image vibrating in-plane. The larger metalized region on the left forms the closely-coupled gate connected to the SR centerline.

Despite the mesoscopic scale of these devices, consisting of billions of individual atoms, it is expected that in the proper regime the collective oscillation modes will behave according to quantum mechanics. Looking only at the collective dynamics of the resonant mode, this can treated as a quantum simple harmonic oscillator with energy quantized: $E_n = \hbar\omega_m(n + \frac{1}{2})$, where n is the NR

occupation and ω_m is the resonant frequency.

While the inherant quantum nature of this system should exist at any temperature, schemes to actually observe quantum behavior require a low average energy state of the NR. For a thermal equilibrium, the average occupation is given by [31]:

$$< n_{th} >= (e^{\hbar\omega_{NR}/k_BT} - 1)^{-1} \tag{2.26}$$

where T, $2\pi\hbar$, and k_B are the temperature, Planck's and Boltzmann's constants respectively. Cooling a resonator into the quantum regime where $\bar{n}_m^T << 1$ and measuring the very small motions has been challenging for a number of technical reasons; not only are very low temperatures necessary to freeze-out the mode, but detection with sensitivity at the quantum zero-point level is required: $x_{zp} = \sqrt{\hbar/(2m\omega_m)}$, where m is the resonator mass. Furthermore, the position measurement must not heat the mode with significant measurement backaction[43], [9].

In order to achieve low average thermal occupation, one requires that the average thermal energy, k_BT be small compared to the energy level spacing. In the limit where $k_BT < \hbar\omega_{NR}$ we enter the so called "freeze-out" regime where average thermal occupation drops expoentially with decreasing temperature and the NR is in its ground state much of the time.

Figure 2.4 shows the calculated thermal occupation of various frequency resonators vs. bath temperature. In order to achieve ground state operation, either temperature can be decreased or NR frequency increased. While refigeration technologies exist that can achieve down to microkelvin temperatures, a rea-

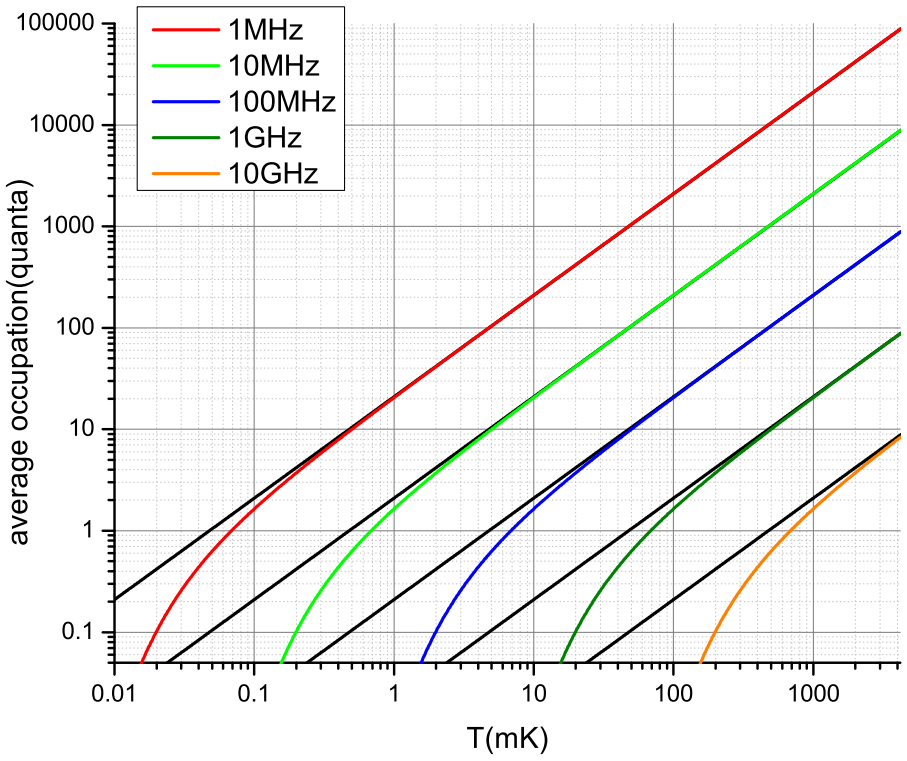

Figure 2.4: Average thermal occupation vs. temperature for a selection of different nanoresonator frequencies. Colored traces show behavior as predicted by quantum mechanics and exhibit "freeze-out" while the black lines show behavior predicted by purely classical mechanics.

sonable practical limit is the use of dilution refigerators with a base temperature of typically no lower than 4mK. At these temperatures, this requires NR frequencies of 100's of MHz. While this is certainly achievable from a technology standpoint(recent developments in MEMs filters have shown high Q micro resonators operating at up to 10's of GHz [67, 68]) coupling begins to become difficult using a capacitive gap coupling technique as we have here, as the motional amplitude becomes increasingly small for these devices.

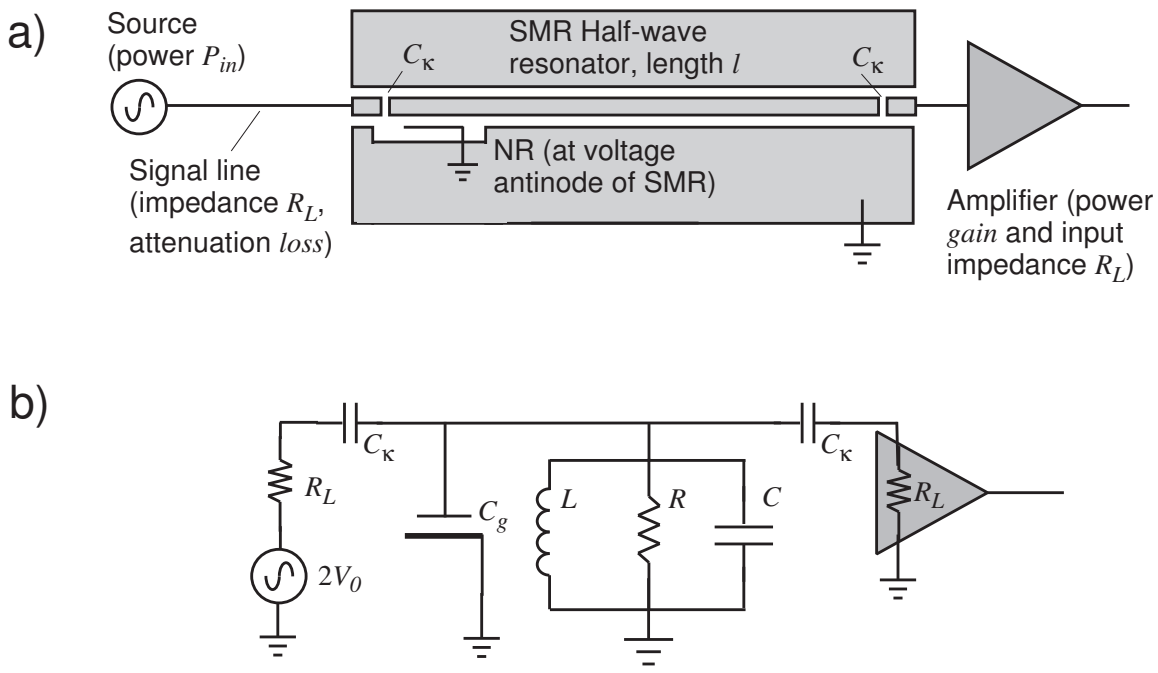

Figure 2.5: Model of the superconducting resonator as a parallel LRC circuit. a) shows the schematic representation of the SR, NR system, b) shows an equivalent circuit model with the SR as an LRC and the NR as a position modulated additional capacitance.

2.3 coupling of a nanomechanical resonator to to the superconducting resonator

To act in any way with a nanomechanical device, either as a readout mechanism or to produce back-action forces, the SR must be somehow coupled to the NR. The approach we use couples the NR motion capacitively to the SR. Under the LRC approximation of the SR behavior, this has a very clear picture, shown in figure 2.5. In this picture, the NR forms a small capacitance with the SR which acts in parallel to the effective C in the LRC model. This produces a slightly modified SR resonance frequency that is dependent on the position dependent C_g with the NR.

As the capacitance between the NR and SR is directly modulated by the NR motion, a modulation of the SR resonant frequency is produced. This in turn modulates any driven oscillation in the SR, producing a versatile NR measurement system of a type that's been studied extensively for decades from the perspective of basic position measurement, eg [9]. In recent years, the back-action dynamics of the oscillating electrics fields in the SR upon the NR has also been the subject of some interest [37, 69, 70].

Figure 2.6 shows a schematical diagram of the position measurement scheme we use for measurement and cooling of the NR. A single microwave tone is applied to the cavity red-detuned, or lower in frequency, from the the cavity center by the frequency of the NR. The NR motion then produces sidebands on this signal at $\omega_p \pm \omega_{NR}$. The lower sideband signal is suppressed due to the cavity response, while the upper sideband is enhanced; this upper sideband is the signal that is measured.

When pumping the SR at $\omega_p = \omega_{sr} - \omega_m$, the motion of the NR preferentially scatters microwave photons to frequency ω_{sr} due to to the SR Lorentzian enhancing up-convertion scattering rates over down-conversion. This process extracts one radio-frequency NR quantum for each up-converted microwave SR photon, damping and cooling the NR motion[35, 38, 69, 70]. This cooling process is analogous to both Raman scattering and the process used to cool an atomic ion to the quantum ground state of motion such as in [16, 69].

From [38], we have the rate of this up-conversion process given by: $\Gamma_{opt} \simeq 4x_{zp}^2 g^2 \bar{n}_p/\kappa$, where $\bar{n}_p$ is the occupation of the SR from the pumping. This rate can be thought of as a red pump power dependent coupling, connecting the NR to an effective non-thermal bath of the SR. As the optical damping to the SR is

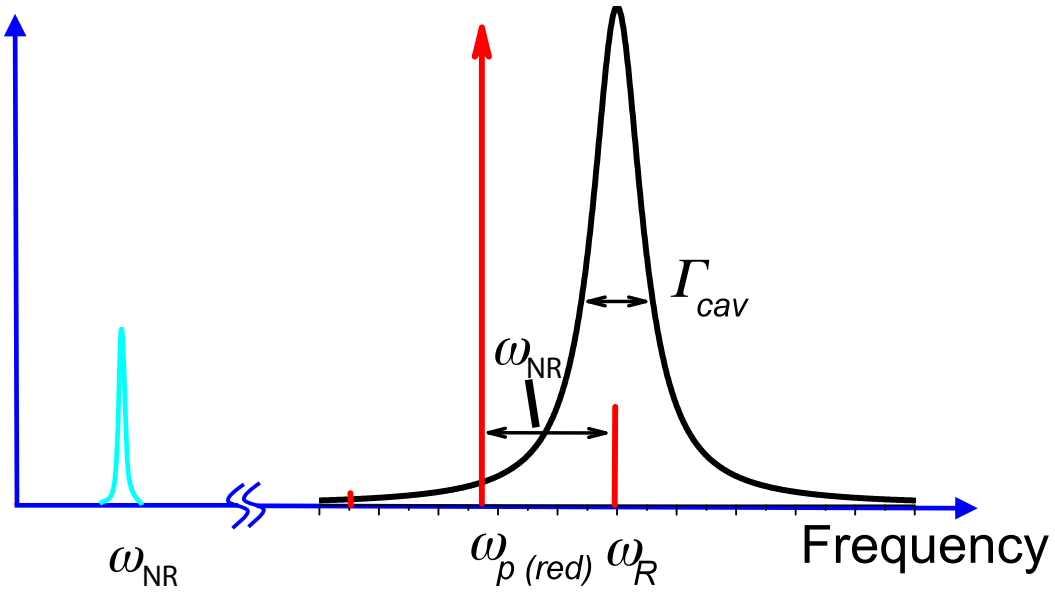

Figure 2.6: Schematic diagram showing the NR sideband measurement scheme. The black curve depicts the Lorentzian response of the SR. The red arrow at at lower frequency than the SR peak depicts the microwave pump signal. NR motion, shown for reference in teal at a much lower frequency, produces a weak sideband at the SR cavity frequency, shown as the smaller red line. The lower sideband is significantly reduced from the upper one due to the Lorentzian response.

increased, phonons leak from the NR to the SR, producing a lower equilibrium effective temperature of the NR.

This processes can be modeled using the simple detailed balance equation. In this model, the NR occupation factor follows a weighed balance of the damping rates time effective occupations of the thermal bath and optical bath:

$$\bar{n}_m = \frac{\Gamma_m^T \bar{n}_m^T + \Gamma_{opt} \bar{n}_{sr}}{\Gamma_m^T + \Gamma_{opt}} \tag{2.27}$$

where $\bar{n}_{sr} = (\kappa/(4\omega_m))^2 + \bar{n}_{sr}^T[1 + 2(\kappa/(4\omega_m))^2]$ is the effective occupancy associ-

ated with the SRs back-action when $\Gamma_{opt} < \kappa$[17]. The first term in the expression for $\bar{n}_{sr}$ is due to the quantum fluctuations of the pump field, and the second term is due to the thermal occupation of the SR, $\bar{n}_{sr}^{T}$. These expressions indicate that the minimum mechanical occupation possible is the effective occupation of the SR.

2.3.1 Strong Coupling Limit

The detailed balance relation correctly predicts the effect of coupling to the microwave cavity and resultant cooling for optical linewidths less than microwave cavity linewidths, and is predicated on assumption that the SR and NR behave as two independent but weakly coupled resonators. In the case where coupling of the microwave field to NR motion becomes comparable or dominates cavity linewdith, $\Gamma_{opt} > \kappa$, this approximation begins to fail as the NR-SR systems begins to form dressed states.

Entering this strong-coupling regime has a number of implications on cooling and measurement. Firstly, as the coupling is turned up, the mode hybridization causes peak splitting, which can be directly seen in the measured power spectra and complicates the measurement picture. Secondly, the effective damping of the NR to the SR bath reaches a limit and not longer increases with increasing coupling. This stops further cooling. This limit has been recently reached with a similar system using an optical cavity and is discussed in more detail in [24].

In the devices in this dissertation, even at the highest pump powers the NR-SR system is far from the turn-on of these strong coupling effects. For a typical

device, damping to the SR might be at highest 30KHz, while SR linewidth is hundreds of KHz. As such, these experiments are at least an order of magnitude away from any limit where this would affect cooling or analysis and the relations in section 2.3 can be safely used.

2.4 Calibration and cavity photon measurement

In order to relate real-world measured spectra to quantum occupations it is necessary to be able to convert the output power from the sample at the top of the fridge to intrinsic photon occupations in the SR. Using the coupling of the SR to the external waveguides as in the previous section, one can relate measured powers to SR cavity occupations. From a circuit model [49], it is possible to directly derive the power in sidebands generated through nanomechanical motion modulating the SR capacitance.

$$P_m = P_{in} \cdot \frac{4\kappa_R\kappa_L}{\kappa^2 + 4(\omega_p - \omega_{SR})^2} \left(\frac{1}{2C}\frac{dC_g}{dx}Q\right)^2 \cdot 2\left\langle x^2 \right\rangle \cdot \tag{2.28}$$

$$= P_{in} \cdot \frac{4\kappa_R\kappa_L}{\kappa^2 + 4(\omega_p - \omega_{SR})^2} \left(\frac{d\omega_{SR}}{dx}\frac{1}{\kappa}\right)^2 \cdot 2\left\langle x^2 \right\rangle \cdot \tag{2.29}$$

$$= P_{out} \cdot \left(\frac{d\omega_{SR}}{dx}\frac{1}{\kappa}\right)^2 \cdot 2\left\langle x^2 \right\rangle \cdot \tag{2.30}$$

Where P_{in} is power incident on the input of the cavity, P_{out} is power directly at the output of the cavity, κ is total cavity linewidth, and $\kappa_{ext} = \kappa_R + \kappa_L$ is linewidth due to the external loading of the cavity by the two end coupling capacitors. It is generally assumed that $\kappa_L = \kappa_R$.

Extracting the number of microwave pump photons in the cavity is done

through the relation:

$$\bar{n}_p = P_{in}\frac{4\kappa_R\kappa_L}{\kappa^2 + 4(\omega_p - \omega_{SR})^2}\frac{1}{\kappa_R}\frac{1}{\hbar\omega_p} \tag{2.31}$$

$$= P_{out}\cdot\frac{1}{\kappa_R}\cdot\frac{1}{\hbar\omega_p} \tag{2.32}$$

where it is assumed that $\kappa_L = \kappa_R$. Through careful measurements of total loss/gain in measurement system from the output of the cavity to the spectrum analyzer, as well as by calibrating background noise levels with known noise temperature of the HEMT amplifier, we can determine P_{out}. Ideally, if the superconducting resonator is dominated by external loading, $\kappa_{ext} = \kappa$ can be directly measured through swept transmission measurements of the cavity[27]. However, if the sample has some degree of additional internal loss, this also requires a careful measurement of κ_{ext}.

To determine κ_{ext} the nanoresonator is used as a calibrated energy source. Given a coupling to the cavity of $\Gamma_{opt} = \Gamma_{tot} - \Gamma_m^T$, the total power that escapes out the output port of the cavity is given by:

$$P_{sideb} = \hbar\omega_{SR}\bar{n}_m\Gamma_{opt}\left(\frac{\kappa_R}{2\kappa}\right) \tag{2.33}$$

Using this to extract κ_R and comparing over a broad range of nanoresonator mode temperatures and Γ_{opt} gives consistent results. With this, it becomes possible directly relate $\bar{n}_p$ to measured output power using eq. 2.32. In a similar fashion, one can measure $\bar{n}_{SR}$.

CHAPTER 3

EXPERIMENTAL SETUP

3.1 Dilution Refrigeration System

The vast bulk of the experiments described here were preformed on an Oxford Kelvinox 400HA dilution refrigerator. This system was purchased and installed in parallel with the developments of the experimental devices and systems described in this thesis, and constituted about a year of labor in the furtherance of this thesis work. Setting this system up included orchestrating the general infrastructure needed: vacuum pluming, pump rooms, ect; as well as the design and construction of a series of vacuum handling systems. All measurements preformed below 1.2K were done on the dilution refrigerator.

The dilution refrigeration system itself was housed in a large screen room: an EM shielded metal room. This served to isolate the experiments from any potential EM noise sources in the environment. Great care was taken to isoloate as much as possible the dilution fridge and circuitry from external equipment. The pumps were housed outside of the room, as was much of the signal generation and measurement equipment. Whenever possible, equipment in the shielded room was powered only on DC provided by a large battery bank. Due to line losses, the microwave sources were required to be housed in the room, but aside from this there were no wall-powered devices.

3.2 Fridge Wiring

There are several, sometimes conflicting, criterion for the wiring of the dilution refrigerator for these type of experiments. The primary goal is to route the signal lines needed for the experiment down to the sample stage such that the lines themselves do not produce significant total heat load to the fridge stages. Use of moderately non-thermally conductive materials is key, but these materials are often somewhat lossy. In addition, significant filtering is often needed to shield the samples from room temperature noise sources. A schematic of the wiring used can be seen in figure 3.4 and will be explained in detail here.

3.2.1 High-bandwidth Lines

For the experiments discussed in this dissertation, the primary signal signal path consisted of a pair of high bandwidth coaxial lines configured to measure the samples in a transmission topology. The coax used was semi-rigid UT85 or UT63 cabling and used soldered SMA connectors which provided reliable functioning to 18GHz in a cost-efficient manner. The challenge in using coax down to millikelvin temperatures here is threefold: thermalizing the inner conductor, reducing heat load to the mixing stage, and removing Johnson noise from room temperature.

Thermalizing the inner conductor of coax is challenging because the entirety of the thermal connection with the cold stages is provided through the, fairly thick, teflon dielectric. At lower temperatures the phonon thermal conductivity diverges with respect to that of the electron gas which decreases only linearly

with temperature(Wiedemann-Franz), thus making it very difficult to overcome the thermal linkages to high temperatures through the center conductor of the coax. Decreasing temperatures progressively worsen this issue. At ~1K, use of the right materials and careful clamping of the outer conductor suffices; below these temperatures more advanced techniques are required.

To control the heat load on each refrigeration stage, the proper conduction material must be selected. While at higher temperatures, copper coax is predominately used for its high conduction/low loss, using this at cryogenic temperatures is impossible. For moderate temperatures (77K to 1K), the conventional approach is to trade off thermal conduction for increased losses. The commonly used materials used are stainless steel and copper-nickel(CuNi) as these both have significantly reduced conductivity.

In recent years it has become possible to get CuNi coax with silver or gold plated interior conductors. This feature greatly decreases microwave losses, while not significantly increasing thermal conductivity. In our setup, we primary used a combination of silver plated UT63 CuNI and gold plated UT85 CuNi purchased from microcoax.ltd. This coax provided a good compromise between low loss and low thermal conductivity.

At lower temperatures, the ideal solution becomes the use of superconducting lines. Significantly below their transition temperature, superconducting materials of course have their electrons bound in non-interacting cooper pairs, thus significantly reducing thermal conductivity. Couple this with high conductivity, and low associated microwave losses, and superconducting coax is an ideal material for low temperatures. In our case, we used niobium lines for connections below 1K.

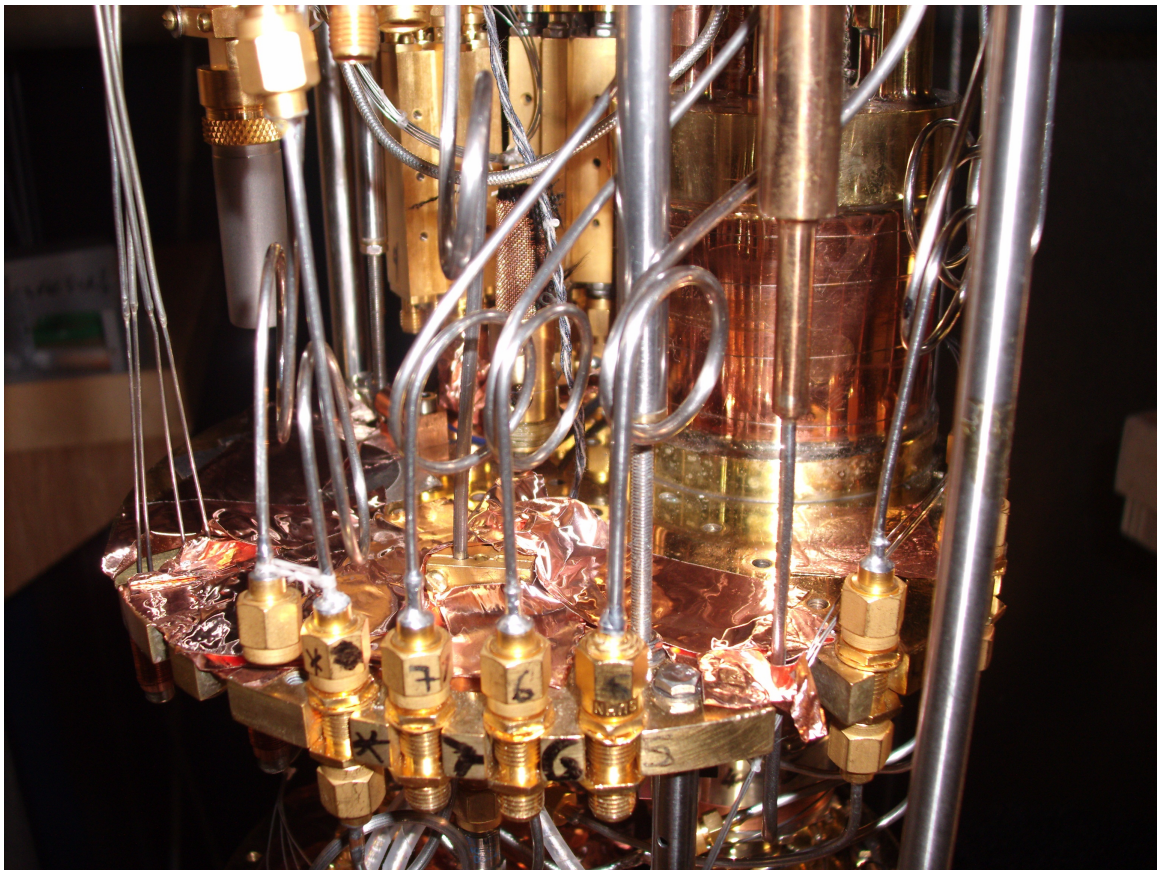

Figure 3.1: Image of example NiCu wiring on the dilution fridge. Connections at the 1K plate are shown with simple bulkhead connectors providing sufficient thermalization at these moderately high temperatures. The strain-relieving loops in the coax can also be seen.

The one disadvantage common to most of these cryogenic materials is a difficulty in soldering to them. For stainless steel and CuNi, it is possible to solder, although it requires careful surface preparation and acid flux. Niobium, however, proves very difficult to solder to. To get around this, we used crimp-on SMA connectors. This proves functional, although it provides somewhat less mechanical durability than solder joins, so care has to be taken to not over-stress or pull on the connectors. This is a particular difficulty due to thermal strain on cool-down. To help prevent this, lines were installed with a strain releaving loop in each segment, as can be seen in figure 3.1.

The second issue to consider is thermalization of the interior conductor. Again, use of stainless steel or CuNI helps with this by decreasing heat load, but it proves insufficient. The solution we settled upon is the use of what we refer to as "stripline coolers", a complete misnomer as these devices neither use striplines, nor cool in any meaningful sense. A better name might be "microstrip thermalizers". These, in essance, were simply segments of matched superconducting waveguide fabricated litiographically on silicon substrates. By having several separate waveguide chips connected via aluminum wirebonds, themselves superconducting at these temperatures, a good degree of thermal isolation was assured. These devices were mounted in sample boxes using a similar design process as that described in section 3.2.3.

The final consideration in wiring the fridge for this experiment was the attenuation of Johnson noise from room temperature. If left unfiltered, the room temperature Johnson noise from anything connected to the input line would directly impact the SR sample, thus exciting the cavity. As the SR cavity must be in its ground state as a requirement for ground state cooling of the NR, this needs to be prevented. To this end, cold attenuators were added to each stage of the wiring. Their values were chosen such that the simple attenuation would cut the incident broadband Johnson noise to an intensity lower than that produced by a resistive source at the particular temperature stage. Attenuation significantly larger than this at each stage are inherently worthless, as the attenuator itself acts as a Johnson noise source.

In this fashion, attenuators were placed at each cold stage, with the exception of the mixing stage. This stage was left unattenuated due to it's very low heat load capability: it was worried the attenuator could itself dissipate signif-

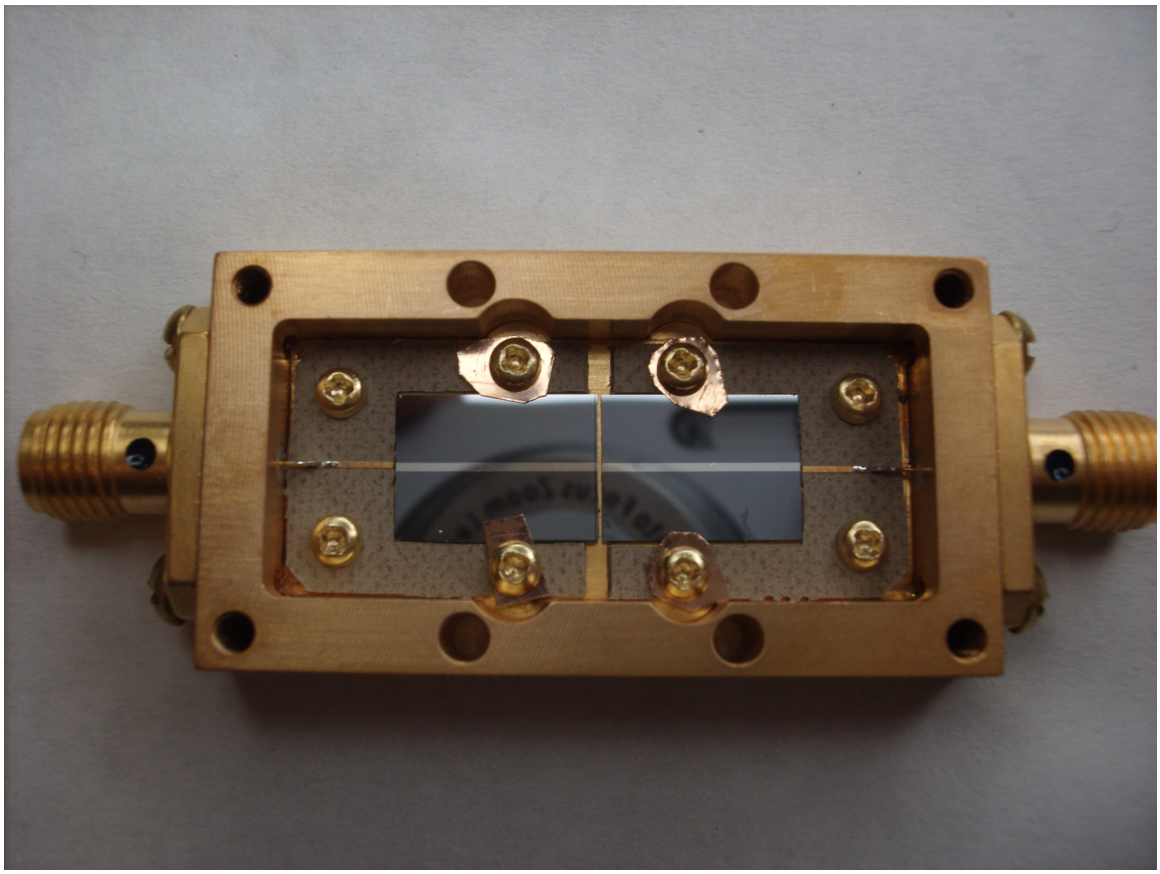

Figure 3.2: An example of a single line high-bandwidth superconducting thermalizing device. The high-resistivity silicon chips with niobium waveguides can be seen mounted in cutouts in the Arlon circuit board. The silicon devices is further split into two to maximize thermal isolation.

icant power, thus heating the stage and the sample. The final incident Johnson noise was then equivalent to less than 150mK, which corresponds to less that 0.1 quanta excitation of the SR.

3.2.2 Low-bandwidth Lines

While the majority of measurements preformed in this thesis made use of the high speed coax lines, low-bandwith lines were also installed for diagnostic and low frequency measurements. The setup used for the experiments here con-

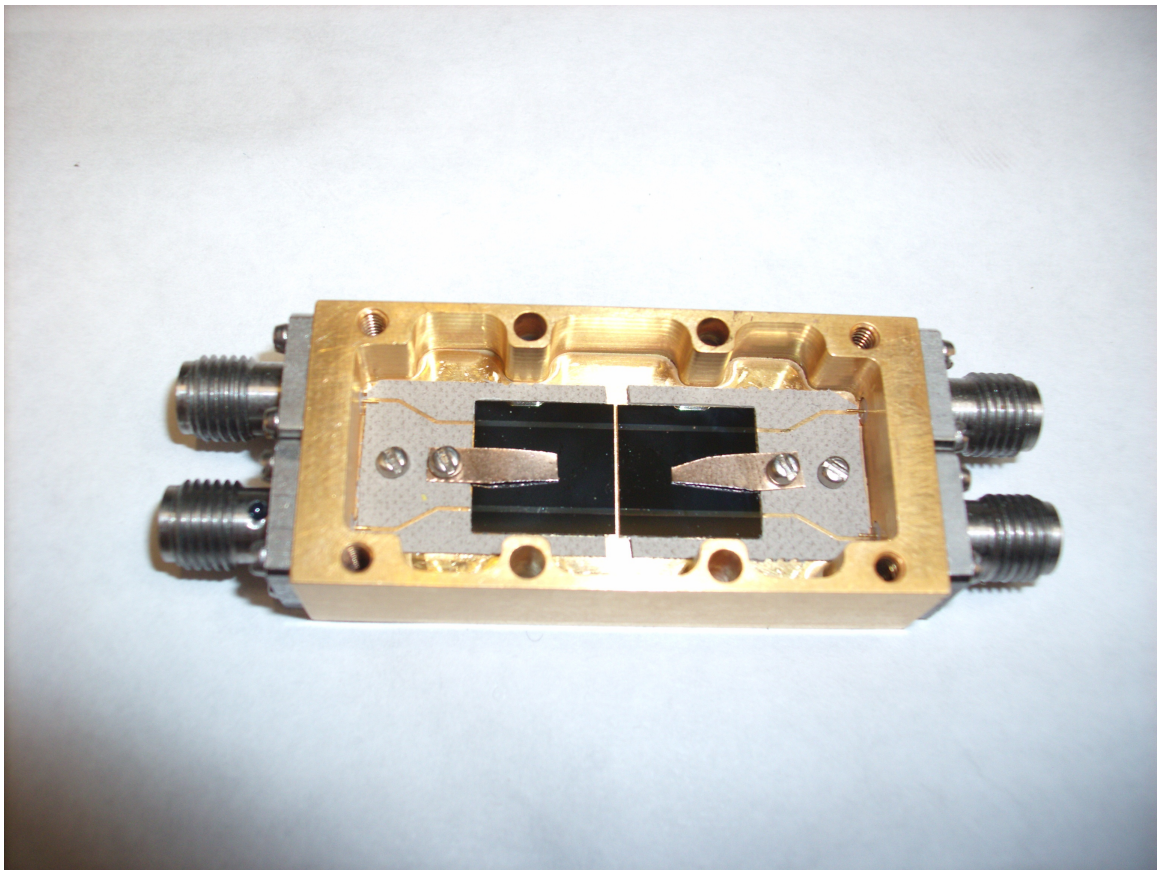

Figure 3.3: An example of double line high-bandwidth superconducting thermalizing device. Similar to the single line device, this design uses less valuable fridge space at the expense of slight crosstalk between the two signal paths.

sisted of UT15 microcoax lines made of stainless steel thermalized at each cold stage and run through power filters at 1K and at the mixing stage.

The microcoax was chosen for a number of reasons. As opposed to the twisted pair used in many other low frequency cryogenic experiments, The coax form significantly reduces cross-talk and increases shielding from stray noise. The lines low thermal conductivity and thin teflon dielectric also allowed for easy thermalization. Finally, the high loss quality of such lines, due to their small conduction area and stainless construction, was benificial to attenaute high frequency signals which were neither wanted nor needed for these circuits.

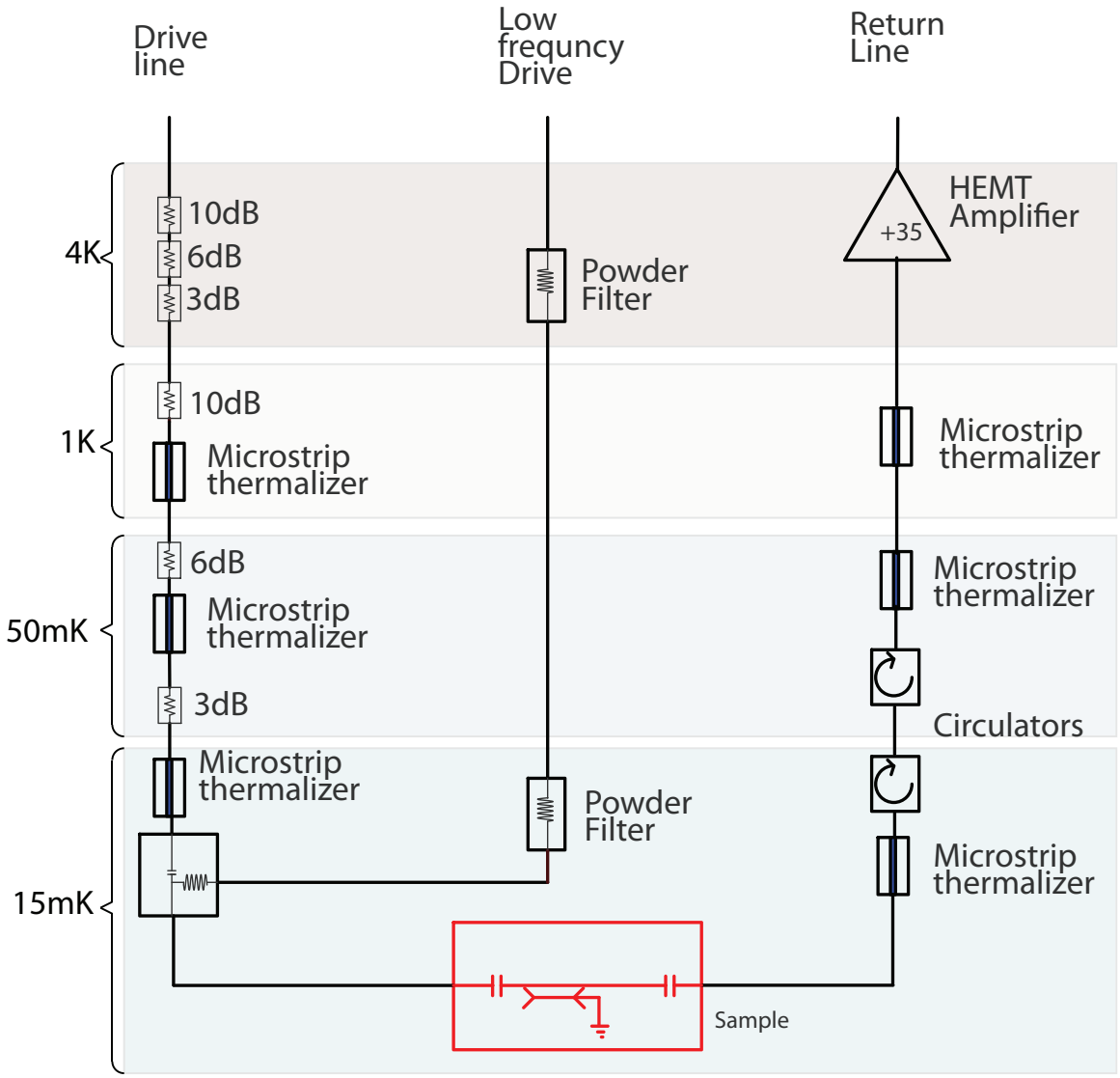

Figure 3.4: Wiring diagram of the dilution refrigerator.

The powder filters were of standard construction such as presented in detail in [3]. The basic design consisted of a gold plated copper body with four chanels drilled through it. Approximately 1 meter of manginin wire was coiled and inserted into each channel. SMA connectors were soldered to each end, and a slurry of copper power mixed with Stycast epoxy was used to fill any remaining space. The resulting filter had a 3dB bandwith of ~100MHz and dropped to better than 100dB of isolation above 2GHz.

3.2.3 Sample Boxes

All microwave signals in the experiments in this dissertation are carried by coaxial lines using SMA or compatible connecters. In order to interface these signals with the actual samples of interest, a small silicon chip, we need a sample mount and connection system. A well designed such system should ideally couple signals to the chip using impedance matched waveguides, to minimize reflections, and have maximum intrinsic isolation between input and output ports. That is to say, parasitic coupling between input and output port not transmitted through the sample should be small.

The solution used here is shown in 3.5 and made use of an OFHC copper sample box. Signals are coupled in through panel mount SMA connectors with extended dielectric. The extended dielectric allows the center pin of the coax to continue to be 50ohm matched through the copper box wall. The box is designed with the smallest dimensions possible in an attempt to push any cavity modes to the higher frequencies. These box resonances tend to couple to signals on the input and output connectors, thus reducing isolation.

Inside the box is mounted a specially constructed circuit board with a 50 ohm coplanar waveguide to which the center conductor of the connectors is soldered. The board is constructed of the special PCB material, Arlon, made by Rogers inc. The Arlon material chosen is a ceramic composite designed to have low loss and a high dielectric constant of ~$10\epsilon_0$, similar to that of silicon. This allows waveguides patterned on the Arlon to be of similar dimensions to those on silicon chips, thus making possible better matched connections. The PCB's were gold plated with a full ground plane on the bottom side. In addition, numerous vias were added to help keep the top and bottom ground planes tied

to each other and prevent slot-line modes.

The actual samples are mounted in a cutout in the center of the board and held by small beryllium copper spring clips. The samples used in these experiments were all 3.5mm x 10mm in dimension. Connections are made using aluminum wirebonds. The input and output lines are bonded with around 6 wirebonds for reliability. In addition, wirebonds every ~0.5mm were added to keep the ground planes well grounded. This was certainly overkill, but was easy enough to do, and gave reliable operation, even if some bonds failed.

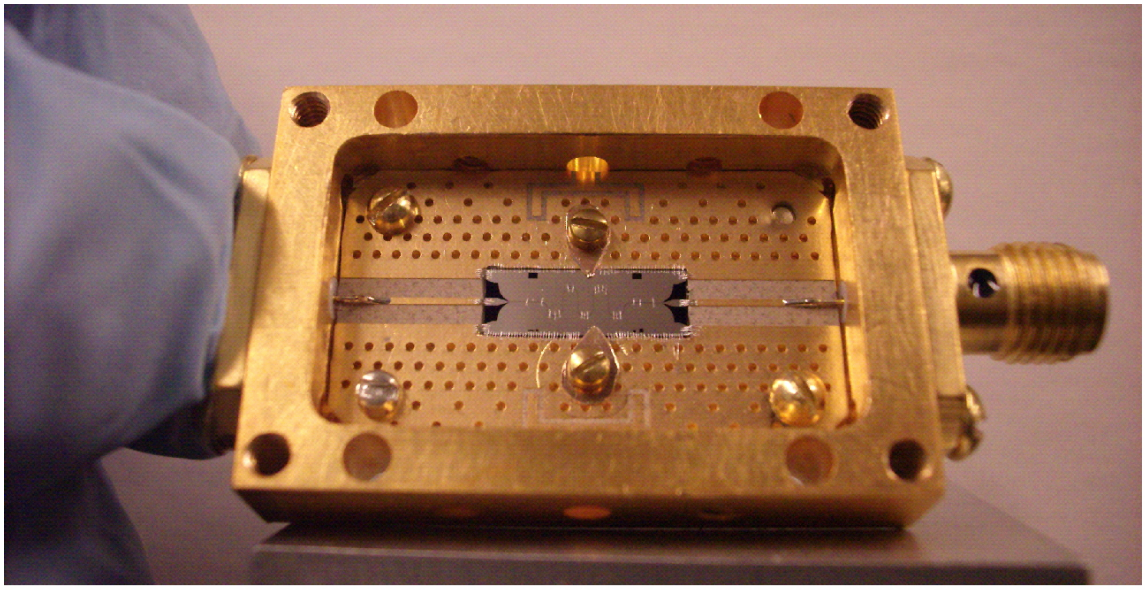

Figure 3.5: Image of assembled sample box and sample. The center pin of the SMA connectors are soldered to an Arlon board mounted in the box. A sample device is seen mounted and wirebonded in the cutout a the center of the Arlon board.

3.3 Electronics

The high frequency and precision nature of these experiments necessitated a variety of high-end electronics. A brief coverage of the main pieces of equipment

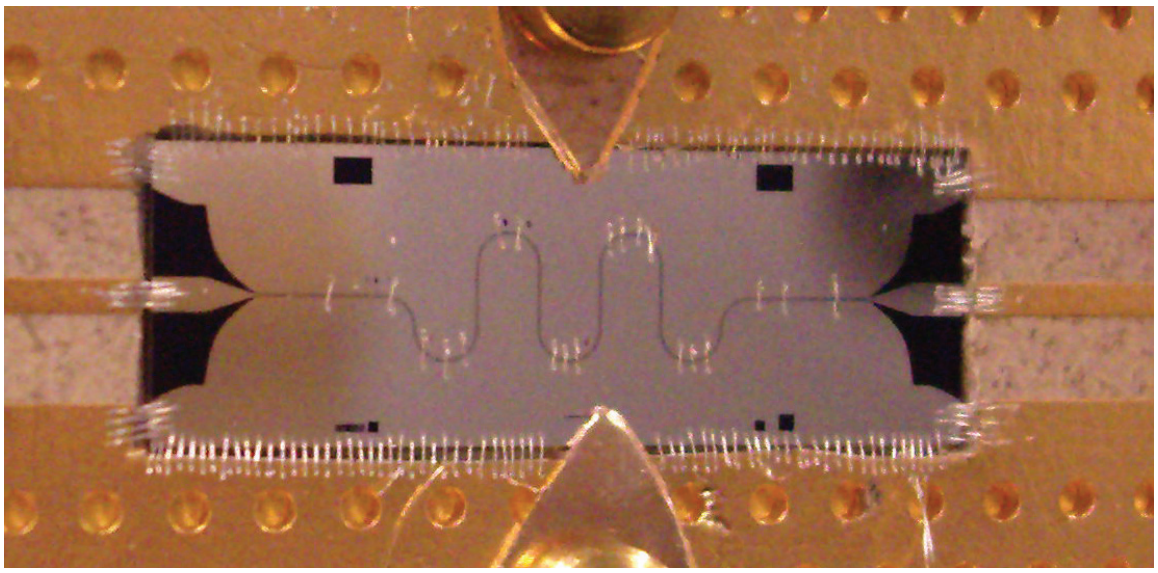

Figure 3.6: Close-up image of the sample mounting and wirebonding. The sample is mounted in a cutout in the Arlon board and wirebonded with many aluminum wirebonds. The number of bonds shown is overkill, but done for maximum reliability.

used is detailed here.

For the microwave probe signals, high precision sources with high max output power and lowest possible phase noise were needed. For initial experiments a Rhodes and Schwartz microwave frequency sythesizer with a max frequency of 6GHz was used. This unit preformed well, but as expiriments progressed, it quickly became apparent that lower phase noise was preferred and, in particular, it became apparent that higher frequencies than 6GHz were needed. As such, these units were phased out in favor of Agilent 8257D units operating to 20GHz.

For low frequency signals(< 100MHz), high purity digital arbitrary function generators(AFG) were used. Textronics model AFG3252's were specifically chosen. These units allowed for a high degree of flexibility of signals with extreme controllability of parameters, in particular phase shift of multiple sine waves.

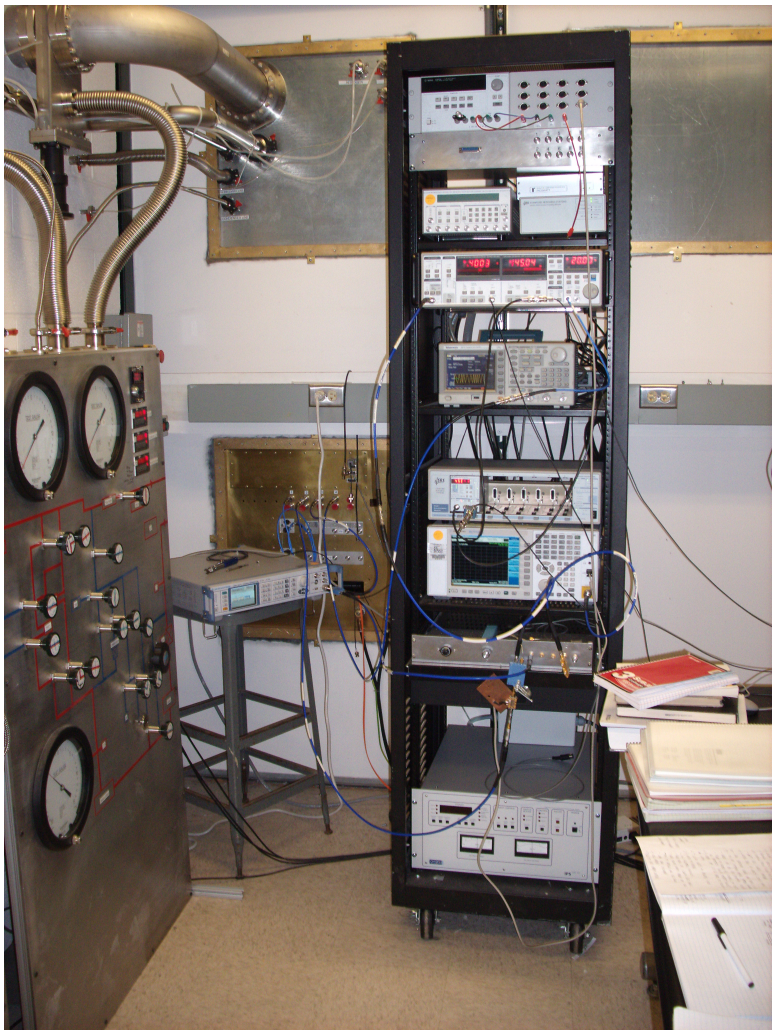

Figure 3.7: Image of the experiment electronics outside of the screen room. The dilution refrigerator pumping system can be seen on the left. The screen room wall is seen with the isolated pumping and electronic feedthrough panels. The measurement electronics can be seen on the right.

On the detection end, the primary piece of equipment was an Agilent N9020A spectrum analyzer with a 20MHz digitization bandwidth. This spectrum analyzer operated to 13.5GHz, had a low noise input preamp option, and generally had high preformance specifications for basic measurement applications. In particular, however, the ability of this spectrum analyzer to digitize wide bandwidths and preform FFT analysis was key to our measurements. A typical measurement here might require resolution bandwidth(RBW) of close

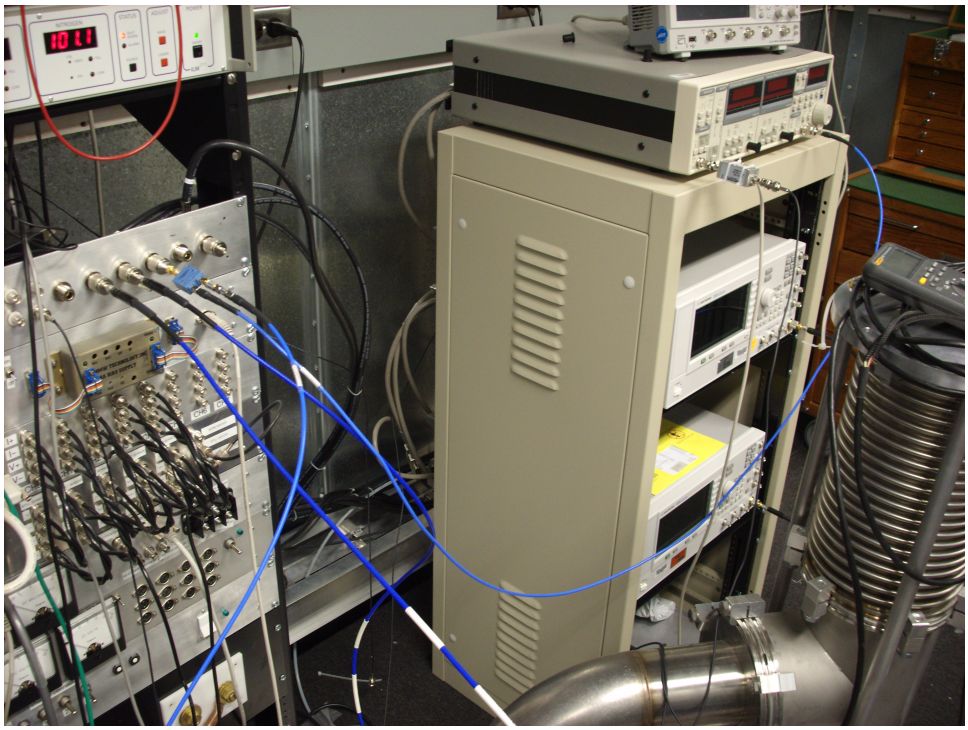

Figure 3.8: Image of the experiment electronics inside of the screen room showing the microwave sources and fridge control electronics.

to 1Hz over a measurement spectrum of 20KHz or greater, averaged for ~1000 repitions. Using an FFT based analysis, the time for one repetition is limited by the time necessary to resolve a 1Hz freqeuency separation, or ~2s, while the total simultaniously measured spectrum is limited by the digitizer . Using the more traditional swept sine measurement would take minutes for the same spectral band and resolution. Measuring very weak signals that would require weeks of averaging in a swept sine measurement are thus possible in minutes or hours with a digitizing FFT.

It's worth noting here that while the fundamental limts of a digitizing FFT spectrum analyzer are set only by the digitizer bandwidth and total time of digitization, in most stand-alone spectrum analyzers practical limitations imposed by the implementation of the internal electronics puts greater limits on perfor-

mance. In particular, in the spectrum analyzer used here, memory limits in the FPGA based FFT put limits on the RBW-measurement span product. This meant that while by the hardware specs of the analyzer it should have been possible to simultaneously digitize a 20MHz span with 1Hz resolution, a capability that would have been useful for some measurements, for such wide span measurements the RBW was required to be opened to 100's of Hz.

In order to synchronize all sources and detection equipment, a common 10MHz reference signal was connected to the ref. in ports of all equipment. This reference signal was generated by a SRS FS725 rubinium source which provided a highly accurate and drift free clock.

3.4 Phase Noise Filter Cavities

The passive attenuation and thermalization is designed to filter out room temperature johnson noise at-174dBm/Hz, however for high microwave pump drive powers, noise from the microwave source easily exceeds this. While we use the best low-noise commercial sources available, any oscillator will necessarily have some amount of noise on the output in the form of phase, amplitude and broad-band noise. For these experiments, minimal noise is required at the cavity frequency as noise, regardless of the source, produces "ring-up" and higher effective thermal occupation of the cavity. From an technical stand-point, phase and amplitude noise of a source are different things requiring careful measurements to tease apart, but for the discussions here only the total spectral density of noise away from the carrier is relevant and will be referred in general as simply "phase noise" in keeping with the specifications from the source

manufacturers.

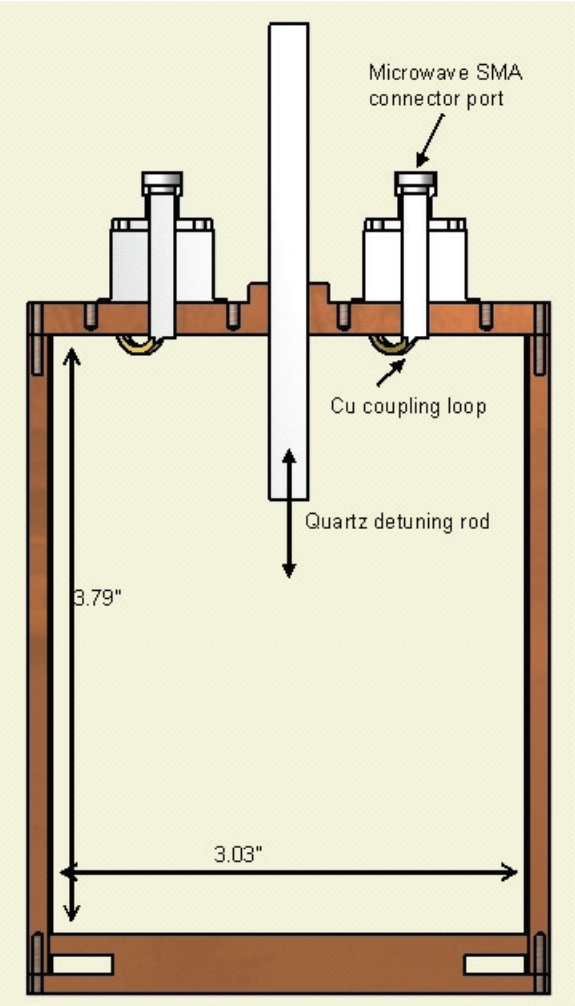

Figure 3.9: Schematic diagram of phase noise filter cavities. Coupling to external waveguides is done via small copper loops; tuning is provided by an adjustable quartz rod.

For the source we use, the phase noise at 6MHz away from a 7.5GHz signal is specified at ~-150dBc/Hz. This means that for a given output power, the spectral phase noise density is 150dB below carrier power per Hz. In addition, the source is specified to have a broad-band output noise density of -150dBm/Hz. To prevent these noise sources from heating the SR and NR, we have to filter this sufficiently to drop it below the room temperature Johnson noise, which as

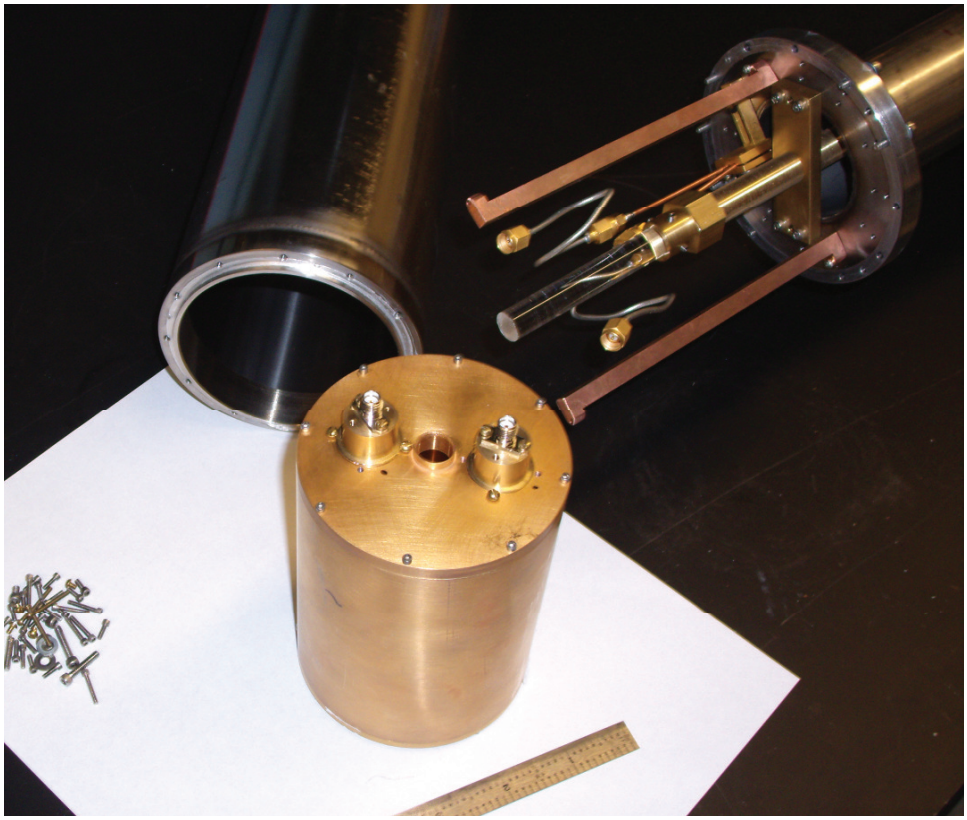

Figure 3.10: Finished, disassembled OFCH copper filter cavity probe. A 5GHz filter cavity is seen in the foreground; the quartz rod tuning aparatus and probe is on the back-right. In operation the cavity is mounted to the probe within the vacuum can, seen on back-left, and cooled in liquid nitrogen.

discussed in section 3.2.1 is filtered out through passive cold attenuators in the fridge.

At the highest power(1dB compression point), this microwave drive system can output +35dBm. As the phase noise is proportional to output power, it would be ideal for the filtering to be able to deal sufficiently with the phase noise up to this maximum value. Total noise amplitude at this power is then -115dBm/Hz, which is sufficiently larger than the broadband noise output that we need only consider the phase noise. Compare with room temperature Johnson noise at -174dBm/Hz.

Figure 3.11: Assembled filter cavity LN2 probe system ready to be cooled. The LN2 dewar used is seen on the right.

To cut phase noise from the source at this highest pump power to levels equal or less than background thermal noise, one requires greater than 60dB isolation of signals one f_{NR} away from the carrier. For a 7.5GHz carrier and a 6MHz f_{NR}, this necessitates a sharper and more accurate cut-off than generally available in commercial filters. As such, it became necessary to construct custom made filters of the neccessary quality.

The filter type decided upon was cryogenically cooled OFHC copper cavity filters. These cavities were designed to act as a multimode resonator, with the

dimensions carefully selected to produce a high Q mode at the desired passband frequency. These were chosen due to their extremely high published Q values at cryogenic temperatures(>50K reported in [2]) and their potential tunability using small dielectric pieces inserted into the cavity.

A schematic of the filter cavity design can be seen in figure 3.9.

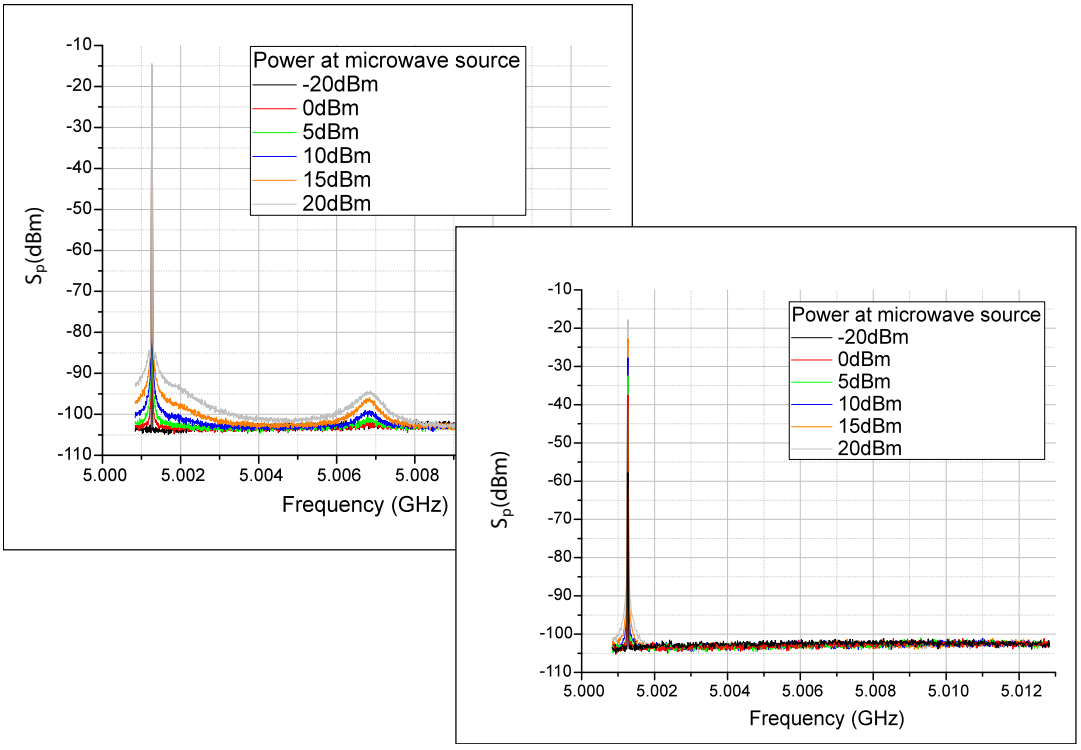

Figure 3.12: Example data showing phase noise ring-up of a 5GHz SR cavity with and without filtering. In the unfiltered rear spectra, as microwave drive powers are increased, the cavity shows clear ring-up to a level equal to hundreds of photons at the higher powers. With a OFHC cavity filter inserted inline with the microwave source, the front spectra show an absence of ring-up effects.

3.5 1K Refrigeration System.

With the move to niobium devices with a superconducting transition temperature of above 8K, preliminary measurements were possible at temperatures

above those needing a dilution refrigerator to reach. Despite the high superconducting transition temperature, In order to limit microwave loss from quasi particles the operating temperature must be several times lower than the transition temperature.

To this end, a 1K continuous flow cryostat system was also constructed with which to do preliminary measurements. This system was built in similar fashion to that described in [15] and [51]. Two high bandwidth lines made of stainless steel coax were routed to the 1K stage. In addition, 12 twisted pair were added, one of which was used to read out a LakeShore Cernox thermometer. The system was mounted in a custom built vacuum can probe affording a generous 4" diameter working space. To cool, the probe was lowered into a custom built 5" bore 9T magnet dewar system. After construction and final adjustments, this refigerator allowed operation down to ~1.4K for transmission measurements of one microwave sample up to 18GHz. For the temperatures involved, the coax was clamped at 4K and 1K but no extraordinary thermalization measures were taken.

CHAPTER 4

MEASUREMENT TECHNIQUES

The basic measurement circuit for samples on the dilution refrigerator is shown in figure 4.1. Tracing this circuit, we have two signal generators: a microwave source for generation of the GHz microwave pump signal(Agilent E8257D) and an AFG for generation of rf signals(Tekronix AFG3252). As discussed in 3.4 the microwave signal is amplified and then filtered to remove phase noise and sent down a high bandwidth line into the fridge. The AFG signal, meanwhile, was sent into a low frequency line on the fridge where it was recombined with the main signal path at the mixing stage using a bias tee.

On the output side, the microwave signals from the output of the HEMT amplifier were put through an additional room temperature circulator(Ditom D3C-4080) and amplified by a low noise amplifier (Miteq AFS-04700530-07-8P-4-GW). The final output spectra were then measured by spectrum analyzer(Agilent N9020A) This circuit, or simple variations thereof, provides the basic measurement setup used for the measurements discussed here.

4.1 microwave pump sideband NR measurement

As covered in 2.3, the NR motion causes a modulation of the SR capacitance. This in turn modulates any microwave signal in the SR cavity. Driving the cavity with a single tone, this modulation creates sidebands on the signal which can be used to read out the nanomechanical motion. This type of measurement forms the basis for most of the experiments here.

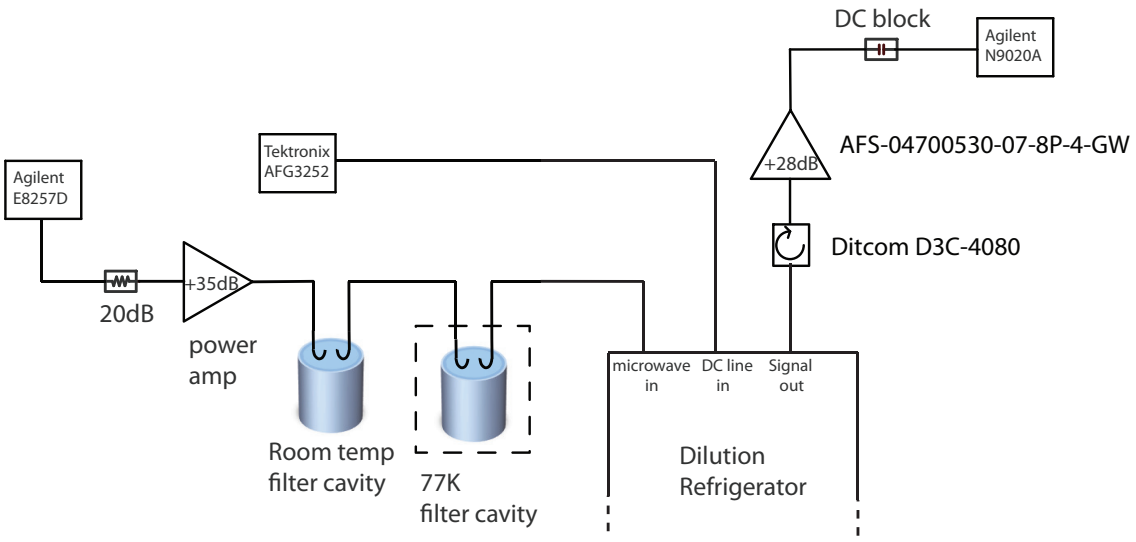

Figure 4.1: Full measurement circuit for back-action cooling experiments. While several slight variations of measurement circuitry have been used, the shown circuit comprises all the components used in the final experiments. Previous experiments used at times only one filter cavity and no power amplifier.

The circuit inside the dilution refrigerator is shown in figure 4.2 and was discussed in part in section 3.2. In this circuit, drive signals are sent down the drive line through the cold attenuators. The combination of the cold attenauators and the phase noise filters at room temp and 77K are designed to prevent the SR from being heated due to radiation down this line. The drive signals enter one port of the sample. The other port of the sample is wired through two Quinstar QCY-050100CM0 circulators to a CITCRYO1-12A HEMT obtained from S. Weinreb at Caltech. This amplifier serves as the initial amplification stage of these measurements. It has a noise temperature of 3.5K and +35dB gain at 7.5GHz.

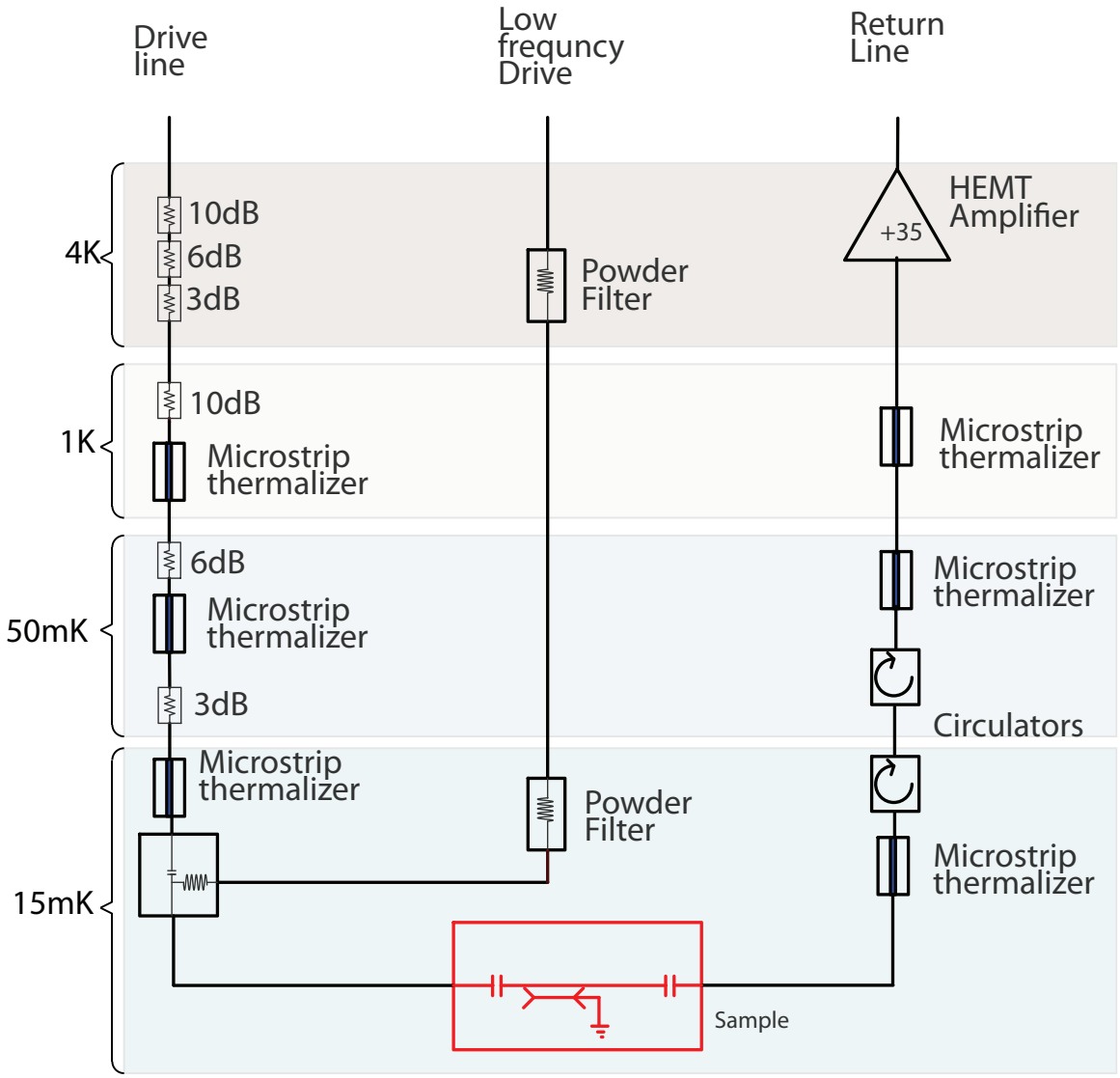

Figure 4.2: Dilution refrigerator wiring schematic.

4.2 low frequency NR direct drive

To measure the frequency and response of the NR upon first cool-down, there are several methods we have used. The first, and most straight-forward conceptually, uses a weak microwave probe signal as a position measurement combined with a low frequency direct NR drive signal. The low frequency signal can be introduced directly down the high-bandwidth lines by using either a

broadband splitter or a bias-tee. This is slightly challenging in that this requires the combining of frequencies in the single MHz with GHz frequency signals. Most splitters/summers operate in a band of only a couple octaves while the majority of bias tees are built with the intent of injecting a DC bias and as such have a DC port bandwidth measured in the KHz.

To get around this, one can use either resistive splitters or bias tees with adequate bandwidth. Resistive splitters operate in wideband down to DC, but suffer from increased insertion loss. Typically, this is unimportant for the low frequency signal, but limits applied power for the high-frequency drive. For measurement on the dilution refrigerator setup, the rf signals are introduced on a dedicated low frequency or ”DC” line which is combined with the high frequency line at the mixing state via an Anritsu K252 bias tee. These bias tees have a much higher DC cutoff than many other bias tees, and allow for signals at 6MHz to be introduced with only 6dB of insertion loss. A microwave combination device designed to combine high frequency signals in the GHz with low frequency signals up to 100MHz would be ideal and could in principle be made, but is not a general purpose device of this type is not available on the market.

We can model and estimate the force produced on the NR through a straightforward calculation. Given a low frequency AC voltage amplitude on the input coupling capacitor of the SR, V_{out}, the voltage observed on the internal SR centerline, V_{in}, is given to good approximation by the straight capacitive division produced by the input capacitor and the total SR capacitance.

$$V_{in} = V_{out}\frac{C_{coupling}}{C_{tot}}$$

This voltage is thus applied directly to the NR coupled capacitively to the SR with capacitance C_{NR}. Approximating this as a parallel plate capacitor, we can obtain the AC force magnitude felt by the NR as the derivative of the capacitor energy:

$$C_{NR} = \epsilon_0 \frac{A}{d} \tag{4.1}$$

$$E_C = \frac{1}{2} C_{NR} V_{in}^2 \tag{4.2}$$

$$F = \frac{\partial E_c}{\partial d} = \frac{1}{2d} C_{NR} V_{in}^2 \tag{4.3}$$

Where d, and A are effective plate separation and area of the capacitor, respectively, and can be estimated from SEMs of the NR. The force thus produced on the NR is proportional to a voltage squared term. In essence, this creates a mixer, the output of which is felt as force on the mechanical resonator. This can be used to produce force on the NR a couple ways, but the method we used predominately was to mix a signal near the NR frequency with a DC bias.

The circuit used for these measurement is shown in 4.3. In this circuit, an adjustable DC bias is introduced, along with an AC signal at 6Mhz produced by the AFG. Introducing the DC bias allows control of the DC bias felt on the NR on-sample. Since the low frequency lines bypass the attenuation on the microwave lines, the DC voltage is directly applied to the SR input capacitor with no attenuation to the sample input capacitor. Given the low temperature and insulating nature of the silicon in the device, the voltage then felt upon the NR can then be estimated as the ratio of SR input capacitor to total SR capacitance, for a total division of around 1000.

By stepping the rf drive in sync with a microwave probe signal such that

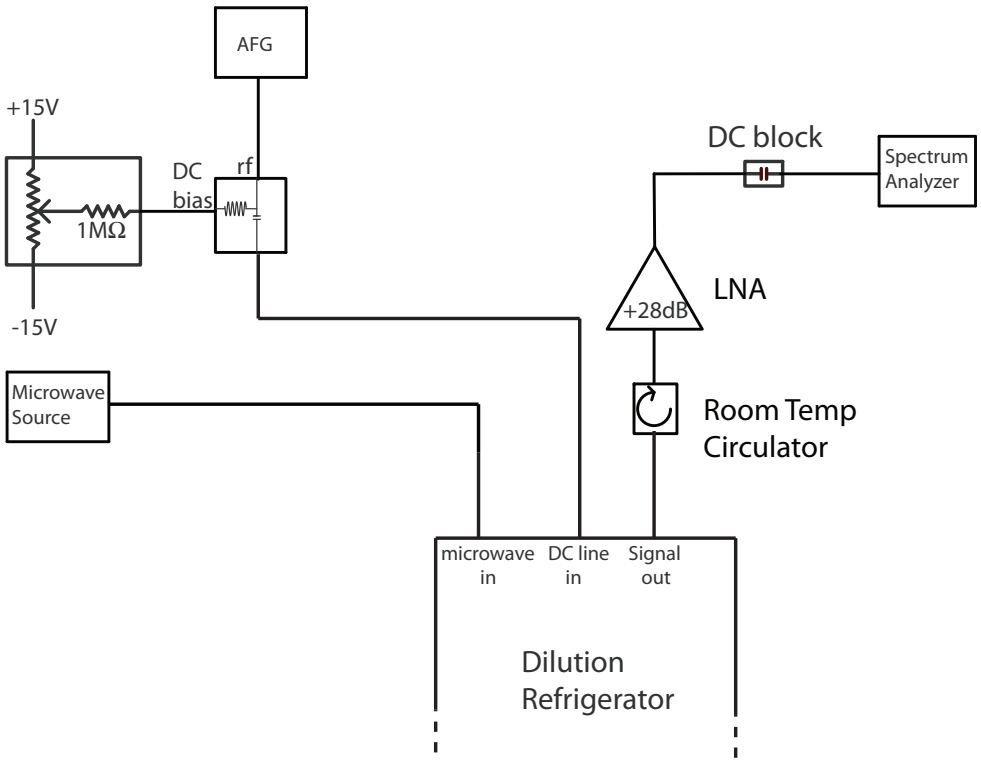

Figure 4.3: Simplified measurement circuit used for initial NR frequency finding. An additional DC bias circuit is added and phase noise filters are removed as precision NR occupation and motion is not being measured.

any NR motion generated sideband is situated at the SR cavity frequency while simultaneously measuring response at this frequency, it is possible to map out the frequencies of any mechanical resonances. Doing this type of sweep also allows direct measurement of the Q of the mechanical resonance. In addition, by driving hard enough to cause the resonator to reach a non-linear range of motion, it is possible to see the response change to that of a bistable system. For the systems we have studied, it is easy to reach this range of driving force and this characteristic response is a good indication that we see a mechanical resonance, as opposed to some other unanticipated electrical mixing term or simply noise pickup.

4.2.1 random noise driving

A similar but more advanced technique of this type used random noise, rather than a coherent sine wave, to excite the NR into high amplitude random motion. The driving of a resonator by gaussian white noise produces motion equivalent to coupling to a thermal bath, with the effective temperature given by the amplitude of the voltage noise. By measurement with an FFT spectrum analyzer, this allows for the NR response to a broad range of frequencies to be simultaneously probed, subject to the limitation of noise drive power only and not acquisition time of each frequency point.

In addition, measurement of this type allows for an easy parallel to a hot resonator with cooling produced by the red pump. This allows for both easy and quick detection of the resonator motion, as well as easy measurements of the cooling curves of the resonator.

Using the equipartition theorem and the nanoresonator's Lorentzian response to a force, we can directly derive an effective temperature T_{eff} to which a purely random force noise spectrum would drive the nanoresonator [63]:

$$T_{eff} = \frac{\omega_m^2}{4k_B k \Gamma_{tot}} S_F \tag{4.4}$$

where Γ_m^{tot} is the total(observed) linewidth of the nanoresonator and S_F is then applied force noise in N^2/Hz.

We can generate this force noise by directly applying a voltage noise to the cavity. We generate these signals using the filtered output of a high sample rate arbitrary function generator with a sufficiently long noise repetition rate to produce effective white noise. The dominant force produced by this technique

is due to mixing of the noise at the NR frequency with the DC bias.

4.3 thermal calibration

Measuring direct side-band spectra of a red probe signal gives a continuous measurement of position. While an estimate of the conversion constant can be made from first principles, as in 2.4, it is strongly desired to have a more exacting measure of this calibration. In these experiments, we do this by using the property of equipartition, $1/2k_BT = 1/2k < x^2 >$, to derive a relation of known amplitude to measured spectral power. Measuring the side-band signal at differing NR temperatures should give a linear relation from which the calibration constant can be extracted. In theory, measurement of the side-band signal intensity at a single temperature directly gives the constant, but doing an entire sweep of temperatures gives more accuracy, as well as a good demonstration of adherence to equipartition or a lack thereof.

In order to make a good measurement of the pure thermal motion of the NR, care must be exercised to not produce significant back-action through the measurement process. In the case of a weak red probe signal, the measurement scheme is explicitly designed to produce large back-action forces to cool the NR mode. In this case, avoiding back-action is done by taking a preliminary curve of thermal noise to red pump power and extracting both the effective temperature and linewidth. The effective back-action in this case is easily determined by any change in damping of the resonator. As such, our technique has been to find the red pump power where little to no linewidth broadening is observed, and then use 5 to 10 dB lower power for thermal calibration measurements.

CHAPTER 5

MEASUREMENTS AND RESULTS

Several samples have been investigated in the development of these experiments and the search for strong coupling and back-action cooling. The initial functional devices, constructed of all aluminum, that demonstrated NR readout and some back-action cooling has been previously reported in [28] and discussed in [27] and so will not be extensively covered here. Instead, the focus will be on results for the more recent and better preforming devices constructed of niobium, which have demonstrated the best performance to date, and which are functionally similar to earlier devices.

The best back-action cooling data to date was seen with the device reported in [52]. This sample was constructed of a niobium waveguide at around 7.5GHz with an SiN and aluminum nanoresonator of about 6MHz. The exact measured parameters of this device are listed in detail in table 5.

5.1 Initial Device Characterization

With this sample on the dilution refrigerator, the nanomechanical motion was observed with the setup described in section4.1. The SR frequency and Q were found using a simple network analyzer measurement. By employing the measurement scheme described in section 4.2 the NR freqeuncy was found using a swept sine signal. Once the SR and NR frequencies were determined for a run, they remained effectively constant and drift free over the course of months.

Once SR and NR frequency were known, it was possible to use single red-detuned microwave pump to read out the motion; an example spectra of the

Table 5.1: Geometric parameters of device used for backaction cooling and evasion measurements.

	Fabrication geometry, verified by inspection in SEM:	
w_{CPW}	$4\mu m$	Width of Nb centerline
d_{CPW}	$100\mu m$	Gap between centerline and ground plane
t_{CPW}	345 nm	Thickness of Nb film on SMR
l	30 μm	length of mechanical resonator
w_{NR}	170 nm	width of mechanical resonator
t_{SiN}	60 nm	thickness of SiN
t_{Al}	80 nm	thickness of Al film on NR
d	75 nm	Distance between the NR and gate
	Parameters calculated using the geometry:	
m	$2.2 \cdot 10^{-15}$ kg	effective mass of NR
k	2.70 N/m	spring constant of NR
Z_0'	126 Ω	Characteristic impedance of CPW waveguide in SR
Δx_{ZP}	24 fm	zero-point motion of the NR
	Parameters calculated from rf measurement:	
f_{SR}	$7.479048GHz$	SR frequency
κ_{SR}	$2\pi \times 600KHz$	SR linewidth
f_{NR}	$6.312MHz$	NR frequency
κ_{NR}	$2\pi \times 14Hz$	NR linewidth at 150mK
C	260fF	Equivalent SR capacitance
L	1.7nH	Equivalent SR inductance
g	$2\pi \times 84$KHz/nm	NR SR coupling constant
C_g	438aF	gate capacitance between NR and SR

NR motion generated sideband at the SR frequency is shown in figure 5.1. In this spectra, the NR motion can be seen as a sideband of up-converted photons proportional to the NR occupation, $\bar{n}_m$, on top of noise a noise background due to the HEMT amplifier as well as any thermal or otherwise excited noise in the SR. Fitting this spectra to a Lorentzian gives the total power in the thermal peak. Using a weak probe signal of this type and assuming the nanoresonator motion follows equipartition, $\frac{1}{2}k\left\langle x^2\right\rangle = \frac{1}{2}k_BT$, it is possible to directly obtain a calibration

of the sideband signal to mechanical motion and temperature as in 4.3, shown in figure 5.2.

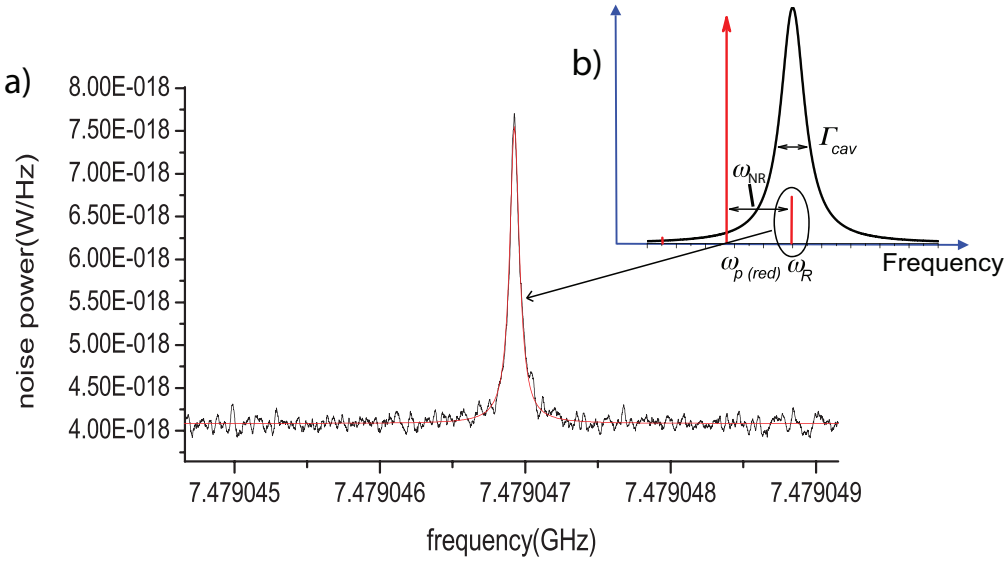

Figure 5.1: Example spectra of NR motion sideband. a) shows the direct spectra data taken from the spectrum analyzer with the NR motion produced sideband seen. b) shows the schematic representation of the measurement for reference.

5.1.1 Thermal Calibration

On the thermal calibration curve one can immediately see that the effective temperature of the NR motion follows a linear relation with fridge temperature as expected from equipartition, except for divergence below around 150mK. This phenomena has been consistently seen on every sample measured and seems to be due to some non-equilibrium force bath, perhaps charge noise related. This noise appears essentially random, though at times excessive ”ring-up” of the NR motion has been observed, presumably due to these effects, that appears somewhat history dependant. In particular, operating at a very low fridge temperature(<20mK) seems to exacerbate these problems. As such, this random

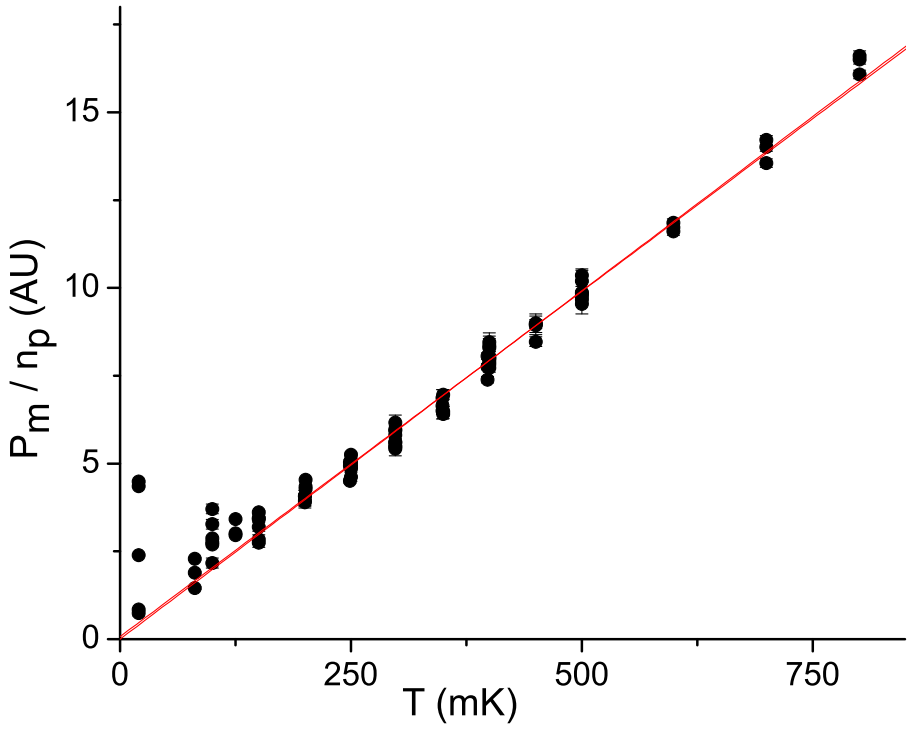

Figure 5.2: NR thermal calibration curve. The fridge temperature is varied from base temperature(15mK) to 800mK and thermal motion of the NR is measured. Above 150mK, NR thermal motion closely follows equipartition. The black line respresents a best fit of the data above 150mK and is used to directly obtain a thermal calibration of the NR.

force noise sets a practical limit on the initial temperature of the NR device for cooling. The majority of the measurements discussed here were thus done from a fridge temperature set at 150mK.

Using this calibration referenced to output power, which is directly measured, along with an estimate of the nanoresonator effective spring constant, the coupling constant of the NR to SR can be extracted, as discussed in section 2.4. The parameters needed for this calculation are directly measured, with the exception of the NR spring constant. To determine spring constant, first a best

estimate of the nanoresonator effective mass is made based upon known layer thicknesses and careful SEM measurements of beam and gate dimensions. This is an imprecise measurement as extraction of SEM dimensions is somewhat inaccurate. Using this effective mass, as well as a geometric mass conversion factor, which in our case is approximately unity [27], and then using the relation $\omega_m^2 = \frac{k}{m_{eff}}$, this gives $m_{eff} \approx 2pg$, $k \approx 3.2N/m$, and a coupling of $\frac{d\omega_{SR}}{dx} \approx 84\text{K}Hz/nm$. While this measurement does require the indirectly calculated effective mass, yielding uncertainties of about 10%, this technique has the advantage of being directly proportional to the ratio of P_m/P_{out} which is measured to high accuracy, rather than relying on any additional knowledge of line losses or gains.

5.2 Classical Back-action

With the refrigerator stabilized at T=146mK, in order to prevent extraneous ring-up of the NR, the output noise spectra was measured versus the SR red-detuned pump power. While pump power is the parameter that is directly set for each measurement, it is not a particularly good value to use in analysis. Instead, for each spectra measurement the fed-though pump power is directly measured and referred back to a cavity occupation, $\bar{n}_p$, as described in section 2.4. This value is used as the independent variable for all the relevant data in this section.

Each power spectrum, $S_x(\omega)$, can be referred to the oscillator position using the NR thermal noise calibration. Back-action correlations between the NR motion and any SR field are important in the measured noise spectra at the lowest mechanical occupation factors. Fluctuations in the SR voltage, due to noise

occupation of the SR, $\bar{n}_{sr}$, together with the pump, produce forces at ω_m. The resulting motion, again measured out with the pump signal, produces noise at ω_{sr}, however 180^o out of phase with the original SR fluctuations. This correlation results in an inverted noise peak, similar to noise squashing[48], which adds incoherently to the noise power driven by the thermal bath. The resulting observed noise peak or dip, $\bar{n}_{eff}$, is calibrated using thermal noise. 5.3 shows measurements of $S_x(\omega)$ demonstrating this effect in three cases at low occupation factors: when $\bar{n}_{eff} > 0$, when $\bar{n}_{eff} \approx 0$, and when $\bar{n}_{eff} < 0$ showing the squashed output noise.

Clearly, the back-action cooling effect is not cooling to zero temperature and then to negative temperature. In order to determine the actual cooled temperature of the NR, we must understand the contribution of the back-action correlation. To better quantify this effect, we worked with the theorist Aash Clerk. The details of the calculations involved can be found in the SOM of [52]. The end result of these calculations reveal a surprisingly simple relation: $\bar{n}_m = \bar{n}_{eff} + 2\bar{n}_{SR}$, where $\bar{n}_m$ is the actual NR occupation, $\bar{n}_{eff}$ the observed or effective occupation, and $\bar{n}_{SR}$ is the occupation of the SR due to the excessive noise.

To use this relation to extract the actual NR occupation, it becomes necessary to also measure the total SR occupation due to this additional cavity noise. This is done by measuring a widespan spectra of the SR cavity and fitting the noise to a Lorentzian to extract the total power output. Then using the calibration relations in section 2.4 allows a direct extraction of $\bar{n}_{SR}$. An example spectra of this type is shown in figure 5.4. Taking this data for a sweep of microwave pump powers yields the results shown in figure 5.5.

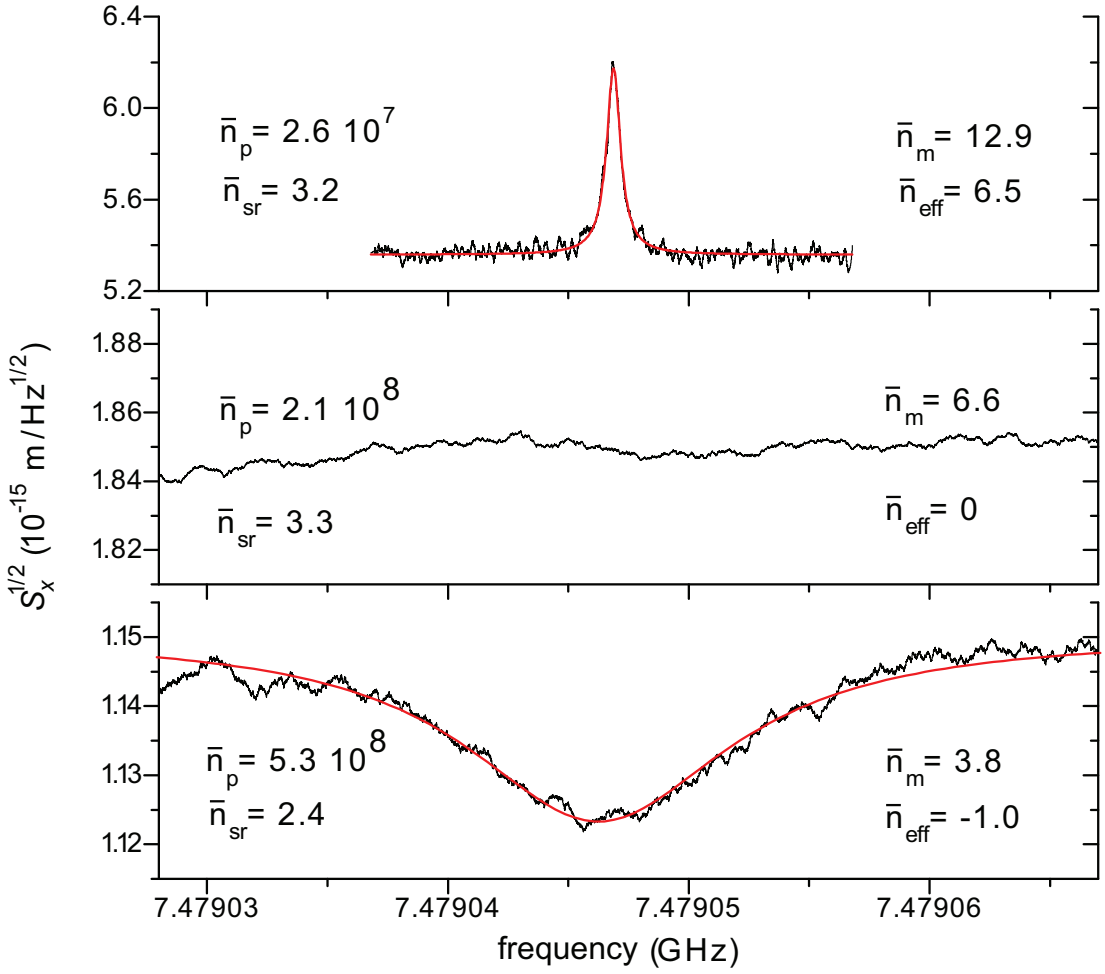

Figure 5.3: Example spectra as red pump power is increased. At lower pump power, the NR motion sideband is a normal standard Lorentzian. As power is increased, the NR thermal noise is damped and back-action effect begin to become relevant. At highest power, back-action produced correlation become dominant and a negative Lorentzian is seen.

5.3 NR Back-action Cooling

Taking the effects of $\bar{n}_{sr}$ into account in this way it becomes possible to determine the actual NR occupation vs. pump power, as shown in figure 5.6. The lowest mechanical occupation observed is $\bar{n}_m = 3.8 \pm 1.3$. In this measurement the uncertainty is dominated by the uncertainty in $\bar{n}_{sr}$. At this low occupation factor the resonator is expected to be found in the ground state with probability $P_0 =$

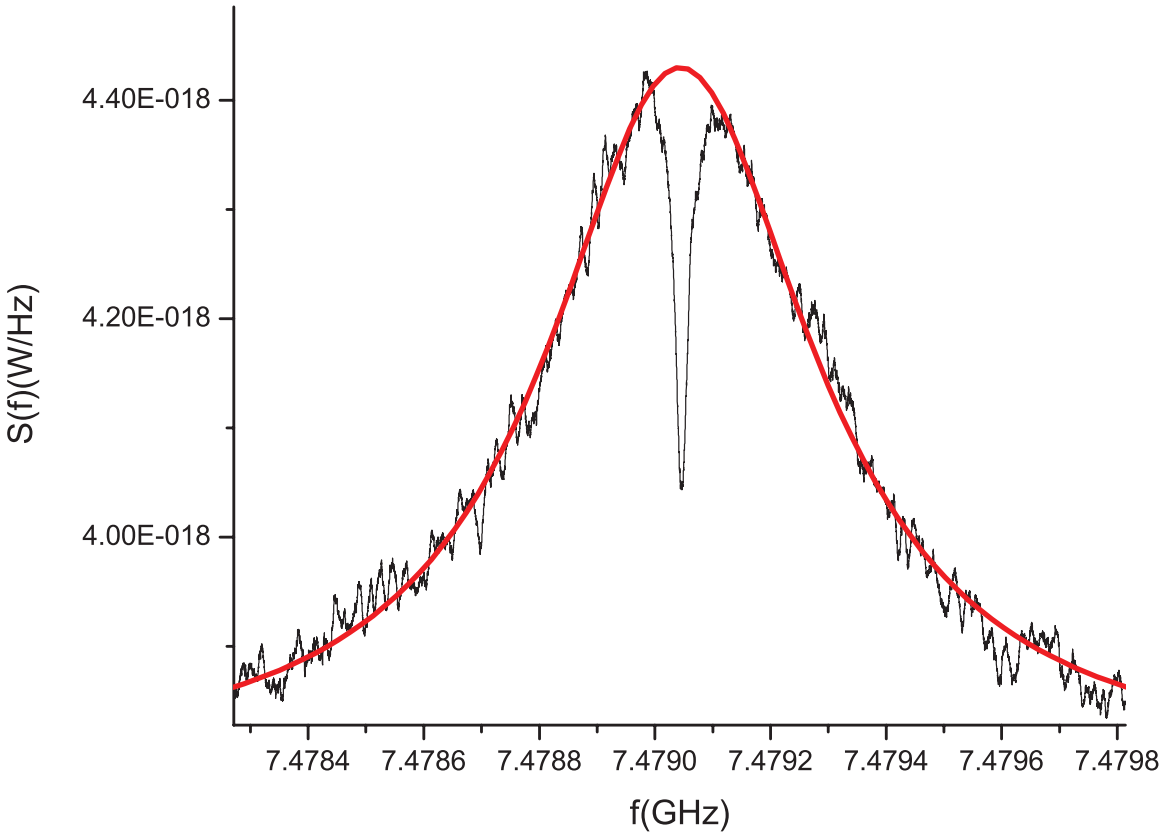

Figure 5.4: Example widespan spectrum. Both the cavity excitation and NR sideband dip can be seen for a high red pump power. The SR noise seen corresponds to an average of about three photons.

$1/(\bar{n}_m+1) = 0.21$. The overall cooling power of this as a refrigeration technique is miniscule by normal standards, estimated at $\dot{Q} = \hbar\omega_m \cdot \Gamma_{opt} = 10^{-22}$W. This should not be considered in the context of bulk refrigeration, however, but rather as the preparation of a single oscillatory mode in a non-equilibrium state.

As an additional check, the refrigerator temperature was lowered to 20mK to see if greater cooling could be achieved. Despite increased Q values of the NR and possibly lower bath temperatures, a decrease in the minimum $\bar{n}_m$ was not observed. To try to help explain or understand this, one can use the detailed balance relationship, 2.27 and the measured $\bar{n}_m$ and Γ_{sr} to compute the NR bath heating rate, $\dot{n}_T = \Gamma_m^T \bar{n}_m^T$, versus $\bar{n}_p$, figure 5.8 This bath rate is the calculated rate

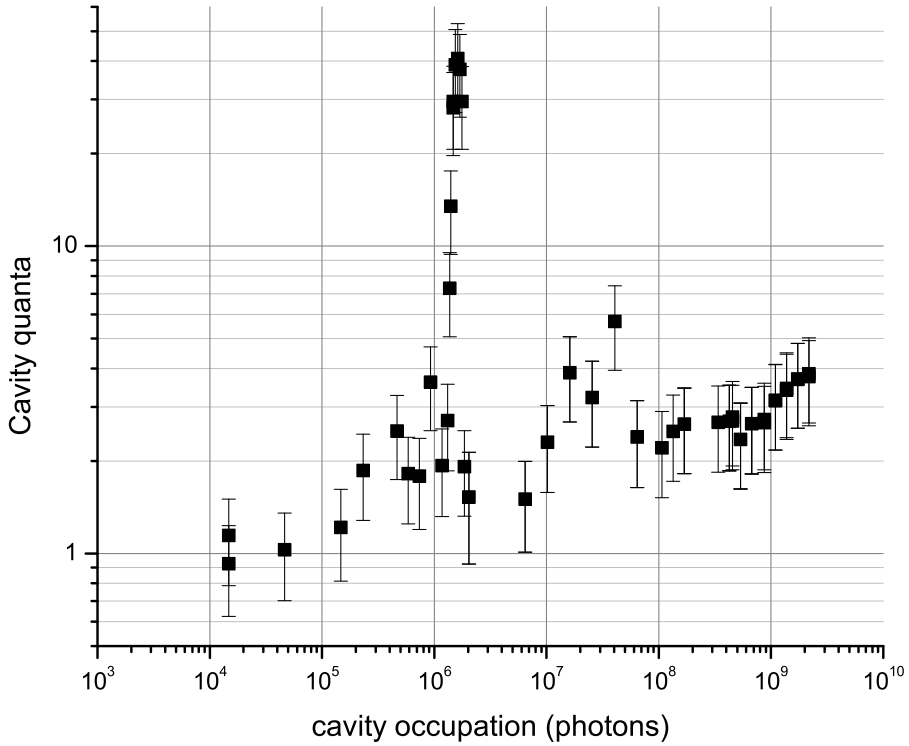

Figure 5.5: Measured cavity occupation vs. applied red pump power. As power is increased, increasing cavity occupation is seen, believed to be from dissipative effects. In addition, spikes are seen at certain powers, possibly due to a periodic oscillation of a superconducting weak link effect.

at which phonons excite the NR due to its interaction with the thermal bath. It is clear that as $\bar{n}_p$ increases above $3 \cdot 10^7$, $\dot{n}_T$ begins to increase, nullifying the benefit of starting at low temperatures. The exact source of this heating is not totally clear at this time but is major limitation to the final extent of the back-action cooling data presented here.

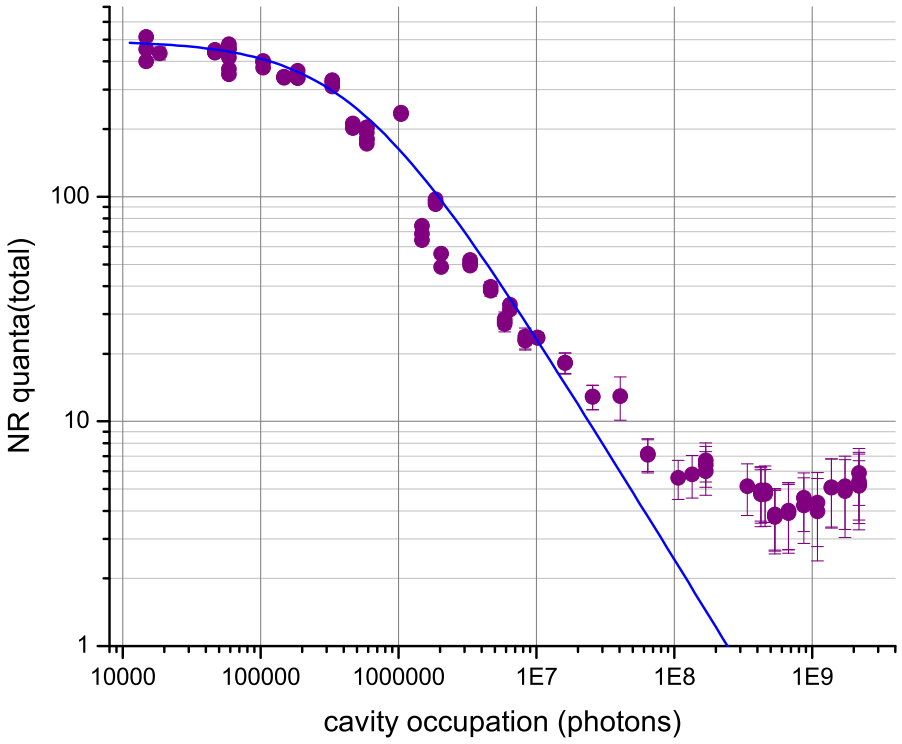

Figure 5.6: NR cooling with a red-detuned pump. NR occupation is corrected for SR occupation and back-action correlation effects. As power is increased, NR occupation is seen to fall along the theoretical cooling curve, in blue, up to a point where anomalous heating begins. The lowest occupation seen corresponds to $\bar{n}_m = 3.8 \pm 1.3$.

5.4 Calibration linearity and stability

The cooling data in this case shows clear departure from original theoretical predictions in that cavity ring-up and increased bath heating become significant factors and must be accounted for. This raises some uncertainty that other non-idealities may be causing error in the measurement of NR occupation. In addition, there is always the possibility that the calibration of spectral power density to NR motion obtained from the thermal calibration is not linear with

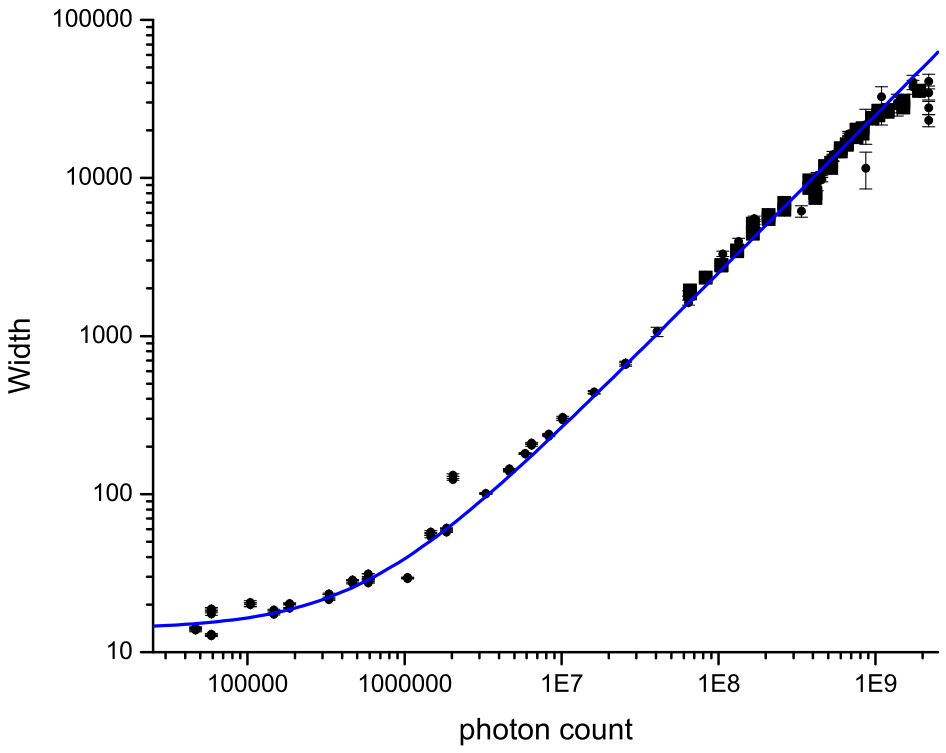

Figure 5.7: NR linewdith broadening with increasing red pump power. Linewidth is seen to broaden as expected from theory(blue line), with only some slight deviation at the highest powers.

power. This thermal calibration is taken at very low microwave drive powers, and as such could possibly not be valid for high powers for many practical reasons, eg. the SR having power dependent dissipation. To check that these concerns are not issue and that the understanding of the physics involved in the back-action interaction is correct, there were several additional measurements done.

To address any concerns that the equipartition-derived position calibration is either non-constant over time or non-linear with applied pump power a couple observations were made. First, measurement of thermal motion taken over

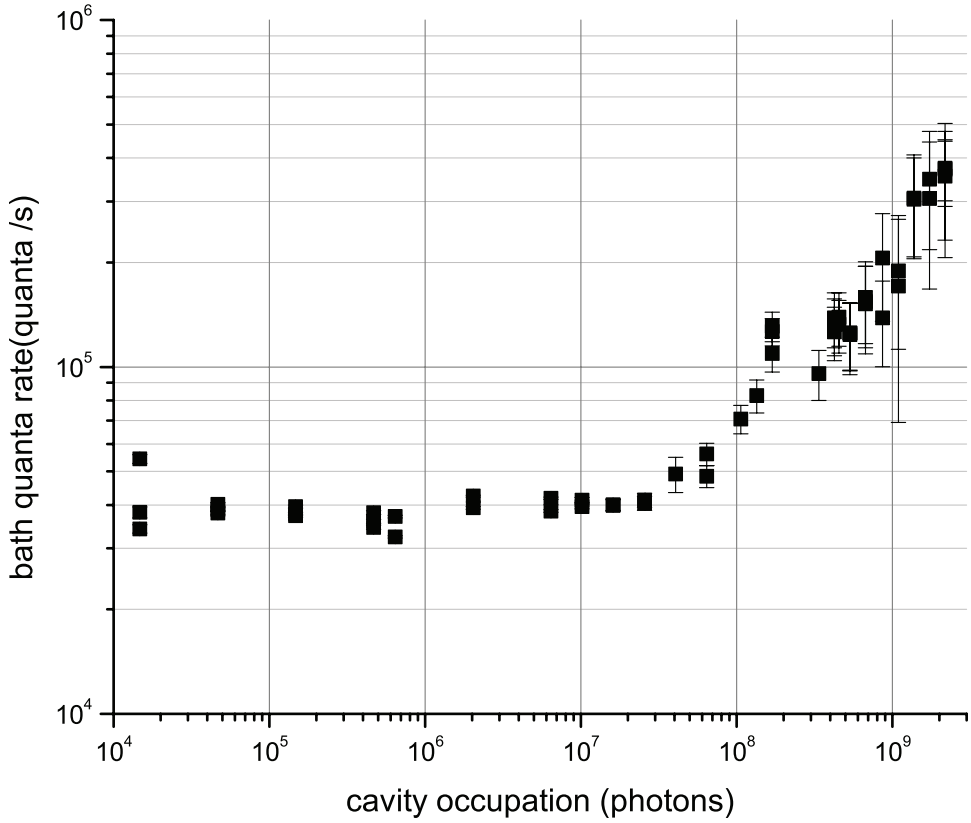

Figure 5.8: Calculated NR heating rate due to coupling to a thermal bath. For an NR experiencing only a constant damping to a constant temperature bath, this value should be independent of pump power. The upturn at around 3×10^7 pump photons indicates either an increasing bath temperature(heating) or an increased damping rate(decreased Q).

hours or days consistently follow the equipartition relation found in the thermal calibration. Even warming the sample to 77K and back to $\sim$ 150mK gave consistent behavior before and after warmup, though there were sometimes very slight shifts in frequency on order of a fraction of a percent. In addition, when the the response of the nanoresonator was observed continuously over $\sim$ 10 hours it was found to give a constant response in occupation with $< 2\%$ scatter.

Linearity of the calibration with applied pump power is also a major concern that needed to be addressed. The primary check of this was simply by directly measuring the power transmitted through the cavity at the pump frequency

during each measurement. This was found to be directly proportional to the power applied at the top of the fridge to within the uncertainties of the measurement for the range of powers used in this data, as seen in figure 5.9. While uncertainties in the source output power and spectrum analyzer measurement kept this to within about 10% accuracy, this does imply that neither cavity κ nor frequency were changing significantly with power.

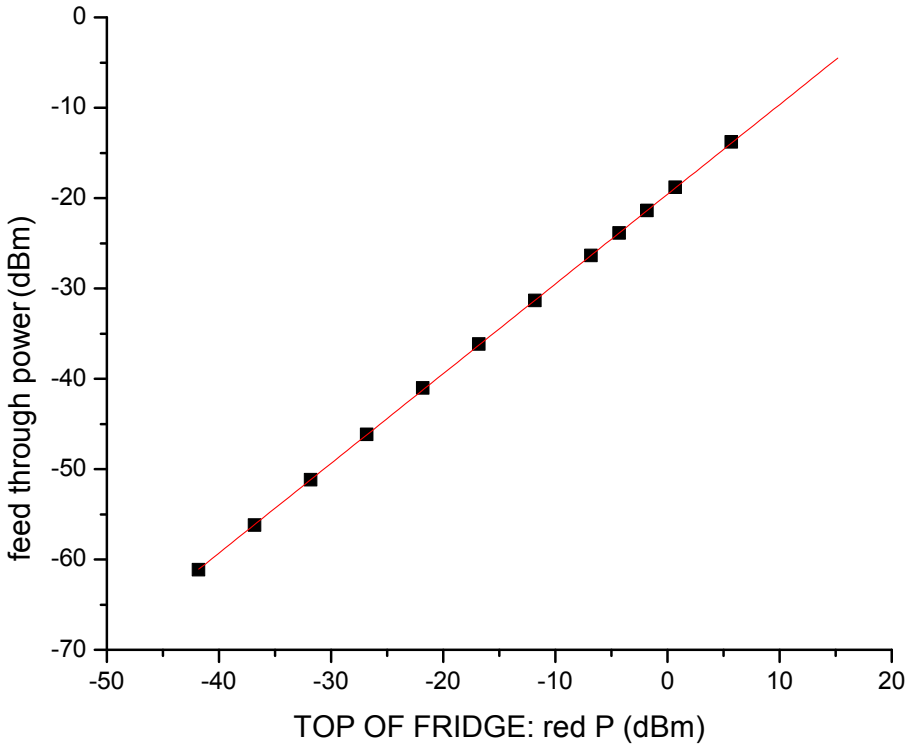

Figure 5.9: Measured power feedthrough linearity with applied pump power at the top of the dil. fridge. The highest powers correspond to the highest SR cavity occupation($\approx 2\times10^9$ photons) and follow a linear trend to within specified errors of the microwave source and spectrum analyzer.

5.4.1 Other Measurements

In addition, the transmission response of the cavity was directly measured using a network analyzer while adding in the red pump. From this, it was determined that cavity frequency was unchanging, while κ actually decreased by $\sim \pm 2.5\%$ from lowest to highest power. This effect of decreased losses with increased power is well known, e.g. [21].

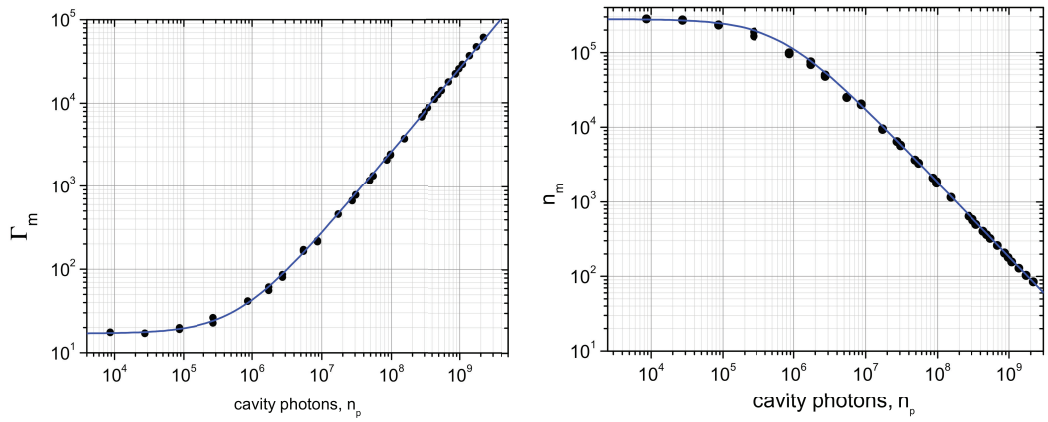

Figure 5.10: Back-action cooling of the NR driven to a high effective occupation by applied random noise. The NR is driven to an effective temperature of ~70K by continuous random noise produced by an AFG and cooled by back-action. Measured linewidth and occupation follow theoretical curves very accurately in this situation.

Some samples were also driven at higher powers beyond the point at which best cooling was seen. In this case, there became noticeable deviation of fed-through power from applied power at the top of the fridge, due seemingly to a combination of increasing SR cavity loss and the begining of saturation of the HEMT amplifier. The power at which this effect became significant(greater than 10% decreases) was at several dB higher than that used in the data shown here. Certainly this could be an issue with increasing powers, but it did not seem to affect the accuracy of coldest point measurements here.

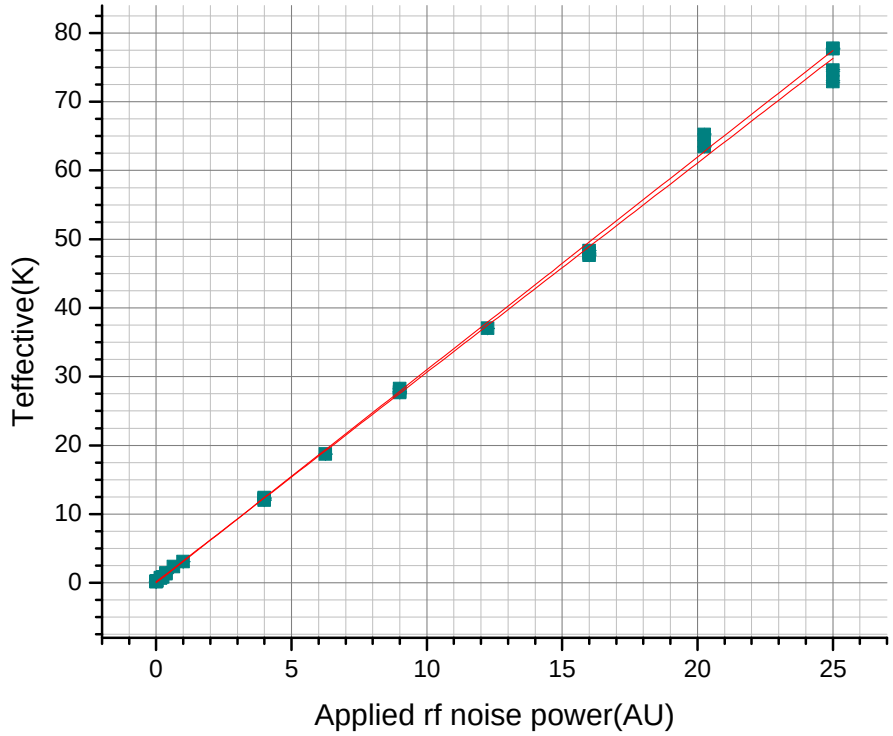

Figure 5.11: Measured effective temperature of the NR due to random noise driving. The effective temperature is seen to linearly follow the applied noise power, as expected for a directly applied force noise as in section 4.2.1.

To check the behavior of the system (NR and SR) in a limit where $\bar{n}_{sr}^{T}$ was not a complicating factor, radio-frequency electrostatic force noise at the NR frequency was also applied as described in section 4.2.1. At low red pump power, this force noise excites the NR to a large effictive thermal temperature. Starting from $\bar{n}_m = 2.5 \cdot 10^5$, cooling by a factor of 3000 to $\bar{n}_m = 80$ was observed, which closely follows the expected cooling curve over the full range of $\bar{n}_p$ 5.10. This follows the theoretical curve and gives strong indication that the back-action and cooling behave as expected. This suggests that the increase in bath rate at high pump power is due primarily to an increase in bath temperature and not

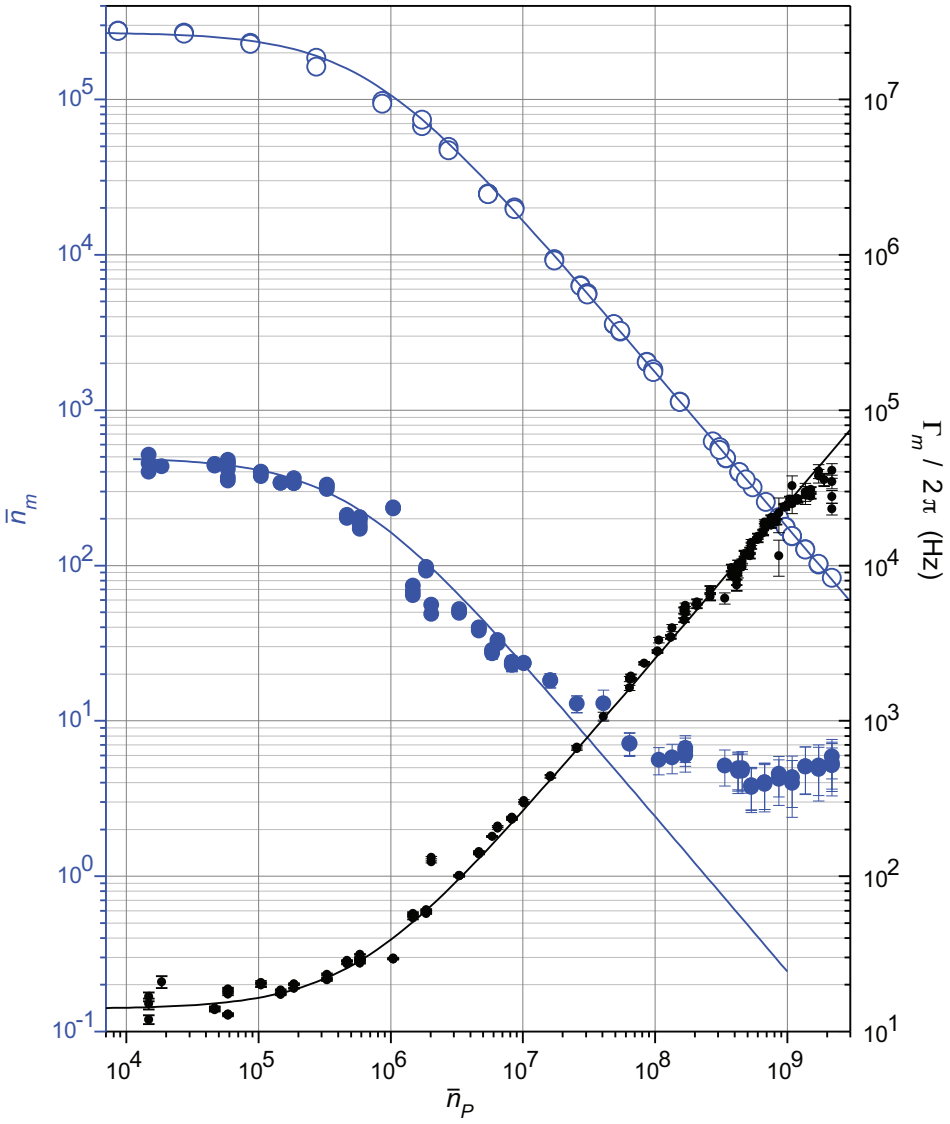

Figure 5.12: Back-action cooling of the NR from low and high effective NR temperature initial states compared. The cooling from $T = 150mK$ is shown in solid blue, while the cooling from a noise driven effective temperature of $T \approx 70K$ is show in open blue circles. Linewidth broadening of the low temperature data is shown for reference.

due to a significant increase in Γ_m^T. Based upon this alone, it is believed that the thermal calibration is valid and linear with pump power.

5.5 Pump detuning measurements

To better understand the back-action effects and also check our calculation of parameter of the device such as coupling constants, we also did pump detuning measurements in which we sweep the red microwave pump around the exact red detuning frequency. As discussed in , the back action NR linewidth broadening and frequency pulling depend on the exact detuning of the pump from the cavity frequency. Figure 5.13 shows detuning sweeps.

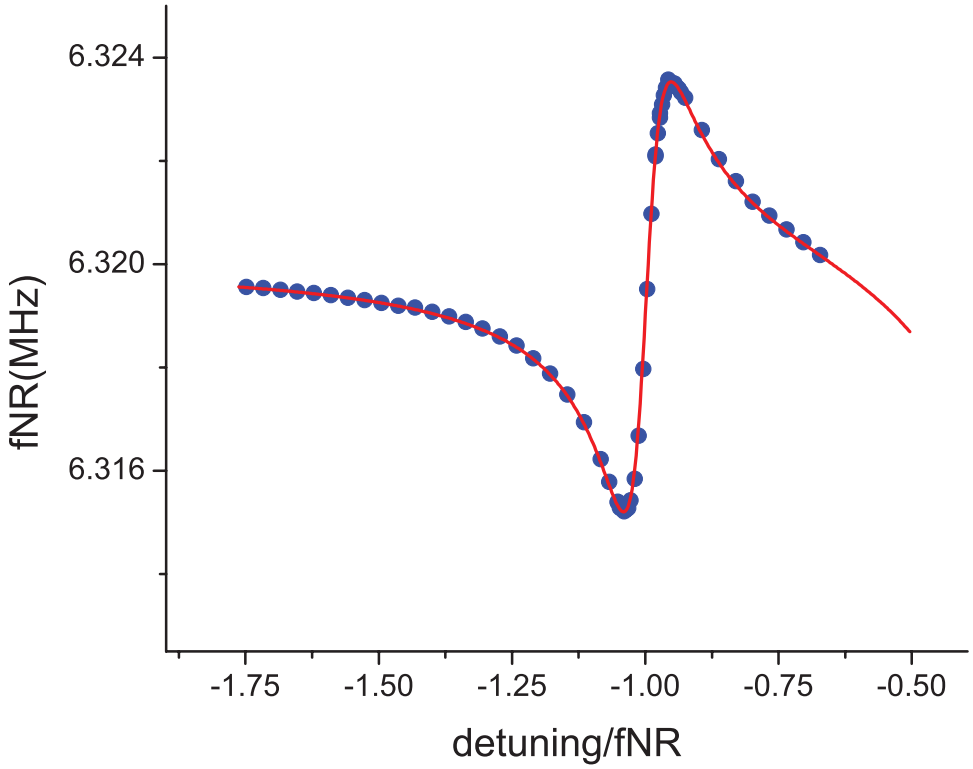

Figure 5.13: Detuned red-pump NR frequency pulling. The red pump frequency is swept from exactly f_{NR} below f_{SR} and the NR frequency response is measured. The red curve shows a fit to the date taking into account both the theoretical frequency pulling effect from the expected interaction with the microwave field as well as a non-linear optomechanical spring constant pulling.

From [38] one can obtain the optomechanical frequency pulling due to the interaction of the NR with the microwave fields. In addition, to accurately model

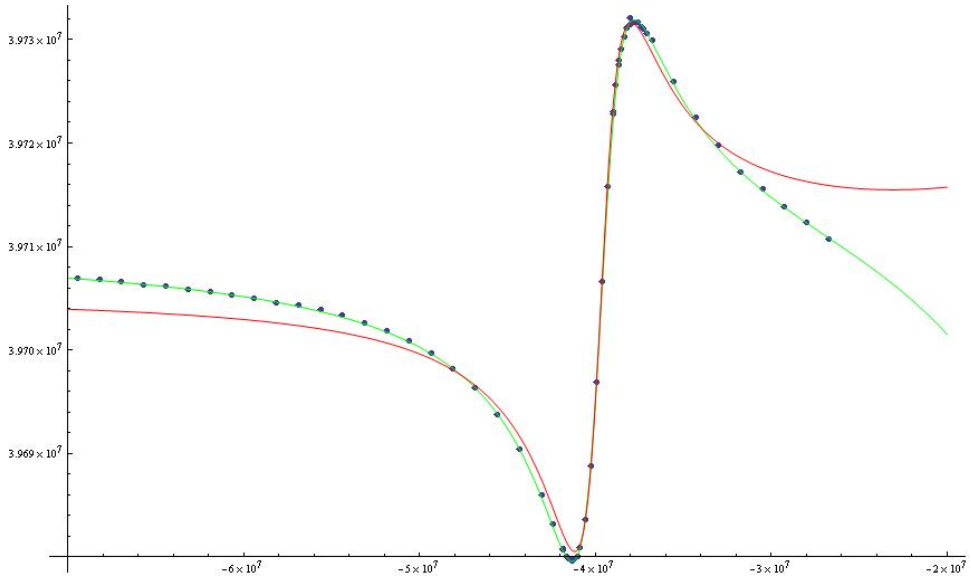

Figure 5.14: An example fit of detuning sweep data both with and without a non-linear pulling term. The green curve shows the fit to detuning date(blue dots) including a non-linear term while the red curve is the best fit without such a term.

the observed data, it was found that the frequency pulling must include a term directly proportional to applied power, which had not originally been considered. This can be attributed to an electrostatic type frequency pulling proportional to the average square of the voltage of the microwave field in the cavity. The entire frequency shift due to applied power is then given by:

$$\Delta\omega_{tot}^{NR} = \left(-\lambda x_{zp}^2 + \frac{2(g^2 x_{zp}^2 \delta \left[\left(\frac{\kappa}{2}\right)^2 + \delta^2 - \omega_m^2 \right]}{\left[\left(\frac{\kappa}{2}\right)^2 + (\omega_m + \delta)^2 \right] \left[\left(\frac{\kappa}{2}\right)^2 + (\omega_m - \delta)^2 \right]} \right) \bar{n}_p \tag{5.1}$$

Where g is coupling constant, $x_{zp} = \sqrt{\hbar/2m\omega_m}$ is zero point motion, $\delta = \omega_p - \omega_m$ is pump detuning, and $\lambda = \frac{1}{2}\frac{\omega_{SR}}{C_{tot}}\frac{\partial^2 C_g}{\partial x^2}$ is the second order frequency pulling term.

With the frequency pulling term, the fits to this data were extremely good at all powers measured. By comparison, attempts to fit the data without a non-

linear term gave extremely poor results; see for example a comparison of fits in figure 5.14. This suggests that the understanding of the physics involved is accurately modeled. From the fit of this data, the coupling term, g, can be additionally extracted and was found to be within the error of the value found from the thermal calibration, $g = 86 KHz/nm$.

CHAPTER 6

DISCUSSION AND CONCLUSIONS

6.1 Discussion

Based on this data, it seems that the behavior of the NR-SR system is understood and that a clear claim to having reached an NR occupation of 3.8 quanta can be made. While this is a higher occupation than expected and desired, it does approach the ground state and begins to allow the possibility to see quantum effects. Based on thermal statistics, this average occupation gives a 21% probability of being in the ground state at any given time which puts direct quantum experiments within reaching distance. Fo an NR linewidth of 10Hz, one can make an estimate of the average time necessary for a single phonon to excite the NR due to it's coupling to the thermal bath. This gives a time of $\tau = (\dot{n}_T)^{-1} = 2\mu$s, which is longer or comparable to many q-bit measurement and relaxation times [36, 30].

It should be stressed that this calculation is done assuming the NR occupation value is an average occupation of what is essentially a thermal state. The occupation of the resonator is expected to follow Bose statistics and fluctuate randomly due to thermal forces. While the back-action cooling lowers the occupation from a completely equilibrium state, it should behave as only an increased damping term to a low temperature bath, cooling but not otherwise affecting the NR. This assumption is implicit in the process of fitting the NR sideband Lorentzian and using the thermal calibration to calculate occupation. It's also worth noting that the goodness of the fits of the NR sideband noise to a Lorentzian response is itself a good indication that the NR is behaving as a

randomly driven thermal state.

The experiments presented are similar to that of Teufel et al[61] which demonstrated cooling from $\bar{n}_m$ = 700 to 200. To better illustrate differences and improvements in the presented work, a a brief comparison of the experiments and devices can be made. The largest fundamental difference is that the microwave resonator here is designed with double end-coupling capacitors allowing direct measurement in transmission mode, rather than the interferometer-type measurements of Teufel et al. This design provides several favorable features, in particular the reduction of red-detuned drive power transmitted to the amplifier, reducing the complication of amplifier saturation. In addition, the microwave resonators here are constructed of niobium rather than aluminum for higher power handling.

The significantly improved cooling demonstrated here is primarily produced through greatly increased NR-SR coupling and power handling. For a numerical comparison, the experiment of Teufel et al demonstrated a coupling of $6.4 KHz/nm$, NR frequency of $1.525 MHz$, and a maximum demonstrated circulating power of $7.3 uW$. By comparison, we have demonstrated a coupling of $\sim 80 KHz/nm$, NR frequency of $6.2 MHz$, and a maximum photon count of $2 \cdot 10^9$ photons, equivalent to $468 uW$ circulating power.

6.2 current limitations

While it may be possible to directly use cooled devices with these occupation factors for quantum experiments, it would be ideal if current limitations could be overcome. The measurements identify several effects that work to prevent

true ground-state cooling: excess occupation of the SR ($\bar{n}_{sr}$) at high pump powers, heating of the NR thermal bath at high pump powers, and the non-thermal force noise at low temperatures preventing thermalization of the NR below 150mK. If these effects can be minimized or compensated for, the true ground state would be achievable at an order of magnitude less pump power than used in these experiments.

As discussed in section 3.4, it is believed that the excess SR occupation, $\bar{n}_{sr}$, is not a result of phase or amplitude noise. The double cavity filter system used achieved sufficient filtering that worst-case estimates of phase noise from the source should still be less than johnson noise from the 77K cavities themselves, and contribute less than 0.04 photons into the SR at the highest pump power. Clearly something causes additional heating.

Several possibilities were investigated in an attempt to reduce this effect. One possibility is that the fridge internals are heating due to the high pump power, possibly at the attenuators. A rough calculation based upon the power incident at the attenuators would suggest heating of several hundred millikelvin and observations of the fridge temperature while at base temperature showed slight heating when driving at maximum power. An attempt to overcome this possibility used large lengths of lossy coax as a replacement for the cold attenuators in order to greatly increase the volume of heated material and increase thermalization rates. Unfortunately, this did not significantly change the SR occupation.

A rough estimate of the heating produced from straight dissipation on the silicon sample can also be done to get an idea of how large an effect dissipation heating may be. Taking an estimate of the thermal conductivity of the silicon

from [53, 47] and assuming half the incident power is absorbed at the surface of the sample gives $\sim 150mK$ heat rise for the highest powers. Realistically, thermal conductivity is probably more limited by thermal transfer from the chip to the box, which is difficult to estimate. The prediction that heating could result in a doubling of the sample temperature is suggestive that this is a contributing effect, however.

It should be emphasized that the powers necessary to reach the lowest occupation factors correspond to a large fraction of a watt of microwave power put into the top of the fridge. It is not surprising that with such high powers, some aspect of the system might heat or behave non-idealy. It is expected that using similar capacitively coupled systems, possibly with different forms of mechanical resonators or the use of discrete components for the microwave resonator, would yield great improvement in the possible coupling, allowing cooling at much more sane drive powers. For example, by increasing Γ_{opt} a factor of 10, maintaining the same $\dot{n}_T$, one would expect $\bar{n}_m \approx 0.5$, with $P_0 = .67$, a significantly better proposition for use in quantum experiments.

6.3 Future Work

While preforming a quantum experiment with the NR that requires an initial zero occupation state might be challenging, there are additional techniques proposed to indirectly observe mechanical quantum behavior which are expected work even at low average occupation comparable to that presented here, such as [1, 65]. An additional experiment that the Schwab group has spent some time pursuing is that of looking for differences in up and down conversion rates

of photons scattered by the NR. Analogous to Raman scattering, up-converted photon rates are expected to be proportional to $\bar{n}_{NR}$ while down-converted photons are expected to be proportional to $\bar{n}_{NR} = 1$. A discussion and calculation of measurement times for such an experiment is included in appendix B. Using a second blue-detuned continuous weak probe signal, this dependance was looked for, but experiments had to be concluded before the effect was clearly seen. This would be a possible avenue to pursue with further experiments, especially if higher SR-NR coupling could be achieved, and would be one of the first clear signatures of the quantum nature of a mechanical resonance.

Beyond such proposals to observe quantum effects with devices such as demonstrated here, it is clear that there are many improvements that could be made in performance. While the device here is closely approaching the ground state, increases in coupling and, in particular, decreases in the needed pump power to achieve cooling would make available the deep quantum ground state. It would seem that this is the clear way forward for using this type of mechanical device in quantum-limited experiments.

APPENDIX A

FABRICATION

The devices used in this dissertation were all of the form of a e-beam litheographic nanoresonator coupled to an optical litheographic superconducting microwave resonator. Three separate fabrication recipes for these devices were developed, one for each metal composition used: all Al, Nb SR and Al NR, and all Nb. This appendix has a brief description of the techniques and concerns in the fab processes as well as a listing of the recipes used. With only occasional exception, the work done for the devices in this thesis was done at the Cornell Nanofabrication Facility.

A.1 overview

Our device fabrication process begins with ultra-high resistivity Si wafers: $\langle 100 \rangle$ orientation, 500 micrometers thick. The wafer is coated with around 70-80nm of silicon nitride (high stress, low pressure chemical vapor deposited as described in [66]) which will form the nanoresonator substrate material. As we have found this material to have high microwave dissipation, the SiN is etched away from all but small $2\mu m$ x $37\mu m$ islands where the nanoresonators will be fabricated. This is accomplished using photolithographic patterning and a combination of CHF_3/O_2 plasma etching and a 6:1 buffered oxide wet etch.

The resulting SiN islands are then coated with 80nm of aluminum, using photolithography and lift-off. The Al serve a dual purpose as a stop-etch barrier and as pads for electrical contact with the subsequent niobium deposition. 350nm of niobium is deposited over the entire wafer in a low pressure($2 \cdot 10^{-7}$

torr) sputter system. The niobium is then etched to form the coplanar wave guide and resonator using a CF_4/O_2 plasma with a photoresist etch mask. This process etches slightly into the silicon over most of the device but is stopped by the aluminum stop-etch at the SiN islands.

Following the niobium etch, the aluminum is patterned to leave small electrical contact pads, using photolithography followed by wet etching with an aluminum stripping solution. The nanoresonators are then formed in a two step e-beam process. First, using a bilayer PMMA mask, e-beam lithography, aluminum evaporation, followed by liftoff, the nanoresonator, gate, and electrical contacts to the niobium are defined. A second e-beam process then defines an etch window in a PMMA mask located around the nanoresonator. The mechanical resonator is freed via a two-step etch process. The first etch, CHF_3/O_2, vertically removes the SiN layer, and the the second, an SF_6 etch, isotropically under-etches and frees the beam. The finished chips are cleaned in O_2 plasma before mounting in sample boxes.

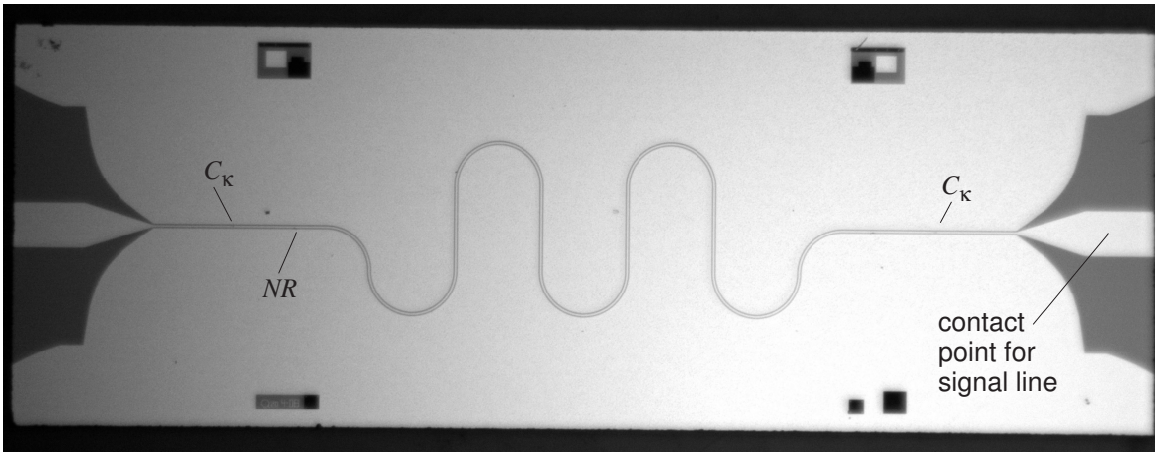

Figure A.1: Optical image of completed nanofabricated sample.

A.1.1 Fabrication of Al-SR

Start with bare, clean, high-resistivity silicon wafer.

- Spin LOR5A at 5500rpm for 60sec, bake at 180C for 3mins
- Spin S1813 at 5500rpm for 60sec, bake at 115C for 60sec
- Expose SR-photomask pattern using 5x-g-line stepper at 0.5sec per die.
- Develop exposed bilayer resist in MIF 300 for 60s.
- Thermal evaporate 300nm of Al at 4-5 /s at a pressure of $1x10^{-7}$torr.
- Lift off (usually for more than 4hrs) in resist remover, 1165

A.1.2 Fabrication of Nb-SR

- Spin SPR 220 3.0 at 5500rpm for 60sec, bake at 115oC for 90sec
- Expose SR-photomask pattern using the 5x-g-line stepper at 1.6sec per die.
- Post exposure bake the SPR at 115oC for 90sec.
- Reverse the tone of the exposed SPR by baking it in 600Torr of NH 3 in the YES 58-SM oven.
- Flood expose the SPR for 60sec using the EV620 contact aligner
- Develop the SPR in MIF 300 for 70sec or in MIF 321 for 100sec. After optical inspection to confirm that the pattern looks good, we proceed with etching the Nb.
- Etch the Nb metal using the Oxford PlasmaLab 80+ RIE System (50W, 40mTorr, 100 sccm of CF4/10 sccm of O2). CF4/O2 etches the Nb vertically with little or no undercut. This etch is non-uniform across the wafer

but on average etches the Nb at 20nm/min (SEMS). Doing 1-2mins O2 descum every 4-5mins of the etch softens the hardened resist + Nb complex that forms on the walls of the SPR etch mask.

- Strip the SPR resist in 1165 (add SEM of Nb-SR, capacitors, Nb grain, etch).

A.1.3 Fabrication of hs-SiNx Patches on Si Substrate

- Firstly we grow 70-100nm if hs-SiNx on a high resistivity 100-Si wafer using the low pressure chemical vapor deposition (LPCVD) furnace at the CNF (T = 775oC, P=224mTorr, 98% of NH3, 40% Dichlorosilane). Using standard photolithographic techniques we pattern a photoresist to cover the regions where the hs-SiNx patches will be formed.
- Spin SPR 220 3.0 at 5500rpm for 60sec, bake at 115oC for 90sec
- Expose the hs-SiNx-mask pattern using the 5x-g-line stepper at 1.6sec per die.
- Post exposure bake the SPR at 115oC for 90sec.
- Develop the exposed SPR in MIF 321 for 100sec or in MIF 300 for 70sec.
- After optical inspection, bake in 90oC oven for at least 6-8hours After about 8hours of bake to harden the SPR, we proceed to etch the nitride layer

Reactive Ion Etch (RIE)

Use filmetric to measure the thickness of hs-SiNx at start of etch

Etch the hs-SiNx using the Oxford PlasmaLab 80+ RIE system (150W, 55mTorr, 50sccm CHF3/5 sccm O2) until only about 10-20nm thick of nitride is left. Measure the nitride film thickness periodically during the etch.

Buffered Oxide Etch (BOE)

Use BOE (6:1) to etch the remaining 10-20nm of nitride in about 10-15mins. BOE (6:1) etches hs-SiNx very slowly at 0.5-1nm/min.

Rinse in DI water. A quick test to determine if all the nitride has been etched is to check if DI water wets the surface or not. Water does not wet a Si surface because Si is hydrophobic. Water wets hs-SiNx as it is hydrophilic.

Optical inspect and use filmetric to determine that all the unwanted nitride has been etched away.

Strip the remaining SPR in 1165 at the end of the first BOE etch.

BOE (6:1) etch to trim the hs-SiNx patch to the desired thickness of 60-65nm

Rinse thoroughly in water and blow dry.

Ebeam #1

- Spin PMMA 495 A4 at 2000rpm (200nm) for 60sec, bake at 170oC for 15mins
- Spin PMMA 950 M2 at 2000rpm (150nm) for 60sec, bake at 170oC for 15mins
- Expose NR design pattern using the Leica VB6 or the JEOL 9300 at the CNF (100kV accelerating voltage, 1nA beam current, 1200-1400 C/cm2 dose)

- Develop exposed bi-layer resist in MIBK:IPA = 1:3 for 90sec
- Rinse in IPA for 30sec
- After optical inspection, do a low power 8-10sec O 2 descum using the Oxford PlasmaLab 80+ RIE system (50W, 60mTorr, 50sccm of O2)
- Evaporate 80-100nm of NR Al at 4-5/s at a pressure of 1e-7torr.
- Lift-off in methylene chloride : acetone 1:1 for ¿ 4hours
- Rinse in IPA
- Inspect the beams using SEM.
- Dice chips into 3.5mm x 10mm final sample form factor.

Ebeam #2

- Spin PMMA 495 A8 at 4000rpm (450nm) for 60sec, bake at 170oC for 15mins
- Expose the hs-SiNx window design pattern using the Leica VB6 or the JEOL 9300 at the CNF (100kV accelerating voltage,1nA beam current, 1400-1800 C/cm2 dose)
- Develop exposed resist in MIBK:IPA = 1:3 for 90sec
- Rinse in IPA for 30sec
- Optical inspect for alignment.

Freeing Al-beams

We mainly use the Oxford PlasmaLab 80+ RIE system to free the Al beams with the following procedure

- 2mins of vertical hs-SiNx etch (150W, 55mTorr, 50sccm CHF 3/5 sccm O2, etch rate 60nm/min)
- 35-60sec of isotropic Si etch (100W, 125mTorr, 60sccm SF 6, etch rate 500-700nm/min)
- 20-30mins of low power O 2 descum to strip the residual resist (50W, 60mTorr, 50sccm O2)
- SEM inspect the freed beams We usually break vacuum between the etch step above to optical inspect the beams.

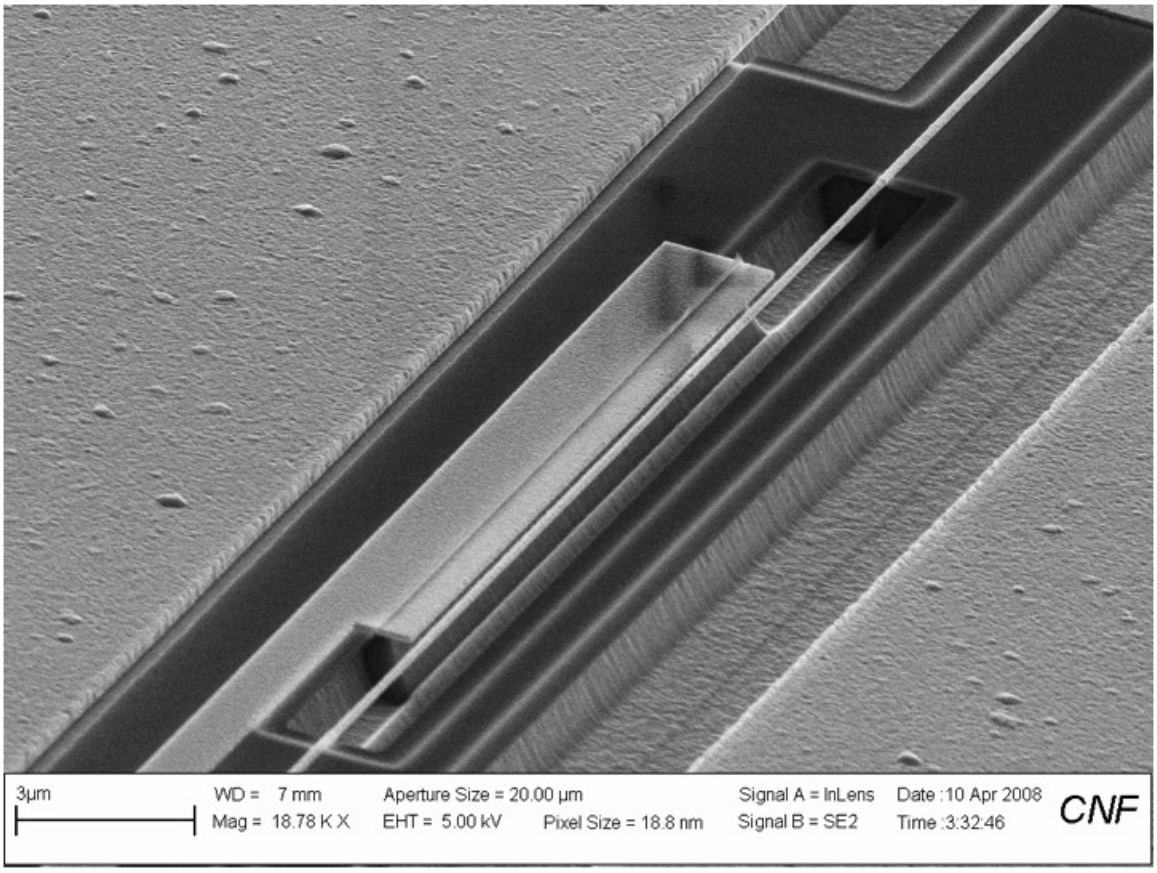

Figure A.2: SEM of the freed NR structure. The beam can be clearly seen freely suspended in close proximity to the gate on the left.

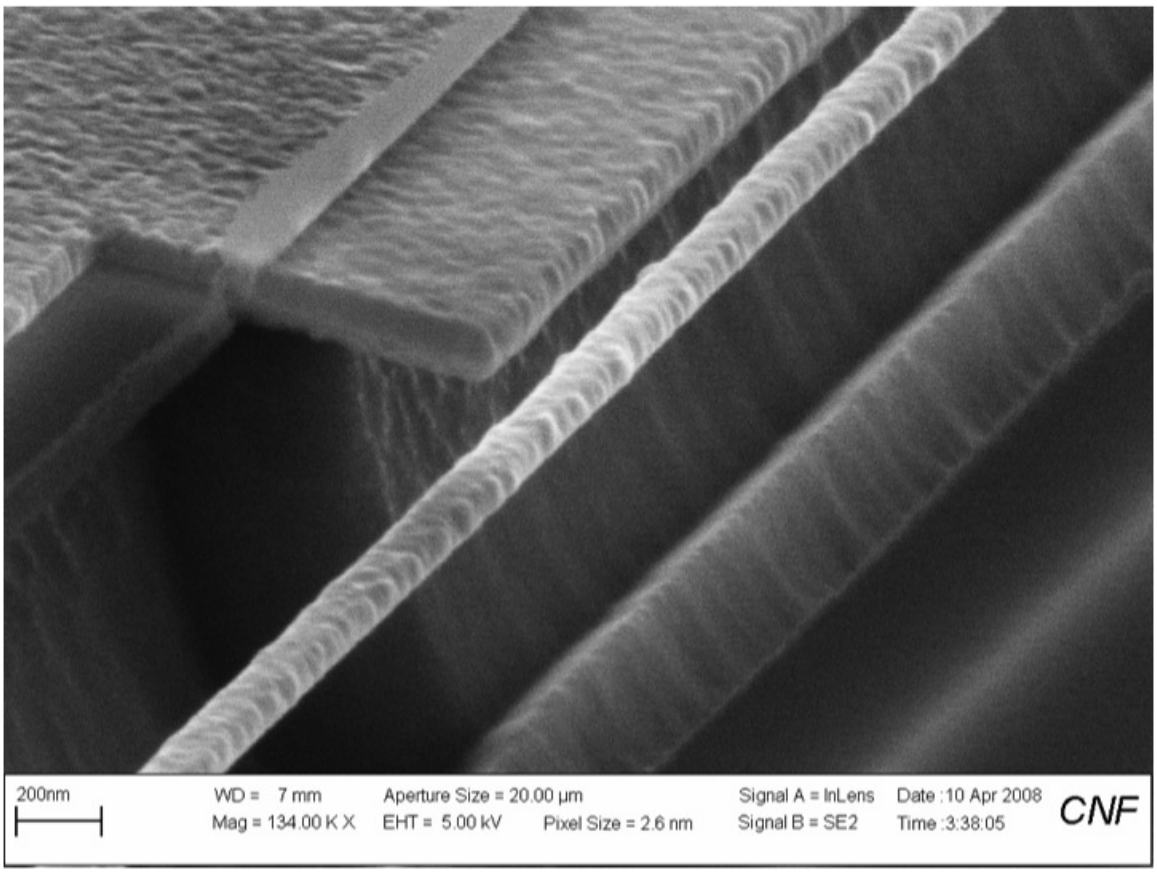

Figure A.3: SEM of the freed NR structure closeup.

APPENDIX B

CONSIDERATIONS ON MEASUREMENT OF SIMULTANEOUS UP AND DOWN CONVERSION RATES

The previous work has demonstrated average nanoresonator occupation of $\sim 3.8 \pm 1.2$ quanta. In order to more accurately measure mechanical resonator states near the ground state, as well as to demonstrate conclusively the quantum nature of a macroscopic object, we would like to make use of fundamental quantum behavior of the nanoresonator. The clearest way we currently see to do this is to utilize the difference in up conversion and down conversion rate of photons from two applied microwave probe in a similar setup as that discussed in this thesis. Analogous to Raman scattering[69], the down-convertion rate would be proportional to $\bar{n}_m + 1$, while the up-converted rate is proportional to $\bar{n}_m$ allowing for a direct observation of the difference and thus a clear quantum signature.

While this is simple in theory, practical considerations are, as always, somewhat more complicated. Two specific measurement schemes are discussed: a continous measurement done in equilibrium while cooling, and a pulse measurement scheme.

B.0.4 Continuous Measurement

Conceptually, a continuous measurement is simple. A strong red-detuned drive is used to widen NR linewidth and cool to near the ground state. Simultaneously, a weak blue-detuned probe is introduced and the sidebands are measured on the spectrum analyzer, which when combined with calibration directly gives

conversion rates. In this case both red and blue sidebands are generated at the microwave cavity resonance frequenecy. In order that both sidebands can be resolved, the drive frequencies must be shifted slightly in order to separate the sidebands generated at the microwave resonance frequency. This does change scattering rates in theory, but so long as the shift is much less than microwave linewidth, the effect is slight.

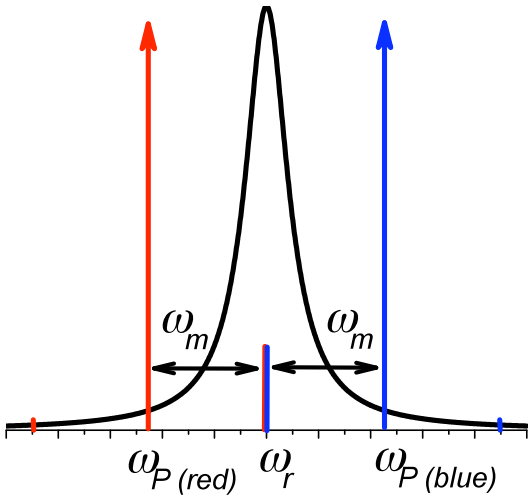

Figure B.1: Schematic representation of Red + blue probe measurement of the NR. Pumps are detuned by $\sim \omega_m$ from cavity frequency, with slight differences in detuning to allow both sidebands to be simultaneously resolved

With any combination of red and/or blue detuned drives, the red drive extracts energy from the NR, thus increasing NR linewidth while blue drive injects energy, thus narrowing linewidth. The steady state temperature of the mechanics is given by the detailed balance equation

$$\bar{n}_m = \frac{\Gamma_m^T \bar{n}_m^T + \Gamma_{opt} \bar{n}_{SR}}{\Gamma_m^T + \Gamma_{opt}} \tag{B.1}$$

where Γ_m^T is the natural linewidth of the mechanics, $\bar{n}_m^T$ is the temperature of the bath in NR quanta, Γ_{opt} is the coupling to the microwave field, and $\bar{n}_{SR}$ is the effective occupation of the microwave resonator, which in the sideband resolved limit($\omega_m > \kappa$) is approximately zero [37]. The total effective Γ_{opt} linewidth is equal to the sum of the contributions from red and blue drives:

$$\Gamma_{opt} \simeq \frac{4\Delta x_{zp}^2 g^2}{\kappa}\left(\bar{n}_p^R - \bar{n}_p^B\right) \tag{B.2}$$

where $\Delta x_{zp} = \sqrt{hbar/2m\omega_m}$ is the magnitude of zero point fluctuations of the NR, $g = \partial\omega_{SR}/\partial x$ is the relative change in microwave resonance frequency for mechanical motion, and κ is microwave resonance linewidth. As such, NR mode temperature can be adjusted by changing Pred, Pblue, or both, so long as the difference in powers is set to give the desired linewidth and temperature. If the maximum power handling of the sample is the limiting factor, this means that signal can be arbitratily increased by increasing Pred and Pblue simultaniously. Of course, power handling is always limited at some point.

At high NR occupation, the effective calibrated signal of red and blue should be roughtly equivalent. As occupation is lowered, the difference in scattering rates should become evident. Even if the relative calibrations of the two are only known poorly, taking the ratio of the red to blue scattering rate should demonstrate deviation and should allow an accurate measure of the thermal occupation of the mechanics, independent on external calibrations.

The practical hurdles of this measurement technique are two-fold. The first is that of obtaining sufficient signal to noise level at reasonable power levels. To estimate this, we can use demonstrated device parameters in [52], [29] and

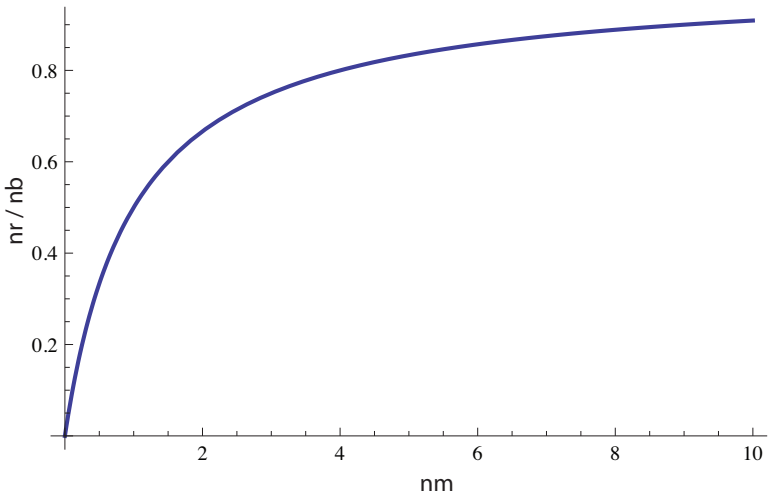

Figure B.2: Expected ratio of measured red vs. blue scattering rates.

extrapolate to newer optimized devices.

The current best device, when driven with a strong red cooling pump, gave a signal sufficient to measure a mechanics occupation of $\bar{n}_m \approx 1 quanta$ with sufficient signal to reduce error to $\sim 10\%$ after 2 hours of continuous averaging. This was obtained at a cavity occupation of $\bar{n}_p \approx 5 \times 10^8 photons$. To simultaneously measure the down-conversion scattering rate, we would need to add an additional weak blue probe of about 1/10th the power of the red pump. The blue measurement would require 100 times the averaging time to compensate for the reduced signal. Based upon averaging times for the red measurement, this would then require over a week of acquisition per data point.

This is not entirely infeasable, but we can certainly improve matters. In theory, the microwave resonator should have extremely low losses corresponding to internal loss limited $Q > 80,000$. As such, our design of $Q = 20,000$ should be over-coupled, and thus any photons generated in the cavity, ie by scattering with the NR, should predominately leak out the coupling capacitors. In the

sample considered here, however, there was additional anomalous dissipation in the cavity. This dissipation caused the absorption of approximately 70% of the photons. With newly fabricated samples, we see none of this additional dissipation and so expect much higher signal output.

A second improvement we have worked on is to adjust the end coupling capacitors. In old designs, the end capacitors were equal in value, causing a loss of half the converted photons out the drive end of the cavity. By increasing the output capacitor while decreasing the input capacitor, we can preferentially send photons out the side connected to the HEMT amplifier, thus increasing signal. Current designs allow $\sim 3/4$ of the photons out the output end of the cavity.

Combining these improvements in a new device, even without addition improvements in coupling or maximum power handling, should achieve acceptable signal to noise after only 8 hours of averaging. This is still somewhat longer than would be ideal, but is acceptable.

The second practical issue is that of relative linewidths. With a designed sample of $Q_{SR} = 30,000$, $f_{SR} = 7.5GHz$, we have $\Gamma_{SR} = 2\pi \cdot 250KHz$. At the point of best cooling with the current sample, mechnical linewidth is broadened to up to $\Gamma_m \approx 30KHz$. To avoid overlap issues with the red and blue sidebands, they should ideally be separated by several NR linewidths. Clearly this becomes difficult. Even separating by 60KHz, the roll-off of the cavity Lorentzian begins to be non-negligible. This, strictly speaking, is not a problem. The difference in scattering rate for a slightly detuned signal is known and can be compensating for by

$$\Gamma_{opt} \simeq \frac{\left(\frac{\kappa}{2}\right)^2}{\left(\frac{\kappa}{2}\right)^2 + (\Delta - \omega_m)^2} \frac{4\Delta x_{zp}^2 g^2 \bar{n}_p}{\kappa} \tag{B.3}$$

The sideband peak Lorentzians will also be distorted by the cavity Lorentzian shape, but this can be corrected for and a carefully written curve fitter should be able to simultaneously fit both peaks.

B.0.5 Pulsed Measurement

In a pulsed measurement scheme, the NR is first prepared in a low occupation state, then cooling power is turned off and a quick up-conversion rate measurement is preformed.

This is done in a series of steps as shown in fig. B.3:

1) Cool NR to desired temperature. $\tau \approx 8\mu s$

2) Turn off red pump, turn on blue probe

3) Wait until circulating power rings down/up from red to blue. $\tau \approx 0.6\mu s$

4) Measure output signal for short enough time that the mechanics heats by < 1 quanta

Repeat...

The measurement time involved here has three relevant time scales. First, the coupling of the mechanics to the thermal bath produces natural leakage of quanta into the mechanics. We can estimate this given by the natural linewidth

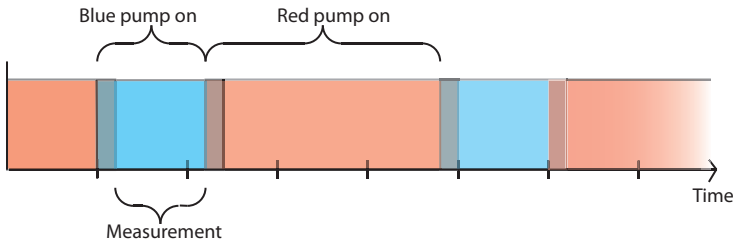

Figure B.3: Pulse measurement scheme

of the mechanics, which is typically 20Hz or less. Given a fridge temperature of 150mK and a 6MHz beam, this gives

$$T_{bath} \approx 500 quanta$$

$$\tau_{themal} \approx 6.3 \times 10^4 quanta/s$$

Or, more usefully, one quanta in $\approx 16\mu s$. Any pulse measurement should be done in less then this amount of time.

Second, the blue probe measurement has some direct back-action heating effect on the NR. Since we are making a down conversion measurement, each photon extracted corresponds to one phonon of NR heating. As such, the blue probe measurement should be of sufficient power and length to produce at most one photon. We can estimate this conversion rate based upon coupling strengths in the current sample. Given a max Γ_{opt} of 20KHz(obtained in [52]), we assume that we can obtain an equivalent strength coupling with a blue drive. At this coupling:

$$rate = 2\pi\Gamma_{opt} n_m$$
$$\approx 125000 n_m / s$$

or one quanta in $8\mu s$ for the mechanics in its ground state. This is half the maximum time available based upon bath leakage.

Given that is seems possible to generate one photon per cycle, the actual signal to noise needs to be calculated. This is most easily done by comparing the number of photons reaching the HEMT amplifier with the background level of noise in quanta, which is here dominated by the HEMT. For a careful design of the microwave cavity, we can make the coupling capacitor on the output larger than the input, allowing effective capture of $\sim 3/4$ of the photons. Our current setup has an estimated $\sim 1.5dB$ line loss between the sample and the HEMT, and a HEMT temperature of 4K at 7.5GHz. This gives:

$$Signal = 0.5 photon/pulse$$
$$Noise = 11 quanta \cdot BW$$

Where BW is measurement bandwidth. We would typically do this measurement using a digitizing spectrum analyzer with FFT, but regardless of measurement technique, the effective bandwidth is limited by measurement time. In this case, given a measurement time of $10\mu s$, our bandwidth resolution is 200KHz. For this measurement time and bandwidth, this gives $S/N = 0.012$ for each measurement. In order to obtain a reasonable signal to noise ratio of 4, this

then requires $\sim 100,000$ averages. At a very generous time of 10ms per pulse, this gives a total data collection time of around 100s.

Based upon these number, either a continuous or pulsed measurement scheme seems like it would work. The pulsed scheme gives a higher effective signal to noise and thus faster acquisition times, attributable to its higher power signal during measurement times. This comes at the cost of greater complexity, however, so it may be that a simple continuous measurement would be the best first avenue to pursue.

BIBLIOGRAPHY

[1] A.D. Armour, M.P. Blencowe, and K.C. Schwab. Entanglement and decoherence of a micromechanical resonator via coupling to a cooper-pair box. *Phys. Rev. Lett.*, 88:148301, 2002.

[2] F Biquard and A. Septier. Improvement of the surface conductivity of copper and aluminium at hyper-frequencies by lowering the temperature. *Nuclear Instr. and Methods*, 44(1):18–28, 1966.

[3] K. Bladh, D. Gunnarsson, E. Hurfeld, S. Devi, C. Kristoffersson, B. Smalander, S. Pehrson, T. Claeson, P. Delsing, and M. Taslakov. Comparison of cryogenic lters for use in single electronics experiments. *REVIEW OF SCIENTIFIC INSTRUMENTS*, 74(3), 2003.

[4] D. G. Blair, E. N. Ivanov, M. E. Tobar, P. J. Turner, F. van Kann, and I. S. Heng. High sensitivity gravitational wave antenna with parametric transducer readout. *Phys. Rev. Lett.*, 74(11):1908–1911, Mar 1995.

[5] M. F. Bocko and R. Onofrio. On the measurement of a weak classical force coupled to a harmonic oscillator: experimental progress. *Rev. Modern Phys.*, 68(3):755–799, July 1996.

[6] M.F. Bocko and W.W. Johnson. Phase-sensitive parametric motion transducer. *Phys. Rev. A*, 30:2135–2137, 1984.

[7] V. B. Braginsky, Y. I. Vorontsov, and K. S. Thorne. Quantum nondemolition measurements. *Science*, 209:547–557, 1980.

[8] V.B. Braginsky and Yu.I. Vorontsov. Quantum-mechanical limitations in macroscopic experiments and modern experimental design. *Sov. Phys. Usp.*, 17:644–650, 1975.

[9] Vladimir B. Braginsky and Farid YA. Khalili. *Quantum Measurement*. Cambridge University Press, Cambridge, UK, 1992.

[10] C. M. Caves. Quantum limits on noise in linear amplifiers. *Phys. Rev. D*, 26(8):1817–1839, October 1982.

[11] Carlton M. Caves, Kip S. Thorne, Ronald W. P. Drever, Vernon D. Sandberg, and Mark Zimmermann. On the measurement of a weak classical force

coupled to a quantum-mechanical oscillator. I. issues of principle. *Rev. Mod. Phys.*, 52(2):341–392, Apr 1980.

[12] A. N. Cleland and M. L. Roukes. A nanometre-scale mechanical electrometer. *Nature*, 392:160–162, March 1998.

[13] A A Clerk, F Marquardt, and K Jacobs. Back-action evasion and squeezing of a mechanical resonator using a cavity detector. *New Journal of Physics*, 10(9):095010 (20pp), 2008.

[14] Peter K. Day, Henry G. LeDuc, Benjamin A. Mazin, Anastasios Vayonakis, and Jonas Zmuidzinas. A broadband superconducting detector suitable for use in large arrays. *Nature*, 425:817–821, October 2003.

[15] L.E. DeLong, O. G. Symko, and J. C. Wheatley. Continuously operating he4 evaporation refigerator. *The review of scientific instruments*, 42(1):147–150, January 1971.

[16] F. Diedrich, J. C. Bergquist, Wayne M. Itano, and D. J. Wineland. Laser cooling to the zero-point energy of motion. *Phys. Rev. Lett.*, 62(4):403–406, Jan 1989.

[17] J. M. Dorbrindt, I. Wilson-Rae, and T. J. Kippenberg. Parametric normal-mode splitting in cavity optomechanics. *Phys. Rev. Lett.*, 101:263602, 2008.

[18] Theodore Van Duzer and Charles W. Turner. *Principles of Superconductive Devices and Circuits*. Prentice Hall, 2nd edition, 1998.

[19] M. I. Dykman. Heating and cooling of local and quasilocal vibrations by nonresonant field. *Sov. Phys. Solid State*, 20:1306–11, 1978.

[20] L. Frunzio, A. Wallraff, D. Schuster, J. Majer, , and R. Schoelkopf. Fabrication and characterization of superconducting circuit qed devices for quantum computation. *IEEE Trans. Appl. Supercon.*, 15(2):860–863, June 2005.

[21] Jiansong Gao, M. Daal, J.M. Martinis, A. Vayonakis, J. Zmuidzinas, B. Sadoulet, B.A. Mazin, P.K. Day, and H.G. Leduc. A semiempirical model for two-level system noise in superconducting microresonators. *Applied Physics Letters*, 92(21):212504 – 1, 2008/05/26.

[22] C. Genes, D. Vitali, P. Tombesi, S. Gigan, and M. Aspelmeyer. Ground-

state cooling of a micromechanical oscillator: Comparing cold damping and cavity-assisted cooling schemes. *Phys. Rev. A*, 77:033804, 2008.

[23] S. Gigan, H. R. Boehm, M. Paternostro, F. Blaser, G. Langer, J. B. Hertzberg, K. C. Schwab, D. Baeuerle, M. Aspelmeyer, and A. Zeilinger. Self-cooling of a micromirror by radiation pressure. *Nature*, 444(7115):67–70, Nov 2006.

[24] Simon Groblacher, Klemens Hammerer, Michael R. Vanner, and Markus Aspelmeyer. Observation of strong coupling between a micromechanical resonator and an optical cavity field. *Nature*, 460:724–727, 2009.

[25] Simon Gröblacher, Jared B. Hertzberg, Michael R. Vanner, Garrett D. Cole, Sylvain Gigan, K. C. Schwab, and Markus Aspelmeyer. Demonstration of an ultracold micro-optomechanical oscillator in a cryogenic cavity. *Nature Phys.*, 06/07/online:10.1038/nphys1301, 2009. (advanced online publication).

[26] G. Hammer, S. Wuensch, M. Roesch, K. Ilin, E. Crocoll, and M. Siegel. Superconducting coplanar waveguide resonators for detector applications. *Supercond. Sci. Technol.*, 20:S408, October 2007.

[27] Jared B. Hertzberg. *BACK-ACTION EVADING MEASUREMENTS OF NANOMECHANICAL MOTION APPROACHING QUANTUM LIMITS*. PhD thesis, University of Maryland at College Park, 2009.

[28] J.B. Hertzberg, T. Rocheleau, T. Ndukum, M. Savva, A. A. Clerk, and K.C. Schwab. Back-action-evading measurements of nanomechanical motion. *Nature Physics*, 6:213–217, 2010.

[29] J.B. Hertzberg, T. Rocheleau, T. Ndukum, M. Savva, A.A. Clerk, and K.C. Schwab. Back-action evading measurements of nanomechanical motion. *arXiv:0906.0967v1*, 2009. (unpublished).

[30] Max Hofheinz, E. M. Weig, M. Ansmann, Radoslaw C. Bialczak, Erik Lucero, M. Neeley, A. D. O'Connell, H. Wang, John M. Martinis, and A. N. Cleland. Generation of fock states in a superconducting quantum circuit. *Nature*, 454:310–314, 2008.

[31] Charles Kittel and Herbert Kroemer. *Thermal Physics*. W. H. Freeman, 2nd edition.

[32] D. Kleckner and D. Bouwmeester. Sub-kelvin optical cooling of a micromechanical resonator. *Nature*, 444:75–78, 2006.

[33] Robert G. Knobel and Andrew N. Cleland. Nanometre-scale displacement sensing using a single electron transistor. *Nature*, 424:291–293, July 2003.

[34] M. D. LaHaye, O. Buu, B. Camarota, and K. C. Schwab. Approaching the quantum limit of a nanomechanical resonator. *Science*, 304:74–77, April 2004.

[35] N. P. Linthorne, P. J. Veitch, and D. G. Blair. Interaction of a parametric transducer with a resonant bar gravitational radiation detector. *J. Phys. D: Appl. Phys.*, 23:1–6, 1990.

[36] V. E. Manucharyan, J. Koch, L. Glazman, and M. H. Devoret. Fluxonium: Single cooper-pair circuit free of charge offsets. *Science*, 326:113–116, 2009.

[37] F. Marquardt, J. P. Chen, A. A. Clerk, and S. M. Girvin. Quantum theory of cavity-assisted sideband cooling of mechanical motion. *Phys. Rev. Lett.*, 99:093902, August 2007.

[38] F. Marquardt, J. P. Chen, A. A. Clerk, and S. M. Girvin. Quantum theory of cavity-assisted sideband cooling of mechanical motion. *Phys. Rev. Lett.*, 99:093902, August 2007.

[39] Florian Marquardt, A.A. Clerk, and S.M. Girvin. Quantum theory of optomechanical cooling. *J. Mod. Optics*, 55(19-20):3329–3338, November 2008.

[40] Florian Marquardt and Steve M. Girvin. Optomechanics. *Physics*, 2:40, May 2009.

[41] William Marshall, Christoph Simon, Roger Penrose, and Dik Bouwmeester. Towards quantum superpositions of a mirror. *Phys. Rev. Lett.*, 91(13):130401, Sep 2003.

[42] William Marshall, Christoph Simon, Roger Penrose, and Dik Bouwmeester. Towards quantum superpositions of a mirror. *Phys. Rev. Lett*, 91:130401, 2003.

[43] A. Naik, O. Buu, M. D. LaHaye, A. D. Armour, A. A. Clerk, M. P. Blencowe, and K. C. Schwab. Cooling a nanomechanical resonator with quantum back-action. *Nature*, 443:193–196, September 2006.

[44] A.D. OConnell, M. Ansmann, R.C. Bialczak, M. Hofheinz, N. Katz, E. Lucero, C. McKenney, M. Neeley, H. Wang, E.M. Weig, A.N. Cleland, and J.M. Martinis. Microwave dielectric loss at single photon energies and millikelvin temperatures. *Applied Physics Letters*, 92(11):112903 – 1, 2008.

[45] A. D. OConnell, M. Hofheinz, M. Ansmann, Radoslaw C. Bialczak, M. Lenander, Erik Lucero, M. Neeley, D. Sank, H. Wang, M. Weides, J. Wenner, John M. Martinis, and A. N. Cleland. Quantum ground state and single-phonon control of a mechanical resonator. *Nature*, 464:697–703, 2010.

[46] Young-Shin Park and Hailin Wang. Resolved-sideband and cryogenic cooling of an optomechanical resonator. *Nature Phys.*, 06/07/online:10.1038/nphys1303, 2009. (advanced online publication).

[47] F. Pobell. *Matter and Mehods at Low Temperatures*. Springer, 3rd edition, 2007.

[48] M. Poggio, C. L. Degen, H. J. Mamin, and D. Rugar. Feedback cooling of a cantilever's fundamental mode below 5 mK. *Physical Review Letters*, 99(1):017201, 2007.

[49] David M. Pozar. *Microwave Engineering*. John Wiley and Sons, third edition, 2005.

[50] C. A. Regal, J. D. Teufel, and K. W. Lehnert. Measuring nanomechanical motion with a microwave cavity interferometer. *Nature Physics*, 4:555–560, May 2008.

[51] R. C. Richardson and E. N. Smith. *Experimental Techniques in Condensed Matter Physics at Low Temperatures*. Westview Press, 1998.

[52] T. Rocheleau, T. Ndumum, C. Macklin, J.B. Hertzberg, A. A. Clerk, and K. C. Schwab. Preparation and detection of a mechanical resonator near the ground state of motion. *NATURE*, 463:72–75, january 2010.

[53] H M Rosenberg. The thermal conductivity of germanium and silicon at low temperatures. *Proceedings of the Physical Society. Section A*, 67(9), 1954.

[54] A. Schliesser, O. Arcizet, R. Riviere, G. Anetsberger, and T. J. Kippenberg. Resolved-sideband cooling and position measurement of a micromechanical oscillator close to the Heisenberg uncertainty limit. *Nature Phys.*, 06/07/online:10.1038/nphys1304, 2009. (advanced online publication).

[55] A. Schliesser, P. Del'Haye, N. Nooshi, K. J. Vahala, and T. J. Kippenberg. Radiation pressure cooling of a micromechanical oscillator using dynamical backaction. *Phys. Rev. Lett.*, 97(24), Dec 15 2006.

[56] A. Schliesser, R. Riviere, G. Anetsberger, O. Arcizet, and T. J. Kippenberg. Resolved-sideband cooling of a micromechanical oscillator. *Nature Physics*, 4(5):415–419, May 2008.

[57] David I. Schuster. *Circuit Quantum Electrodynamics*. PhD thesis, Yale University, 2007.

[58] Keith C. Schwab and Michael L. Roukes. Putting mechanics into quantum mechanics. *Physics Today*, 58(7):36–42, 2005.

[59] Rainee N. Simons. *Coplanar Waveguide Circuits, Components, and Systems*. John Wiley and Sons, New York, 2001.

[60] J. D. Teufel, J. W. Harlow, C. A. Regal, and K. W. Lehnert. Dynamical backaction of microwave fields on a nanomechanical oscillator. *Phys. Rev. Lett.*, 101(19):197203, 2008.

[61] J. D. Teufel, C. A. Regal, and K. W. Lehnert. Prospects for cooling nanomechanical motion by coupling to a superconducting microwave resonator. *New J. Phys.*, 10:095002, September 2008.

[62] M.E. TOBAR and D.G. BLAIR. Parametric transducers for resonant bar gravitational-wave antennae. *JOURNAL OF PHYSICS D-APPLIED PHYSICS*, 26:2276 – 2291, 1993.

[63] Patrick A. Truitt. *Measurement of coupling between the electron gas and nanomechanical modes*. PhD thesis, University of Maryland, College Park, 2007.

[64] Patrick A. Truitt, Jared B. Hertzberg, C. C. Huang, Kamil L. Ekinci, and Keith C. Schwab. Efficient and sensitive capacitive readout of nanomechanical resonator arrays. *Nano Lett.*, 7(1):120–126, 2007.

[65] D. Wahyu Utami and A. A. Clerk. Entanglement dynamics in a dispersively coupled qubit-oscillator system. *Phys. Rev. A*, 78:042323, 2008.

[66] S. S. Verbridge, J. M. Parpia, R. B. Reichenbach, L. M. Bellan, and H. G. Craighead. High quality factor resonance at room temperature with nanostrings under high tensile stress. *J. Appl. Phys*, 99:124304, 2006.

[67] Dana Weinstein and Sunil A. Bhave. Internal dielectric transduction: optimal position and frequency scaling. *IEEE Transactions on Ultrasonics, Ferroelectrics, and Frequency Control*, 54:2696–2698, 2007.

[68] Dana Weinstein and Sunil A. Bhave. Acoustic resonance in an independent-gate finfet. In *Proceedings of the Solid State Sensor, Actuator and Microsystems Workshop*, pages 459–462, 2010.

[69] I. Wilson-Rae, N. Nooshi, W. Zwerger, and T. J. Kippenberg. Theory of ground state cooling of a mechanical oscillator using dynamical backaction. *Phys. Rev. Lett*, 99(9):093901, 2007.

[70] Fei Xue, Y. D. Wang, Yu xi Liu, and Franco Nori. Cooling a micromechanical beam by coupling it to a transmission line. *Phys. Rev. B*, 76(20):205302, 2007.